Search for Lepton Universality Violation Using $\Upsilon(3S)$ Decays

by

Gregory King

B.Sc., University of Victoria, 2004
M.Sc., University of Victoria, 2007

A Dissertation Submitted in Partial Fulfillment of the

Requirements for the Degree of
DOCTOR OF PHILOSOPHY
in the Department of Physics and Astronomy

Search for Lepton Universality Violation Using $\Upsilon(3S)$ Decays

by

Gregory King

B.Sc., University of Victoria, 2004
M.Sc., University of Victoria, 2007

Supervisory Committee

Dr. J. M. Roney, Supervisor (Department of Physics and Astronomy)

Dr. R. V. Kowalewski, Committee Member (Department of Physics and Astronomy)

Dr. N. Frank, Committee Member (Department of Chemistry)

ABSTRACT

The measurement of the ratio of the branching fractions of $\Upsilon(3S)$ decays into τ leptons over dimuons ($\mathcal{R}_{\tau/\mu} = \mathcal{B}(\Upsilon(3S) \to \tau^+\tau^-)/\mathcal{B}(\Upsilon(3S) \to \mu^+\mu^-)$) is a test of lepton universality. A violation of lepton universality would be evidence of new physics (and possibly of a light CP-odd Higgs boson). A sample of $\Upsilon(3S)$ decays (2.408 fb^{-1}) collected with the *BABAR* detector at the SLAC National Accelerator Laboratory was used to determine that the ratio $\mathcal{R}_{\tau/\mu}$ is $\mathcal{R}_{\tau/\mu} = 1.0385 \pm 0.034 \pm 0.019$. Using the remaining blinded data sample (corresponding to an integrated luminosity of 25.6 fb^{-1}) the estimated statistical sensitivity will be 1.1 % and the estimated systematic uncertainty of $\mathcal{R}_{\tau/\mu}$ is 1.9 %. Prior to this work, previous measurements of $\mathcal{R}_{\tau/\mu}$ had an estimated total precision of 10 %.

Supervisory Committee

Dr. J. M. Roney, Supervisor (Department of Physics and Astronomy)

Dr. R. V. Kowalewski, Committee Member (Department of Physics and Astronomy)

Dr. N. Frank, Committee Member (Department of Chemistry)

Acknowledgements

I wish to thank my supervisor Dr. Roney, my family and friends, and all members of the *BABAR* Collaboration.

Dedications

This dissertation is dedicated to Melina Young, Owen King, and Kayley King.

Table of Contents

3   The *BABAR* Detector   **29**

4   Methodology   **49**

List of Tables

List of Figures

Chapter 1

Introduction

The Standard Model (SM) is a theoretical framework that attempts to predict and describe all experimental measurements in particle physics. The most recently discovered Standard Model particle is the Higgs boson. In various extensions to the Standard Model there can be more than one *Higgs-like* particle and in certain situations these non-Standard Model Higgs bosons will possess a small mass. If the mass of a non-standard model Higgs boson were close to the $b\bar{b}$ production threshold, detection would be easier at a high luminosity B-factory than at the Large Hadron Collider (LHC).

A direct search for a CP[1]-odd Higgs boson (commonly referred to as a pseudo-scalar) with a mass less than $\Upsilon(3S)$ (the n=3 radially excited $b\bar{b}$ bound state) produced negative results [2].[2] These searches tried to find a monochromatic photon not associated with any known radiative $\Upsilon(3S)$ cascade decays. However, if the intermediate state produced a broad spectrum of photon energies,[3] it could be expected that a signal peak might be masked by

---

[1]Charge Conjugation (C) and Parity (P) are discrete symmetries: The associated symmetry, CP, takes particles and exchanges them with their associated anti-particles. The particle eigenvalues are often used to distinguish between different states. For example, a CP-odd Higgs would have an eigenvalue of -1 when considering a transformation under CP. If CP were a complete symmetry, one would expect the laws of physics to be identical for particles and antiparticles. CP is a valid symmetry when considering the electromagnetic and strong interaction.

[2]This analysis relies upon the following: (a) the CP-odd Higgs boson has a small width; (b) the radiated photon has a high enough energy to permit reasonable detection efficiency; and (c) that these photons will produce an observable peak.

[3]This could possibly happen through interference with η_b or by having a mass such that the emitted photons would have energies below $50\,\mathrm{MeV}$.

background events. A CP-odd Higgs boson will decay more often into tau pairs than into muon pairs, because the tau is more massive than the muon. The presence of a CP-odd Higgs would introduce a violation of lepton universality. Thus, *new physics* might manifest itself as a breaking of lepton universality in the SM, which features couplings between leptons and gauge bosons that are independent of flavour (i.e, electron, muon, or tau).

The CLEO [3] experiment has published results detailing $\Upsilon(1S)$, $\Upsilon(2S)$, $\Upsilon(3S)$ tauonic and muonic branching fractions [4]. CLEO found that within experimental uncertainty ($\mathcal{O} \approx 10\,\%$) lepton universality was respected. The much larger data sample of $\Upsilon(2S)$ and $\Upsilon(3S)$ events collected by the *BABAR* collaboration allows for a more detailed search for a low-mass CP-odd Higgs and provides an excellent opportunity to study the hypothesis of lepton universality at approximately the 2\,\% uncertainty level.

The $\Upsilon(2S)$, $\Upsilon(3S)$ and $\Upsilon(4S)$ events for this analysis were produced at Stanford Linear Accelerator (SLAC). The *BABAR* detector was located at the interaction point (IP) of two asymmetric beams one of electrons (9.0 GeV) and one of positrons (3.1 GeV) in the Positron Electron Project (PEP-II) storage ring facility. A beam of electrons generated by the high energy ring was fired toward an interaction point where it met a beam of positrons generated by the low energy ring but travelling in the opposite direction. The primary physics goal of the *BABAR* experiment involved the study of *CP*-violating asymmetries in the decay of neutral B mesons to CP eigenstates [5–8]. The *BABAR* experiment provided both a large number of B mesons and a large sample of τ and μ pairs ideal for this analysis. In fact, the *BABAR* experiment recorded by far the largest sample of $\Upsilon(3S)$ meson decays currently available for further research.

This dissertation will highlight the background of and the motivation for this research. The methodology section will detail how the experiment was done and define the goals of the study. The event selection for both τ and dimuon events will be detailed and the $\mathcal{R}_{\tau/\mu}$ for the unblinded sample will be estimated, with an evaluation of all the statistical and systematic

errors.

Chapter 2

Theory

This chapter begins with a summary of the Standard Model (SM) and a list of the particles which are constituents of the SM. The properties of leptons and quarks are discussed and an overview of the τ lepton is presented. Finally, a discussion of important observables in the SM is presented.

2.1   Standard Model

The fundamental concepts of classical physics involve both particles and fields. Modern physics unites these concepts in an attempt to fully describe the universe. *Quantizing* any classical field leads to a synthesis of the concepts of particles and fields. Fundamentally, the *quanta* of the fields are particles with specific properties (e.g., spin, charge, mass) while the interactions between charged particles are mediated by an exchange of gauge bosons. The description of the interaction dynamics between elementary particles and three of the four fundamental forces observed in nature is known as the Standard Model (see, for example [9,10]). The four fundamental forces in nature are the following: *strong* (or colour dynamics); *electromagnetic* (or charge dynamics); *weak* (or flavour dynamics); and *gravity* (or geometric dynamics, as defined in terms of General Relativity). Further, the electromagnetic and weak interactions can be unified into a 'single' interaction known as the *electroweak* force. Of the four forces in nature, the Standard Model provides a description of the strong, the weak,

and the electromagnetic forces (the force of gravity is to be too weak to play a significant role in elementary particle physics and can be largely ignored in this discussion [9,11]). Each interaction is distinguished by its inherent strength and its associated charge, as well as by its own particular set of conservation laws and selection rules.

The goal of particle physics is to identify the basic units of matter and the basic forces between them. It is expected that the smallest units of matter will interact in the simplest ways and there will be a connection between the basic units of matter and the basic forces [11].

An elementary particle is an intrinsic building block of matter with no inherent structure. Such particles are usually categorized into three distinct groups called *leptons*, *quarks*, and *mediators*. According to the Standard Model, all 'matter' is built from a number of fundamental spin-$\frac{1}{2}$ particles (fermions) known as quarks and leptons. There are six leptons, and six 'flavours' of quarks. Mediators, such as *photons*, *gluons* and *weak bosons* (including the Higgs), are responsible for the interactions between particles.

Tables 2.1 and 2.2 list the fundamental leptons and quarks. Unlike leptons, quarks are confined to composite systems known as *hadrons* and carry an additional charge known as colour. However, unlike electric charge, colour charge exists in three kinds and the strong interaction is associated with the colour charge.

lepton	charge (e)	mass (MeV/c^2)
ν_e	0	$< 2 \times 10^{-6}$ [12]
e	-1	$0.510998928 \pm 0.000000011$ [12]
ν_μ	0	$< 2 \times 10^{-6}$ [12]
μ	-1	$105.6583715 \pm 0.0000035$ [12]
ν_τ	0	$< 2 \times 10^{-6}$ [12]
τ	-1	1776.82 ± 0.16 [12]

Table 2.1: Lepton electromagnetic classification. The particles are grouped according to generation, in order of increasing mass with respect to the charged lepton of the associated generation.

The known fundamental forces are mediated by a set of spin-1 vector particles (bosons),

quark	charge (e)	mass (GeV/c^2)
d(down)	$-1/3$	$0.0048^{+0.0005}_{-0.0003}$ [12]
u(up)	$+2/3$	$0.0023^{+0.0007}_{-0.0005}$ [12]
s(strange)	$-1/3$	0.095 ± 0.005 [12]
c(charm)	$+2/3$	1.275 ± 0.025 [12]
b(bottom)	$-1/3$	4.18 ± 0.03 [12]
t(top)	$+2/3$	$173.07 \pm 0.52 \pm 0.72$ [12]

Table 2.2: Quark electromagnetic classification. The particles are grouped according to generation.

while the photon is the associated mediator of the electromagnetic interaction. The weak force has three associated vector bosons, the W^+, the W^-, and the Z^0, while the strong interaction is mediated by gluons (in the Standard Model there are eight of them).

Mediator	Charge (e)	Mass (GeV/c^2)	Interaction
gluons (g)	0	0 [12]	strong
photon (γ)	0	0 [12]	electromagnetic
$W^\pm$	± 1	80.385 ± 0.015 [12]	weak
Z^0	0	91.1876 ± 0.0021 [12]	weak

Table 2.3: Mediators of the three forces. The mass of the photon is a theoretical value; the current estimated upper mass limit is 1×10^{-15} MeV/c^2. Similarly, the mass given in the table for the gluon is the theoretical value; a mass as large as a few MeV/c^2 has not been excluded.

The Standard Model uses quantum field theory to explain fundamental particles and interactions. Although each force relies upon underlying quantum field theory, most physical processes (cross sections and decay rates) can only be calculated through the use of Feynman diagrams[1]. Feynman diagrams are also a mechanism to visualize the exchange diagram (or decay diagram) between the initial and final states.

---

[1]These diagrams represent an element of the 'Dyson expansion' or pertubative expansion and only make sense in the weak 'coupling' regime.

2.2   Symmetries

In physics there is an intimate connection between symmetries and conservation laws. For each continuous symmetry of a given physical system there exists a conserved physical property. The convserse also holds. If there is a conserved quantity there will be a symmetry in the underlying physical system. Although the connection between symmetries and conservation laws is vital to a theoretical understanding of the system, it can often mask the underlying nature of the system itself (i.e. a symmetry may actually be associated with something far more fundamental). For example, the idea of SU(2) isospin symmetry associated with protons and neutrons has more in common with the *breaking* of an 'effective' chiral symmetry in QCD (and the small mass of the up, down, and strange quarks), rather than with the near-degeneracy of neutron and proton mass [13,14]. Symmetries are frequently not *ad-hoc* additions to theory, in fact they are often evidence of a more *fundamental* principle.

2.3   Electroweak Theory

Hadrons and leptons experience the weak interaction and may undergo weak decays. Such decays are often 'masked' by strong and electromagnetic decays. It is only in the situation where both the strong and the electromagnetic interactions are suppressed that weak modes can be observed.

Originally, the *weak* current interaction was regarded simply as a way to explain the phenomenon of radioactive decays and as such it did not constitute a proper theory. The original explanation of weak interactions developed by Fermi is broken at high energy scales. These defects are not present in the Standard Model. According to Quantum Field Theory the introduction of spontaneously-broken *gauge* symmetries is the mechanism by which the Higgs field provides fixed masses for the $W^{\pm}$ and Z^0 gauge bosons. The fundamental weak interaction Feynman diagrams are shown in Figure 2.1. The $W^{\pm}$ boson can also interact with a charged lepton and its associated neutrino, as well as with an up-type quark and a

down-type quark. The neutral current and the associated Z^0 exchange involves couplings with almost all standard model particles, except the eight gluons.

Initially the electromagnetic and weak interactions look very different, but it is possible to unify the description with electroweak theory (see [10, 13]).
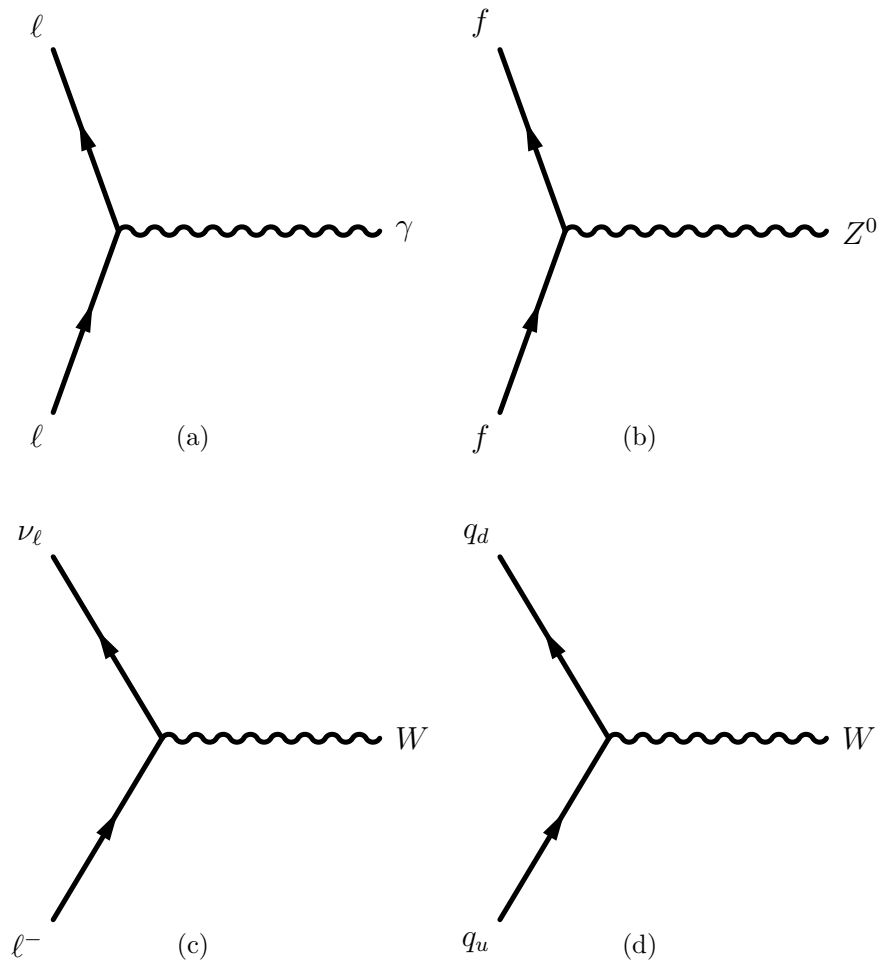
Figure 2.1: <u>Tree level Feynman diagrams,</u> illustrate the *first-order* interactions involving matter and electroweak bosons, where $\ell \in \{e, \mu, \tau\}$, f is a fermion, and $q_{u/d}$ is an up/down-type quark. There are additional self-interaction couplings between the gauge bosons (not shown).

2.4   The τ lepton

The τ lepton was discovered around than 40 years ago by M. Perl *et al.* [15]. It provides a useful tool for testing a wide range of Standard Model phenomena from resonance physics to perturbative short distance physics. Moreover, because the τ is the only known lepton massive enough ($m_\tau \approx 1.777$ GeV$/c^2$) to decay into hadrons, its semi-leptonic[2] decays are ideal for studying strong interaction effects. The τ lepton production mechanism at *BABAR* is shown in Figure 2.2.
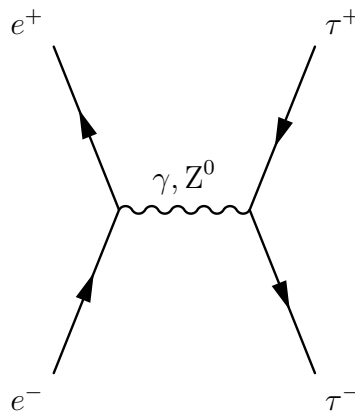
Figure 2.2: <u>Electroweak τ pair production;</u>

The τ decay modes are categorized as either leptonic (see figure 2.3) or semi-leptonic (these decays include at least one hadron) decays (see Figure 2.4). Decays of the τ lepton to hadrons exhibit a complex structure of resonances.

For all hadronic channels, the τ decays through a two-body reaction into a neutrino (ν_τ) and a hadronic resonance, which subsequently decays into other mesons (see Figure 2.4). This is commonly described as $\tau^- \to (\text{had})^- \nu_\tau$, where (had) is used to denote the hadronic component of the decay and the 4-momentum of the hadronic state is the sum of the final-state particles. In the centre-of-mass frame of the τ lepton, the energy of the hadronic system is completely determined by energy and momentum conservation. The matrix element for any semi-leptonic τ decay is complicated by hadronization.

---

[2]Semi-leptonic refers to the fact that the neutrinos are also part of these decays (in addition to the *non-leptonic* hadrons)
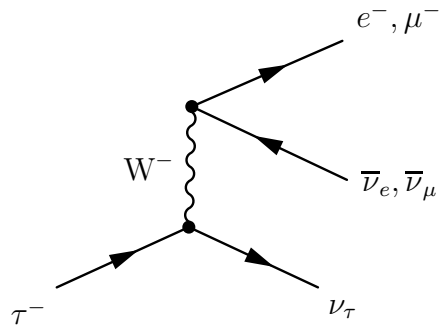
Figure 2.3: τ Leptonic Decay; τ^- which decays into its associated neutrino (ν_τ) and either e^- and $\overline{\nu}_e$, or, μ^- and $\overline{\nu}_\mu$.
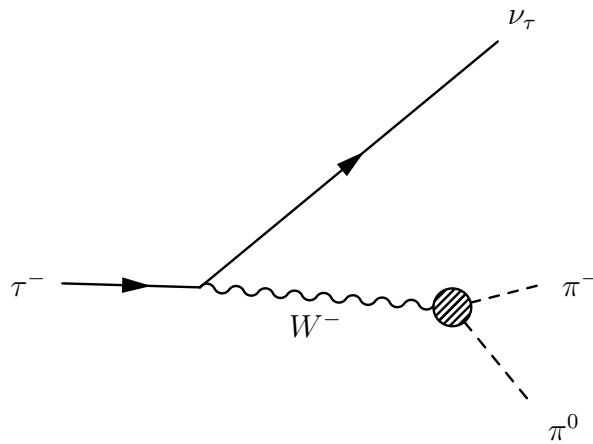
Figure 2.4: τ Hadronic Decay; Feynman diagram of a τ lepton decay with all hadronization and resonance effects represented by the shaded circle.

2.5   Decay Rate and Branching Ratio

The decay rate Γ represents the probability, per unit time, of a particle decaying. The mean lifetime is simply the reciprocal of the decay rate $(1/\Gamma)$. However, because most particles can decay through several channels, it is also necessary to define the total decay rate as the sum of the individual decay rates:

$$\Gamma_{\text{tot}} = \sum_{i=1}^{n} \Gamma_i \tag{2.1}$$

Therefore the lifetime of a decaying particle is the reciprocal of Γ_{tot}.

The *branching ratio* is defined as the fraction of all particles of a given type that decay through a specific decay mode. Branching ratios are determined by decay rates:

$$\mathcal{B}(i^{\text{th}} \ decay \ mode) = \frac{\Gamma_i}{\Gamma_{\text{tot}}} \tag{2.2}$$

2.6   Fermi's Golden Rule

Fermi's Golden Rule provides a prescription for combining dynamic and kinematic information to obtain observable quantities such as decay rates and scattering cross sections. The transition rate for an arbitrary process is determined by the matrix element and the phase space according to:

$$\text{transition rate} = 2\pi|\mathcal{M}|^2 \mathrm{d}R \tag{2.3}$$

where the matrix element $(\mathcal{M})$ contains the dynamic information. On the other hand, $(\mathrm{d}R)$, the phase space factor, contains only kinematic information and depends on the masses, energies, and momenta of the initial and final state particles. The larger the available phase space the more likely a transition is to occur.

Suppose a particle, p_1, decays into several other particles, $(p_2, p_3, ..., p_n)$, then the transition rate is described by the Golden Rule for Decays:

$$\mathrm{d}\Gamma = \frac{S|\mathcal{M}_{p_1 \rightarrow p_2 + ... + p_n}|^2}{2m_1} \times \mathrm{d}R_n \tag{2.4}$$

where S is a statistical factor correcting for identical particles in the final state, and $\mathrm{d}R_n$ is the associated n particle phase space factor.

Suppose particles 1 and 2 collide and produce a set of final state particles (3,4,...,n).[3] The *cross section*[4] is given by:

$$\mathrm{d}\sigma = \frac{S|\mathcal{M}_{p_1+p_2 \to p_3+...+p_n}|^2}{4\sqrt{((p_1 \cdot p_2)^2 - (m_1 m_2)^2)}} \times \mathrm{d}R_n \qquad (2.5)$$

where p_i is the four-momentum of the ith particle (mass m_i), S is a statistical factor (correcting for identical particles in the final state).

At the low energy limit $(2m_\mu \ll \sqrt{s} \ll \mathrm{M_Z})$, the electron-positron annihilation into dimuon cross section reduces to

$$\sigma = \frac{4\pi\alpha^2}{3s} \qquad (2.6)$$

where s is the Mandelstam variable, which can be defined as $s = \mathrm{E}_{cm}^2$ (the centre-of-mass energy squared) and the mass effects of final state fermions have been neglected (and additional threshold effects have also been ignored). The correction to this cross-section, when considering the final state mass term, is on the order of (m_f^4/s^2) [9]. In addition, the effects of the weak neutral current (the Z^0 boson mediated exchange) can be disregarded.

The cross section for τ production near the mass-threshold, to the lowest order, is given by:[5]

$$\sigma_{\tau\tau} = \frac{4\pi\alpha^2}{3s}\beta\frac{3-\beta^2}{2}, \qquad (2.7)$$

where $\beta = |\mathbf{p}_\tau|/\mathrm{E}_\tau$ is the velocity of a τ lepton and α is the *fine structure* constant. There are a number of corrections that have not been included:

- **Final-State Radiation (FSR)**- Since the τ lepton is a charged particle, it can radiate a photon;

---

[3] This can be written $1 + 2 \to 3 + 4 + ... + n$.

[4] The cross section is roughly a measure of how likely a scattering interaction is to occur.

[5] The Z^0 mediated interaction at this scale is tiny compared with the photon mediated interaction [16,17]

- **Coulumb Correction**- At the τ-pair production threshold (when $\sqrt{s} = 2m_\tau$), a pair of τ leptons are produced at rest. The two τ leptons can bind into a τ atom before they decay. As a result of binding energy the cross section at $\mathrm{E_{cm}} = 2m_\tau$ becomes a finite and non-zero value and the Coulomb interaction *binds* the τ leptons;

- **Vacuum Polarization**- The quantum electrodynamics (QED) corrections to the photon propagator due to the insertion of quark and lepton loops;

- **Initial-State Radiation (ISR)**- The cross section is also modified by photon radiation from the initial electrons and positrons. This radiation effectively reduces the centre-of-mass energy of the e^+e^- collisions and the initial cross section has to be replaced by the cross section at some reduced energy. The result is integrated over the cross section taking into account the probability of radiation emissions from the full beam energy down to the threshold;

- **Beam Energy Spread**- An experimental correction is necessary because not all electrons (and positrons) in a collider beam carry exactly the same central beam energy. Therefore the centre-of-mass energy is *smeared* out over a small range which can lead to the production of τ pairs even if the central beam energy is below threshold.

In *BABAR*, the centre-of-mass energy is roughly 10.36 GeV when producing the $\Upsilon(3S)$ meson and 10.58 GeV when producing the $\Upsilon(4S)$ meson. Each of the individual leptons (when pair-produced) will have one-half the total energy, or 5.18 GeV, for the on resonance production of $\Upsilon(3S)$ (5.29 GeV for the $\Upsilon(4S)$) and will thus have momenta of 4.866 GeV/c (4.98 GeV/c for the $\Upsilon(4S)$) and $\beta = 0.939$ (0.941 for the $\Upsilon(4S)$). Using equation (2.7) the values for the τ pair-production cross section at different centre-of-mass energies are enumerated in Table 2.4.

The weak neutral current (Z^0 exchange) should introduce a negligible change in the effective cross section at $\sqrt{s} \approx 10$ GeV when considering any of the interactions $e^+e^- \rightarrow \ell^+\ell^-$

	$\sqrt{s}$	p_τ	β	Cross Section
	(GeV)	(GeV/c)		(nb)
$\Upsilon(2S)$	10.0233	4.686033	0.935028	0.85965
$\Upsilon(3S)$	10.3552	4.863107	0.939259	0.80606
$\Upsilon(4S)$ (off peak)	10.5547	4.969174	0.941604	0.77619
$\Upsilon(4S)$	10.5782	4.981651	0.941871	0.77278

Table 2.4: The first order τ production cross section. Estimating the cross section of τ lepton production at various energies using Equation (2.7). The cross section is stated in nb (in high energy physics, it is common to use units where $\hbar = c = 1$, and thus 1 GeV^{-2} is equivalent to 0.3894 mb = 0.3894×10^6 nb). The estimated cross section using the threshold formula (or the fermionic production cross section from equation (2.6)) is significantly different from the Monte Carlo calculated cross section [18] which includes corrections related to ISR, FSR, and other additional factors.

[9, 10]. Even at low energies ($\sqrt{s} \ll m_{Z^0}$) there are two weak force effects [13]:

1. A modification of the total cross-section from that of QED. At low energies this is proportional to g_V^2 ($g_V^2 = 0.00294$);[6] however, at *BABAR* operational energies this effect should be masked by the dominant QED processes.

2. At low energies the forward-backward asymmetry in the angular distribution measures g_A^2.

2.6.1 τ Leptonic Branching Ratio

The partial width of the decays $\tau^- \to e^- \overline{\nu}_e \nu_\tau$ and $\tau^- \to \mu^- \overline{\nu}_\mu \nu_\tau$ can be calculated using Feynman rules applied to the tree level Feynman diagram in Figure 2.3.

The process can be treated as an effective four-fermion interaction with the effects of the $W^\pm$ propagator added as a correction factor later. The resulting diagram is shown in Figure 2.5.

---

[6]In the case of charged leptons, $g_V \approx -0.5 + 2 \times (1 - m_W^2/m_{Z^0}^2) = -0.0542$
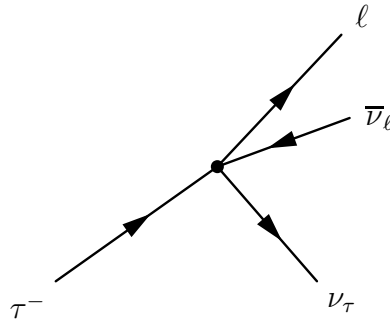
Figure 2.5: <u>Effective Four Fermion Decay of a τ Lepton.</u> The τ^- which decays into its associated neutrino (ν_τ) and a lepton (ℓ) and its associated anti-neutrino ($\overline{\nu}_\ell$ using a Fermi Effective Feynman Diagram). Specifying the direction of fermion 'flow' is not required in this type of diagram, but is included to show its similarity to Figure 2.3.

Using either of the diagrams (Figure 2.3 or Figure 2.5) will yield the following [14,17]:[7]

$$\Gamma(\tau^- \to e^- \overline{\nu}_e \nu_\tau) = \frac{G_F^2 m_\tau^5}{192\pi^2}(1 + \Delta_\ell); \tag{2.10}$$

where G_F is the Fermi coupling constant and the term Δ_ℓ is a correction containing higher order terms, including:

- **Phase Space Corrections** - $O\left(\frac{m_\ell^2}{m_\tau^2}\right)$;

- **QED Radiative Corrections** - $O(\alpha)$;

- **Corrections due to the $W^\pm$ propagator** - $O\left(\frac{m_\tau^2}{m_W^2}\right)$;

---

[7]A more detailed result (from [14]),

$$\frac{d\Gamma}{d\epsilon}(\tau^- \to \ell\overline{\nu}_\ell) = \frac{G_F^2 m_\tau^5}{4\pi^3}\left(\epsilon - \frac{4\epsilon^2}{3} + \epsilon\lambda^2 - \frac{2\lambda^2}{3}\right)\sqrt{\epsilon^2 - \lambda^2}, \tag{2.8}$$

$$\frac{d\Gamma}{d\epsilon}(\tau^- \to \ell\overline{\nu}_\ell) \approx \frac{G_F^2 m_\tau^5}{4\pi^3}\epsilon^2\left(1 - \frac{4\epsilon}{3}\right); \tag{2.9}$$

where $\epsilon = p_0/m_\tau$ and $\lambda = m_\ell/m_\tau$. The kinematic range for the lepton energy is $0 < p_0 < m_\tau^2 + m_\ell^2/(2m_\tau)$. The bounds on this parameter are established by the condition that the four momentum $k - l$ (k is the τ momentum and l is the ν_τ momentum) is *time-like* as seen in the τ rest frame. Because the mass of the daughter lepton is small compared with the mass of the τ lepton, integration can be carried out directly which yields $G_F^2 m_\tau^5/(192\pi^2)$.

The branching ratio for the two leptonic decays is given by:

$$\mathcal{B}(\ell^-\overline{\nu}_\ell\nu_\tau) = \Gamma(\tau^- \to \ell^-\overline{\nu}_\ell\nu_\tau)/\Gamma_{\text{total}}. \tag{2.11}$$

2.6.2   Lepton Universality

Within the framework of the Standard Model leptons have[8] the same coupling constant with respect to all interaction currents[9], except for the recently discovered Higgs boson [19, 20]. For example, if the Fermi constant (G_F) is replaced by a lepton-dependent coupling constant (g_ℓ),

$$\frac{G_F}{\sqrt{2}} = \frac{1}{8}\left(\frac{g_\ell}{m_W}\right)^2 \tag{2.12}$$

for each of the vertices in Figure 2.3 it is possible to compare these independent weak lepton couplings using the measured branching factions $\Gamma(\tau^- \to \mu^-\overline{\nu}_\mu\nu_\tau)$ and $\Gamma(\tau^- \to e^-\overline{\nu}_e\nu_\tau)$ [21–23]. The measured leptonic branching fractions provide constraints on physics beyond the standard model and speaks to the issue of whether lepton universality[10] is valid at the scale of the τ mass.

2.7   Resonances

A *resonance* is defined as a short-lived state with a mass, a lifetime, and a spin (other quantum numbers may be used to characterize this state including angular momentum, parity, etc.). Frequently, a resonance is associated with a very short-lived particle or bound state that cannot be directly observed. A resonance also has an associated lifetime and its characteristic mass will have an associated width. Because the lifetimes of many subatomic particles are too short to be observed directly, the existence of these particles is usually in-

---

[8]Often the guiding principle in formulating theoretical models is Ockham's Razor - '*It is vain to do with more what can be done with fewer*'.

[9]This is one of the many instances of the principle of *Lepton Universality* - which roughly means that all leptons have the same charge

[10]This would be called a violation of *weak* lepton universality, in addition to a violation of lepton universality.

ferred from a peak found in a mass distribution histogram of its decay products. Resonances which involve hadrons are commonly observed in τ lepton decays. For example, in the decay $\tau^- \rightarrow \pi^- \pi^+ \pi^- \eta \nu_\tau$, because the η meson's lifetime is too short for direct observation, it can only be inferred by an examination of the η's decay products.

The decay rate is measured using the energy dependence of a cross section given by the Breit-Wigner cross section formula (see [24]):

$$\sigma(\sqrt{s}) \approx B_{in} B_{out} f_{BW}(\sqrt{s}; m_0, \Gamma); \tag{2.13}$$

$$f_{BW}(\sqrt{s}; m_0, \Gamma) = \frac{4\pi}{k^2} \left[\frac{\Gamma^2/4}{(\sqrt{s} - m_0)^2 + \Gamma^2/4} \right],^{11} \tag{2.14}$$

where Γ is the width, k^2 can be replaced by $\sqrt{s}/2$, $\sigma(\sqrt{s})$ is the cross section of the process at energy $\sqrt{s}$, m_0 is the mean mass of the particle and $B_{in}(B_{out})$ is the branching fraction for the resonance into the initial (final-state) channel.

2.8   Reference Frames for Collision Processes

In a two-particle collision, particles a and b with four-momenta $p_a = (E_a, \mathbf{p}_a)$ and $p_b = (E_b, \mathbf{p}_b)$ collide. The values of $\mathbf{p}_a$ and $\mathbf{p}_b$ are fixed by experimental conditions within defined experimental uncertainties. Different frames can be defined by requiring $\mathbf{p}_a$ or $\mathbf{p}_b$ to have some special values. The following are the most frequently used frames of reference:

- **Laboratory System** (LS) is defined as the system in which the experiment is carried out and all energies and momenta will be measured. It is fixed by the experimental set-up, which may involve either a beam of particles hitting a stationary target, or by two colliding beams. Unless otherwise stated, all measured quantities will by associated with the LS.

---

[11]The relativistic Breit-Wigner formula is:

$$\frac{12\pi}{m_0^2} \Gamma_{in} \Gamma_{out} \frac{s}{(s - m_0^2)^2 + \frac{s^2}{m_0^2} \Gamma^2}$$

- **Centre-of-Momentum System** (CMS) is defined as the system in which $\mathbf{p_a} + \mathbf{p_b} = \mathbf{0}$. All CMS quantities will be denoted by sub-script, E_{CMS}. The definition can be extended to a decay system or to a centre-of-mass system in a reference frame such that $\mathbf{p}_{decay} = \mathbf{0}$.

2.9   Helicity and Helicity Angle

Two commonly used parameters in physics analysis are helicity and helicity angle. In the arbitrary decay, $Y \rightarrow X \rightarrow a + b$, the helicity angle of particle a is the angle measured in the at-rest frame of the decaying parent particle X between the direction of the decay daughter a and the direction of the grandparent particle Y. The helicity angle distribution is useful in many high energy physics analyses because background events may exhibit different angular distributions from signal events. Helicity angle is also a useful test to select (or reject) events which contain π^0 mesons.

2.10   Phase Space

Phase space is most significant when considering an arbitrary physical system as a whole. The description of a process within a physical system can be divided into two parts: the *dynamic* and the *kinematic*. The greater the number of particles participating in a process, the more important (and possibly dominant) the kinematic term will be when considering the overall behaviour of the system.

When the number of degrees of freedom or the number of particles is reduced, the dynamical aspect of interaction becomes more important. In particle physics interaction dynamics influences the form of physical laws in significant ways. Although the end goal of particle physics is to understand interaction dynamics, kinematics will always play a role such that even in particle physics there is a phase space factor (dR_n) which describes the kinematic aspects of a process.

Studying the phase space factor is increasingly important in systems with few particles because the phase space factor creates a possible background distribution. Furthermore, a variation from phase space may imply that there are underlying dynamics. Although disentangling the actual dynamical effects that cause such a deviation can be difficult, phase space distributions can also play a significant role in the search for hadronic resonances.

Consider the arbitrary particle reaction:

$$p_a + p_b \rightarrow p_1 + ... + p_n \tag{2.15}$$

Imposing the condition of four-momentum conservation on the final state, the n-momentum vectors cannot vary arbitrarily for a given fixed initial state. Therefore, the following conditions can be applied:

$$\left.\begin{aligned} E_a + E_b &= \sum_{i=1}^{n} E_i \\ \mathbf{p}_a + \mathbf{p}_b &= \sum_{i=1}^{n} \mathbf{p}_i \end{aligned}\right\} \tag{2.16}$$

with,

$$E_i^2 = \mathbf{p}_i^2 + m_i^2, \quad i \in a, b, 1, ..., n \tag{2.17}$$

where the m_is are fixed particle masses, the 3n-dimensional space of unconstrained final state momentum vectors $\mathbf{p}_i$ is called the momentum space and conditions (2.16) and (2.17) define a $3n - 4$ dimensional surface called *phase space*. Because the dynamics of particle processes are rarely described in terms of momentum vectors, invariants and variables motivated by specific types of interactions are usually used to parametrize phase space.

It is important to distinguish between the two different types of experimental processes: exclusive reactions or inclusive reactions. An *exclusive* reaction is one in which all particles and their momenta are known, while in an *inclusive* reaction only some of the particles and momenta are known such that the final state is not completely identified or involves a sum over a subset of all exclusive channels (see Figure 2.6). Two types of sub-processes are

encountered in practice: particle decays and interactions between two particles.
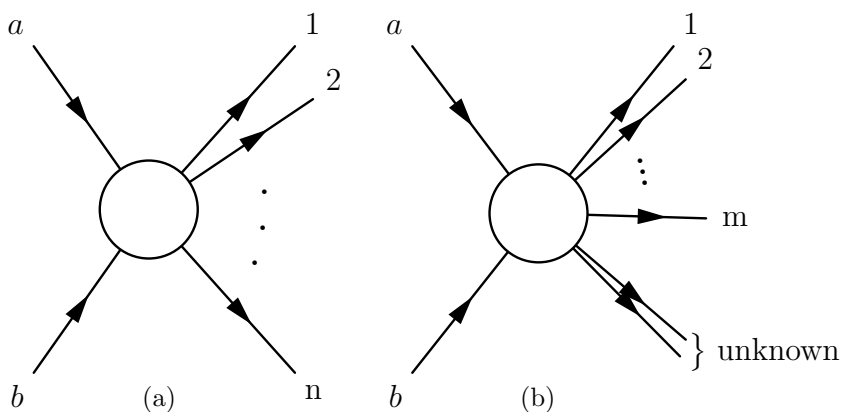
Figure 2.6: Inclusive and Exclusive Scattering Reactions. Examples of an exclusive (a) and inclusive (b) scattering reaction. In (a) all particles (1-n) are *observed*. In (b) all of the particles (1-m) are observed, while some particles (labelled unknown) are not constrained (or observed).

The transition probability (defined as the chance that an initial state will transform into a given final state) is obtained from the matrix element. The purpose of many experiments is to clarify or determine the structure of this matrix element. In order to obtain measurable quantities, the square of the matrix element has to be integrated over all allowed values of momentum. The total reaction cross-section or decay rate is then obtained by integrating over all of phase space and the cross section is addresses a scattering process, while the decay rate is related to a decay process. The invariant phase space term, $(\mathrm{d}R_n)$ [9, 25, 26], up to a multiplicative constant of $(2\pi)^{4-3n}$, is given by:

$$\mathrm{d}R_n(\mathrm{P}; \mathrm{m}_1, \mathrm{m}_2, ..., \mathrm{m}_n) = \prod_{i=1}^{n} \mathrm{d}^4\mathrm{p}_i \delta(\mathrm{p}_i^2 - \mathrm{m}_i^2)\delta^4(\mathrm{P} - \sum_{j=1}^{n}\mathrm{p}_j) \qquad (2.18)$$

2.11 Semi-Leptonic τ Decay Width

For a semi-leptonic decay of the τ, the matrix element[12] (ignoring the propagator of the $W^\pm$ boson) is:

$$\mathcal{M} \propto J_{\text{lep}}^\mu J_\mu^{\text{had}} \tag{2.19}$$

where, J_{type}^μ is the vector-current associated with weak leptonic (J_{lep}^μ) or hadronic (J_{had}^μ) interactions.[13] Since it is not known how the $W^\pm$ and Z^0 will couple with composite structures like hadrons, the term J_μ^{had} (also called the hadronic weak interaction current or hadronic form factor) is only determinable experimentally.[14]

When hadronization produces a single pion ($\tau^- \to \pi^- \nu_\tau$), the hadronic current can be reduced to $J_\mu^{\text{had}} = f_\pi p_\mu$ (see, for example, [10,27]) where p_μ is the four-momentum of the π^- and f_π is known as the pion decay constant. The pion decay constant can be obtained by measuring the π^- lifetime. For example, the partial decay width for the reaction is

$$\Gamma(\tau^- \to \pi^- \nu_\tau) = \frac{G_F^2 f_\pi^2 \cos^2(\theta_C) m_\tau^3}{8\pi} \left(1 - \frac{m_{\pi^-}^2}{m_\tau^2}\right)^2, \tag{2.20}$$

where G_F is the Fermi coupling constant and θ_C is the Cabibbo angle [24].

2.12 Experimental Branching Fraction and Cross Section

The general equation used to determine the experimental branching fraction of a particular decay is:

$$\mathcal{B}(\tau^\pm \to X^\pm \nu_\tau) = \frac{N_{\text{sel}}^{\tau^\pm \to X^\pm \nu_\tau}}{2N_{\tau^+\tau^-}} \tag{2.21}$$

---

[12]The matrix element is commonly written $\mathcal{M}$.

[13]The definition of leptonic current can be found in Griffiths [9] or Halzen and Martin [10].

[14]The $W^\pm$, which is responsible for the decay of the τ lepton, actually couples with *free* quarks. However, at energies below $m_\tau c^2$, quarks are strongly bound into mesons and decays of the τ lepton can be described by a hadronic current coupling to the $W^\pm$. The hadronic current leads to a final state with one or more mesons such that it is called a hadronic current rather than a quark current.

where $N_{\mathrm{sel}}^{\tau^\pm \to X^\pm \nu_\tau}$ is the number of observed events (that match $\tau^- \to X^- \nu_\tau$) and $N_{\tau^+\tau^-}$ is the number of τ pair events. Because this is an experimental measurement the equation must be modified to include experimental efficiency and remove background contamination, and leads to:

$$\mathcal{B}(\tau^\pm \to X^\pm \nu_\tau) = \frac{N_{\mathrm{sel}}}{2N_{\tau^+\tau^-}} \frac{1 - f_{\mathrm{bkg}}}{\varepsilon_{\mathrm{sel}}} \tag{2.22}$$

where $\varepsilon_{\mathrm{sel}}$ is the efficiency for selecting $\tau^\pm \to X^\pm \nu_\tau$, and f_{bkg} is the estimated fraction of background contamination.

Similarly, the experimentally relevant formula for cross section is given by:

$$\sigma_{\ell^+\ell^-} = \frac{N_{\ell^+\ell^-}}{\mathcal{L}} \frac{1 - f_{\mathrm{bkg}}}{\varepsilon_{\mathrm{sel}}} \tag{2.23}$$

where $\mathcal{L}$ is the total luminosity of the sample, f_{bkg} is the estimated background fraction, and $\varepsilon_{\mathrm{sel}}$ is the selection efficiency.

2.13   Simulated Events

Monte Carlo (MC) methods are often required in physics research to 're-parametrize' a problem which is not solvable analytically. Monte Carlo methods commonly rely upon computers and a large number of *pseudo-random* numbers to *sample* a distribution and obtain a numerical result.[15]

In experimental particle physics, Monte Carlo methods are used to do the following: to calculate theoretical cross sections; to generate a set of synthetic events and any subsequent decay processes; to estimate the interactions of charged and neutral particles within detector material; as well as to simulate detector response to certain interactions including estimating detector behaviour due to running conditions, detector age and radiation damage. The Monte Carlo software used in this analysis has been vetted by many different particle physics collaborations (including the *BABAR* collaboration) as having high accuracy and precision.

---

[15]Monte Carlo simulation is commonly referred to as *stochastic* simulation.

Further, an experimentalist will often use Monte Carlo methods to estimate the size of systematic errors, determine the sensitivity and stability of analyses and to facilitate numerically accurate error estimates.

Synthetic events can also provide a mechanism to estimate parameters such as efficiencies and background rates so Monte Carlo methods are commonly used as a mechanism to find parameters which can be used to discriminate between signal and background events and thereby improve experimental sensitivity.

2.14   Estimators

An *estimator* ($\hat{a}$) is a method which, when applied to a data sample, will produce a numerical measurement of a property of the parent population or distribution.[16] A *study* sample can be drawn from a larger parent population (in particle physics referred to as *total events*) or it can be generated from a probability distribution function[17] whereby the value of $\hat{a}$ depends upon the data sample chosen.

The estimator is said to be *efficient* and will likely be a good measure of the true value 'if the variance of the estimator is small so that the difference between the estimate and the true value will tend to vanish for large samples [28]'. Such an estimator is said to be *consistent* if the estimator's value tends to the true value when considering larger data sets. For a finite sample an estimator should be *unbiased*, that is, 'the chances of an overestimate will balance the chances of an underestimate [28]'. If the number of measurements is sufficienctly large, uncertainties associated with systematic effects can be important, or even dominate the overall uncertainty.

---

[16]When an estimator of some property a is applied to a data sample it produces an estimate $\hat{a}$.

[17]*Point* estimation involves determining a single value; *interval* estimation determines a range of values which will most likely include the true parameter value. An estimator of a parameter is a *statistic*; a statistic is a function which can be applied to a random variable (or to a set of random variables).

2.15   Motivation

In the Standard Model framework couplings between leptons and gauge bosons are independent of lepton flavour (if one neglects the final-state lepton mass effects). The decay width, denoted Γ, for $\Upsilon(\mathbf{nS}) \to \ell^+ \ell^-$ is estimated to be (see [29]):

$$\Gamma^{\mathbf{n}}_{\Upsilon \to \ell^+ \ell^-} = 4\alpha^2 Q_b^2 \frac{|R_{\mathbf{n}}(0)|^2}{M_\Upsilon^2} \times K(x) \tag{2.24}$$

where α is the fine structure constant, Q_b is the charge of the bottom quark, $|R_n(0)|$ is the non-relativistic radial wave function of the bound $b\bar{b}$ states (evaluated at the origin), and the phase space factor $K(x)$, for the 2S and 3S is equal to:

$$K(x) = (1 + 2x)(1 - 4x)^{\frac{1}{2}} \tag{2.25}$$

where $x = m_\ell^2 / m_\Upsilon^2$. The ratio of the branching fractions, $\mathcal{R}_{\tau/\mu} = \Gamma_{\Upsilon \to \tau\tau} / \Gamma_{\Upsilon \to \mu\mu}$ is governed entirely by the kinematic factor and yields $\mathcal{R}_{\tau/\mu} = 0.9946$ ($\Upsilon(3S)$).

In several extensions to the Standard Model, for example in the next-to-minimal supersymmetric standard model (NMSSM), the Higgs sector can include up to seven physical Higgs bosons. In many models with an expanded Higgs sector parameter space allows for a CP-odd Higgs boson with a mass around 10 GeV/c^2. If a CP-odd Higgs exists (commonly denoted A^0 and often called a *pseudoscalar* Higgs boson) it would be evidenced by a dependence on lepton type.[18] Higgs-like interactions would influence the observed lepton decay width of the $\Upsilon(3S)$ mesons as illustrated by the Feynman diagram (Figure 2.7). Since a CP-odd Higgs interaction term has a coupling constant that is proportional to the mass of the fermion,

$$\mathcal{L}^{f\bar{f}}_{\text{int}} = -X_f \frac{A^0}{v} m_f \bar{f}(i\gamma_5)f \tag{2.26}$$

the interaction between the A^0 and τ-pairs is considerably larger than the interaction between

---

[18]Since the charged lepton in each generation has a large mass difference when compared to the previous generation, see Table 2.1.

the A^0 and muon pairs. Such an interaction would be an observable breaking of *lepton universality* [30]. B. Aubert, *et al.* limited the direct search of the Higgs to the mass range of 4.03-10.1 GeV/c^2 [31]. Direct detection of a Higgs mediated decay [31,32] could be difficult for the following reasons:

1. The quantum interference between a light CP-odd Higgs and an η_b meson (see Figure 2.8) may imply non-monochromatic radiated photons [33],

2. The observable mass peak of the associated radiated photon would be broadened by detector energy resolution,

3. The photon peak could be hidden by low energy radiation.
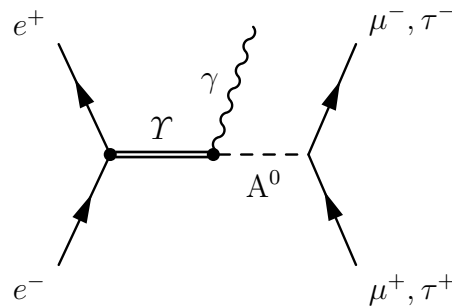
Figure 2.7: Higgs Mediated Feynman Diagram of $e^+e^- \rightarrow \Upsilon(n\mathrm{S}) \rightarrow \tau^+\tau^-$ Feynman diagram of the process $e^+e^- \rightarrow \Upsilon(n\mathrm{S}) \rightarrow \tau^+\tau^-$ with a pseudoscalar Higgs
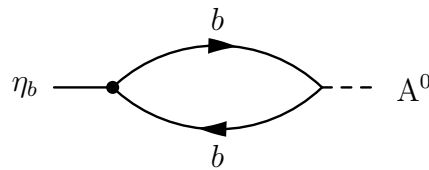
Figure 2.8: Mixing Diagram between an η_b and a CP-odd Higgs.

The decay width of a CP-odd Higgs boson into a τ-pairs is given by

$$\Gamma[A^0 \to \tau^+ \tau^-] \simeq \frac{m_\tau^2 \tan^2 \beta}{8\pi v^2} m_{A^0} (1 - 4x_\tau)^{1/2} \tag{2.27}$$

with $x_\tau = (m_\tau/m_{A^0})^2$ [34]. Radiative decays of $\Upsilon(3S)$ into an on-shell CP-odd Higgs boson would yield a relative width of

$$\frac{\Gamma[\Upsilon(3S) \to \gamma A^0]}{\Gamma[\Upsilon(3S) \to e^+ e^-]} = \frac{m_{\Upsilon(3S)}^2 \tan^2 \beta}{8\pi \alpha v^2} \left(1 - \frac{m_{A^0}^2}{m_{\Upsilon(3S)}^2}\right) \tag{2.28}$$

where v is the vacuum expectation value (246 GeV), α is the fine structure constant, and m is the mass of the particle (denoted by the subscript). The width of CP-odd Higgs boson to τ pairs should be the dominate decay [34]. As both $\tan \beta$ and m_{A^0} are model dependent parameters, any interpretation of the measured $\mathcal{R}_{\tau/\mu}$ will depend upon these parameters. For example, if $\tan \beta = 15$ and $m_{A^0} = 10.2$ GeV would yield an estimated width of $\Gamma[\Upsilon(3S) \to \gamma A^0] = 0.033 \Gamma[\Upsilon(3S) \to e^+ e^-]$ and a $\mathcal{R}_{\tau/\mu}$ of 1.033.

> For the sake of comparison with other Higgs searches, the ξ_f factor with the
> 2HDM (type II) parameter for the universal down-type fermion coupling to a CP-
> odd Higgs, i.e. $\xi_b = \xi_l = \tan \beta$, [is] defined as the ratio of the vacuum expectation
> values of two Higgs fields. Inserting numerical values [yields] the interval
>
> $$\mathcal{R}^\star \approx (3.6 \times 10^{-9} - 4.5 \times 10^{-7}) \times \tan^4 \beta \times m_\ell^2 \tag{2.29}$$
>
> where the approximation $m_{A^0} \approx 2m_b \approx 10$ GeV is used, the range for soft photon
> energy is 10-50 MeV and m_ℓ is expressed in GeV. [35][19]

The quantity $\mathcal{R}^\star = \mathcal{R}_{\tau/\mu} - 1$ is the ratio of the estimated branching fraction of $\Upsilon(3S) \to \gamma \ell^+ \ell^-$ (mediated by a CP-odd Higgs with a mass similar to that of $\Upsilon(3S)$ meson) to the Standard Model branching fraction of $\Upsilon(3S)$ of a particular lepton-pair. The quantity, $(3.6 \times 10^{-9} - 4.5 \times 10^{-7})$ is given as a range because soft photon emission is only constrained

---

[19]The preceeding quotation is reproduced with corrections highlighted in square brackets.

within the range of 10-50 MeV. If one assumed that the branching fraction, $\Upsilon(3S) \to \ell^+\ell^-$, would show the largest deviation for the τ-pair channel and also assumed that $\mathcal{R}^\star$ was on the order of 0.10, it would yield a parameter range of $16 \lesssim \tan\beta \lesssim 54$. The expected deviation for the μ-pair channel would be negligible. It follows that the ratio $\mathcal{B}(\Upsilon(\mathbf{n}\mathrm{S}) \to \tau^+\tau^-)/\mathcal{B}(\Upsilon(\mathbf{n}\mathrm{S}) \to \mu^+\mu^-)$ can be used as a measure lepton universality.[20]

This analysis uses $\Upsilon(3S)$ decays collected by the *BABAR* detector at the PEP-II collider at the SLAC National Accelerator Laboratory as an experimental tool to test if lepton universality is valid at centre-of-mass energies around 10 GeV/c^2. The branching fraction of $\Upsilon(3S)$ decays to leptons is denoted by $\mathcal{B}(\Upsilon(3S) \to \ell^+\ell^-)$, where $\ell = \mu, \tau$ and the ratio of the branching fraction $\mathcal{R}_{\tau/\mu}(\mathbf{n}S) = \mathcal{B}(\Upsilon(\mathbf{n}\mathrm{S}) \to \tau^+\tau^-)/\mathcal{B}(\Upsilon(\mathbf{n}\mathrm{S}) \to \mu^+\mu^-)$

The *BABAR* sample of $\Upsilon(3S)$ decays corresponds roughly to an integrated luminosity of 28.0 fb^{-1} and 2.62 fb^{-1} of off-resonance data[21]. The 28.0 fb^{-1} dataset represents the largest sample of $\Upsilon(3S)$ decays collected to date[22] and the 13.6 fb^{-1} $\Upsilon(2S)$ sample is the second largest sample of such decays generated (with 1.42 fb^{-1} of off-resonance data collected at 30 MeV below the $\Upsilon(2S)$ resonance). The design and operation of the *BABAR* detector are detailed later in this paper (also note [5,6]).

The *BABAR* detector was specifically designed to handle the asymmetric beam energies provided by the PEP-II storage rings in order to facilitate comprehensive studies of CP-violation in B-meson decays. The lower-energy beam of positrons has an energy of 3.111 GeV, while the higher-energy beam of electrons has an energy of 8.61 GeV for $\Upsilon(3S)$ production, or 8.07 GeV in the case of $\Upsilon(2S)$ production. It should be noted that due to the differences in beam energies the centre-of-mass reference frame moves relative to the the lab frame of the

---

[20]This relies upon the assumption that the deviation for μ-pair, in the presence of a Higgs-like interaction, is negligible and thus can be treated as an estimate for the $\Upsilon(3S) \to \tau\tau$ branching fraction without the Higgs interaction.

[21]Collected at 30 MeV below the $\Upsilon(3S)$ resonance.

[22]CLEO collected 1.2 fb^{-1} at the $\Upsilon(3S)$ and 1.2 fb^{-1} at the $\Upsilon(2S)$ [4]. The BELLE collaboration collected 2.9 fb^{-1} at the $\Upsilon(3S)$ and 24.9 fb^{-1} at the $\Upsilon(2S)$ [36]

detector.[23]

The *BABAR* detector also has several independent sub-detector elements. The inner detector consists of the following elements: a silicon vertex tracker (SVT); a drift chamber (DCH); a ring-imaging Cherenkov detector (DIRC); and a CsI electromagnetic calorimeter (EMC). These detector subsystems are surrounded by a 1.5 Tesla superconducting solenoid. The steel instrumented flux return (IFR) is designed for muon and neutral hadron detection. A schematic layout of the *BABAR* detector is shown in [5, 6].[24]

---

[23] $\beta\gamma = 0.53$ for the $\Upsilon(3S)$.

[24] The *BABAR* detector has a slight forward asymmetry biased in the direction of travel of the incoming electron beam.

Chapter 3

The *BABAR* Detector

This chapter provides an overview of the hardware and software used to acquire data using the *BABAR* detector, the linear accelerator and the PEP-II storage rings. It also provides an outline of the *BABAR* detector's architecture, with a primary focus on the components used for detecting final state particles.

3.1 Introduction

Progress in experimental physics depends upon improved methods of measurement: in high energy physics scientists use particle accelerators and detectors as their primary experimental tools.

Accelerators impart high energies to charged particles (both subatomic and atomic), which then collide with *targets* of various kinds such as charged particles and atoms. Often, higher energy collisions will serve best to test the properties of fundamental interactions and particles.[1] The presence and behaviour of the particles emerging from collisions are recorded by detectors placed around the interaction point so as to facilitate a reconstruction of the interaction.

The charged and stable constituents of ordinary matter - electrons and protons - are easy to produce in isolation, while more *exotic* particles come from three main sources, cosmic

---

[1]This *rule* is not always true. The *BABAR* detector provides precision measurements related to b-quarks and τ leptons without the highest available beam energies.

rays, nuclear reactors, and particle accelerators.

A large number of electrons are 'produced' through the photoelectric effect. Once produced, the electrons can be organized into a 'beam' by inducing them to pass through a hole in a positively charged plate.[2]

The production of massive particles requires higher energy collisions. High *centre-of-mass energy* conditions are easier to achieve by colliding two high-speed particles head-on rather than firing one particle at a stationary target. For this reason many high energy physics experiments involve colliding beams.

A high energy e^+e^- collision can give rise to a shower of particles that spreads outward from an interaction point. Results are then *recorded* using an array of specialized sub-detectors designed to measure the properties of these particle showers.

At energies above 10 MeV most photon interactions create electron-positron pairs. Electrons or positrons produced from such interactions can be detected as charged particles. Neutrinos, on the other hand, can only be detected by observing their weak interactions with nuclei or with electrons.[3] Neutron and neutral hadron detection relies upon observing the strong interactions with nuclei and the subsequent emission of charged particles or photons.

Charged particles can be detected directly through their electromagnetic interactions. When a charged particle traverses a layer of detector material, the following four processes can occur:

1. atoms can be ionized,

2. the particle can emit Cherenkov radiation,

3. the particles can cause the emission of transition radiation, or,

---

[2]This device is known as an *electron gun*.

[3]Neutrino detection probability is very low. However, the presence of a neutrino can be inferred from the missing energy in an event.

4. the particles can radiate an energetic photon through Bremsstrahlung.

Most detectors follow a standard design geometry. Moving out radially from the interaction point most high energy physics detectors incorporate the following devices:

1. A Tracking Chamber - this chamber facilitates a measurement of a charged particle's momentum moving outwards from the interaction point. In order to measure the momentum of charged particles the tracking chambers are placed within a magnetic field.

2. Some type of Calorimetry, which provides energy measurements of photons and charged particles.

3. Muon detectors, which attempt to determine whether a charged track was produced by a muon rather than a pion, a kaon or a proton.

3.2   The Stanford Linear Accelerator Center

The Stanford Linear Accelerator Center (SLAC), which was established in 1962 is, at 3.2 km, the largest linear accelerator in the world (see Figure 3.1). A linear accelerator (LINAC) uses electromagnetic waves to accelerate charged particles until they reach velocities approaching the speed of light. Electrons are knocked off the surface of a semiconductor with a laser, while positrons are created by firing an electron beam at a tungsten target (a composite tungsten target is used because of its high atomic number, high melting point, high strength and the likelihood it will produce enough positrons per incident electron).

The electron and positron *bunches*[4] achieve an energy on the order of 10 MeV after travelling three meters along the linear accelerator (the linear accelerator is capable of accelerating electrons and positrons to energies of 50 GeV). Because these 'bunches' have a tendency to

---

[4]A collection of coherently travelling electrons or positrons (small spatial separation and similar momentum).
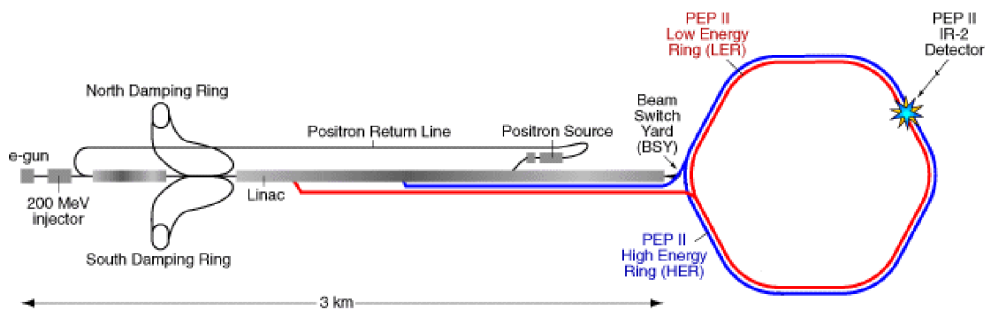
Figure 3.1: SLAC and PEP-II Rings Schematic [37].

disperse in the plane perpendicular to their travel, the electron and the positron bunches are purposely fed into *damping* rings. As the bunches circulate in a damping ring, they lose energy by *synchrotron* radiation, however they are subsequently re-accelerated each time they pass through a cavity in the ring which exposes them to electric and magnetic fields. The synchrotron radiation decreases motion in all directions and damps out motion in the perpendicular plane, while the re-accelerating field keeps the particles moving at relativistic speeds. These now more-compact bunches are then re-injected into the accelerator at a higher velocity.

Electrons and positrons are further accelerated down a long copper tube reaching ultra-relativistic speeds through the action of microwaves supplied by a series of klystrons. After travelling the length of the accelerator, the particles are fed into the PEP-II (Positron-Electron Project-II) storage rings. The first PEP-II ring stores high energy electrons (9 GeV), while the second ring (above the electron ring) stores lower energy positrons (3.1 GeV). The configuration of the rings makes it possible to use asymmetric beam energies for the study of CP violations of the B meson system. The produced beams collide at the interaction point located near the centre of the *BABAR* detector.

The PEP-II rings were designed to provide high instantaneous luminosity for B and τ physics of $\mathcal{O}(10^{34}\text{cm}^{-2}\text{s}^{-1})$ and originally meant to operate with a centre-of-mass energy of 10.58 GeV, which corresponds to the production threshold of the $\Upsilon(4S)$. While most of the data was recorded at the $\Upsilon(4S)$ resonance peak, about 12 % of the measurements were taken

at a centre-of-mass energy around 30 MeV lower. The off-peak dataset allows for studies of the non-resonant background. In addition, smaller data samples were recorded at the $\Upsilon(2S)$ and $\Upsilon(3S)$ resonances. The high energy beam was tuned to a lower energy (around 380 MeV) to reach the $\Upsilon(3S)$ and by 550 MeV to reach the $\Upsilon(2S)$. The masses and widths of the resultant $\Upsilon(2S)$, $\Upsilon(3S)$, $\Upsilon(4S)$ resonances are listed in Table 3.1.

Resonance	Mass (GeV/c^2)	Width (Γ) (MeV/c^2)
$\Upsilon(2S)$	10.0233 ± 0.0003	0.03198 ± 0.00263
$\Upsilon(3S)$	10.3552 ± 0.0005	0.02032 ± 0.00185
$\Upsilon(4S)$	10.5828 ± 0.0007	20.5 ± 2.5

Table 3.1: $\Upsilon(\mathbf{n}S)$ Masses and Widths. The Particle Data Group (PDG) claims the mass of the $\Upsilon(4S)$ is 10.579 ± 0.001 GeV/c^2. This is in contrast to the *BABAR* collaboration measured 10.5828 ± 0.0007 GeV/c^2, which is roughly 3.4 MeV/c^2 different, and is defined as a *calibration* error associated with the PEP-II beam energies. [6])

3.3   The *BABAR* Detector

Because the *BABAR* detector was specifically designed to handle the asymmetric beam energies provided by the PEP-II storage rings, the detector was offset by 0.37 meters in the direction of the lower energy beam relative to the interaction point. The right-handed coordinates are anchored within the main tracking system such that the z-axis coincides with the direction of the e^- beam. The positive y-axis points upwards and the positive x-axis points away from the centre of the storage rings.

The most important requirements for B and τ physics are as follows:

- a large uniform acceptance down to small polar angles relative to the boost direction;

- excellent reconstruction efficiency for charged particles down to 60 MeV/c and for photons to 20 MeV;

- very good momentum resolution;

- excellent energy and angular resolution for the detection of photons with energy 20 MeV to 4 GeV; and

- very good vertex resolution, both transverse and parallel to the beam direction.

- efficient identification of electrons, muons, and hadrons.
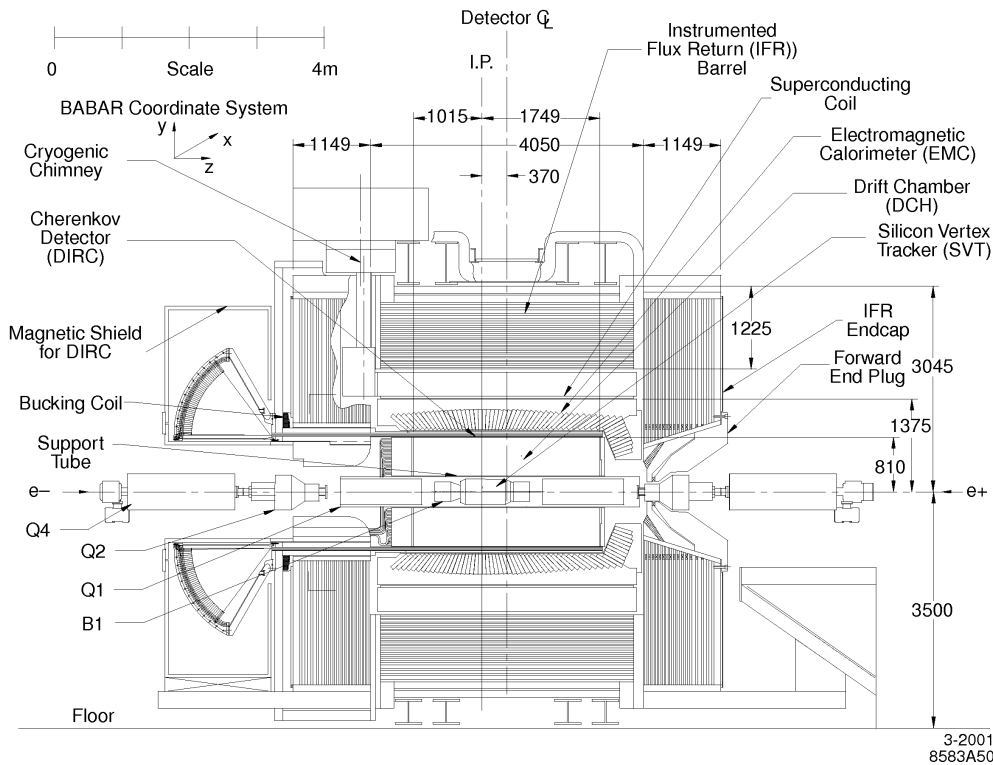
Figure 3.2: *BABAR* detector longitudinal section

The *BABAR* detector met these requirements because of its independent detector elements. The inner detector consists of a silicon vertex tracker (SVT), a drift chamber (DCH), a ring-imaging Cherenkov detector (DIRC), and a CsI electromagnetic calorimeter (EMC). These detector subsystems are surrounded by a 1.5 Tesla (T) superconducting solenoid. The steel instrumented flux return (IFR) was instrumented for muon and neutral hadron detection. The schematics of the *BABAR* detector are shown in Figure 3.2 and Figure 3.3.
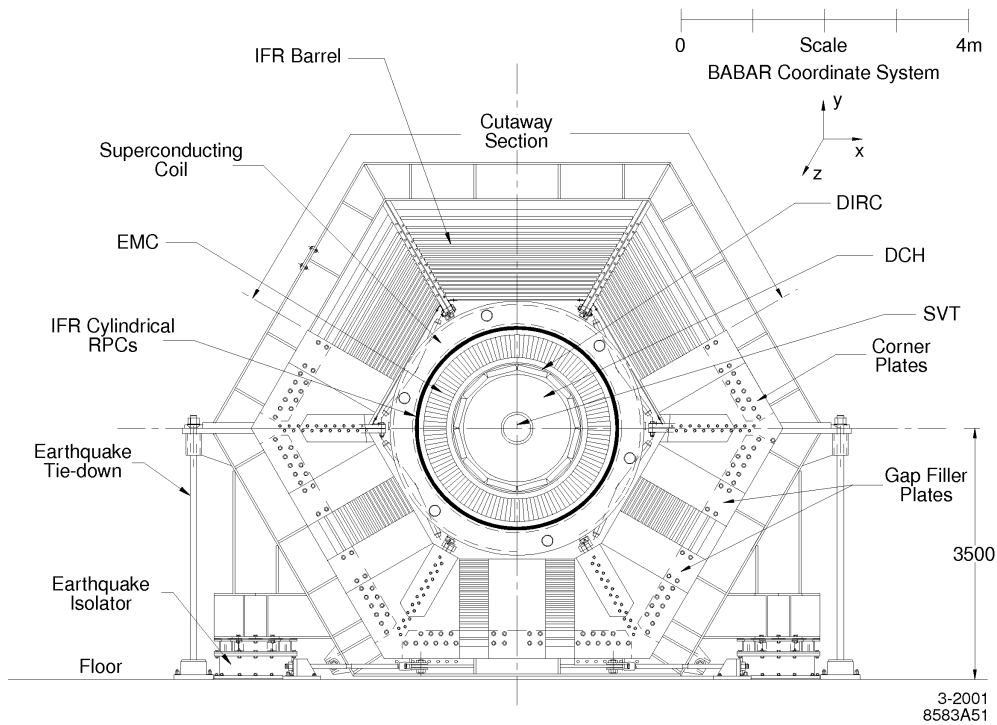
Figure 3.3: *BABAR* detector end view.

3.4   Particle Tracking

The charged particle tracking system has the following two components: a silicon vertex tracker (SVT) and a drift chamber (DCH). The SVT provides position and angle information for the determination of the vertex position just outside the interaction region. The DCH enables the detection of charged particles as well as a determination of their momenta and angles. The magnet supplies a high magnetic field (1.5 T) along the axis of the beam pipe, which bends the path of the charged particles in the detector and allows for momentum determination.

3.5   Silicon Vertex Tracker

The SVT was designed to enable a precise reconstruction of charged particle trajectories and decay vertices near the interaction region. It is composed of five layers of double-sided silicon strip detectors centered on the beam pipe. These layers are organized in 6, 6, 6, 16, and 18 modules respectively (see Figure 3.4 and Figure 3.5). The ϕ measuring strips run parallel to the beam, while the z measuring strips are oriented transversely to the beam axis. The three inner layers are straight, with the innermost layer positioned at a radius of 32 mm from the beam axis, while the modules of layers 4 and 5 are arch-shaped.

The SVT provides stand-alone tracking for particles with low transverse momentum near the interaction point. Finally, double-sided sensors provide up to ten measurements of dE/dx[5] per track. With 10 dE/dx measurements, a 2σ separation between kaons and pions can be achieved down to a momentum of 700 MeV/c.
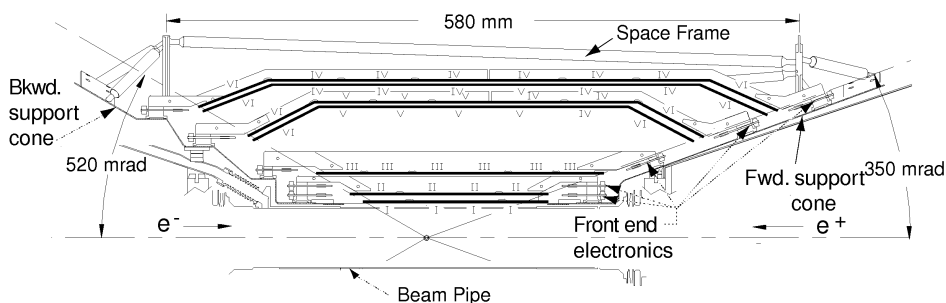
Figure 3.4: Schematic View of SVT: longitudinal section. Roman numerals label the six different types of sensors. The arch design was chosen to minimize the amount of silicon required to cover the solid angle, while increasing the crossing angle for particles near the edges of acceptance.

3.6   Drift Chamber

The primary purpose of the drift chamber (DCH) is to measure the momentum of charged particles. The DCH can provide a set of constraints in order to improve the estimation

---

[5]dE/dx is the energy lost by a particle as it travels through matter.
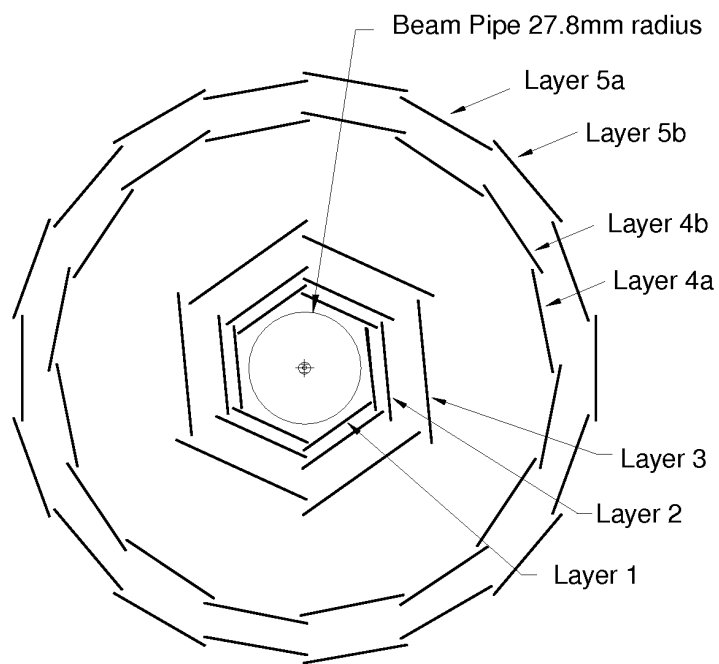
Figure 3.5: Schematic View of SVT: transverse section.

of the track vertex as measured by the SVT. If a particle decays outside the SVT, the reconstruction relies solely on the DCH. The DCH also provides a mechanism to identify particles by measuring ionization loss (dE/dx).

The DCH is designed to track particles with transverse momentum greater than 180 MeV/c. The drift chamber is a 2.80 m long cylinder with an outer radius of 0.809 m, and an inner radius of 0.236 m which encloses the SVT and the beam pipe (see Figure 3.6 for a schematic of the DCH).
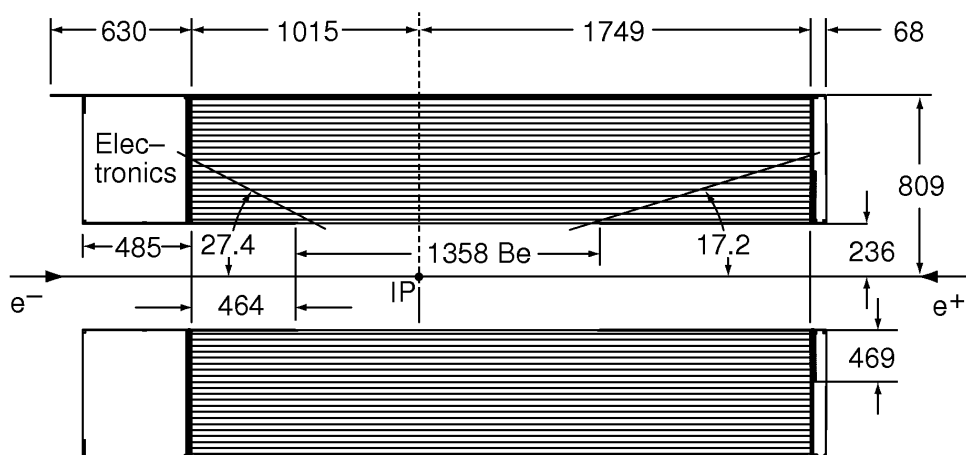
Figure 3.6: Longitudinal section of the DCH showing the principal dimensions.

The DCH contains 7104 hexagonal drift cells (the layout of these cells is shown in Figure 3.7) arranged in 10 superlayers of 4 layers each. The chamber is pressurized with a 4:1 helium/isobutane gas mixture. The electric field lines lie in the $r - \phi$ plane perpendicular to the axial magnetic field. This field is generated by an arrangement of parallel potential wires which surround the signal (anode) wire in the centre of the cell. Roughly half of the signal wires are parallel to the magnetic field (**B**), while others are skewed to run at various stereo angles relative to this axis. This enables a reconstruction of the z position of a track with limited precision. By choosing low-mass wires and a helium-based gas mixture, multiple scattering inside the DCH is minimized[6]. When a charged particle enters the drift chamber

---

[6]If the momentum of the charged particle is less than 1 GeV/c, multiple scattering is significant, and can

Layer		Stereo
16	+ + +	0
15	+ + +	0
14	+ + +	0
13	+ + +	0
12	+ + +	-57
11	+ + +	-55
10	+ + +	-54
9	+ + +	-52
8	+ + +	50
7	+ + +	48
6	+ + +	47
5	+ + +	45
4	+ + +	0
3	+ + +	0
2	+ + +	0
1	+ + +	0

4 cm

+ Sense   ○ Field   ● Guard   × Clearing
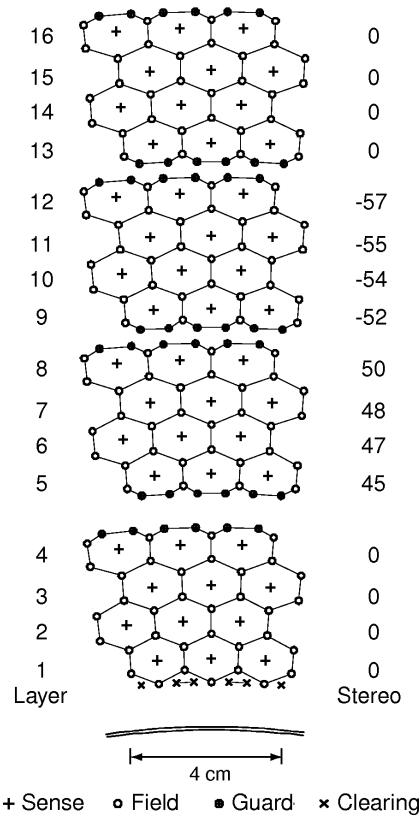
Figure 3.7: Schematic layout of drift cells in the four innermost superlayers. Lines have been added between field wires to aid visualization of cell boundaries. The numbers on the right side indicate the stereo angle of the sensing (sense) wires in milli-radians.

it ionizes the gas and the resulting ionization is detected by the sensing wires which run the entire length of the detector. Additionally, as the particles travel outward, measurements of ionization energy loss are taken (dE/dx). The DCH measures dE/dx with a resolution of 7.5 % and allows for π/K separation up to 700 MeV/c.

3.7   Superconducting Solenoid

The *BABAR* magnet system consists of a superconducting solenoid, a segmented flux return and a field compensating coil. Momentum measurements in the tracking chambers are facilitated by a superconducting solenoid with a magnetic field of 1.5 Tesla in order to achieve the needed momentum resolution for charged particle reconstruction.

3.8   Track Reconstruction

Charged tracks are defined according to five parameters $(d_0, \phi_0, \omega, z_0, \tan(\lambda))$ with associated error matrices. These parameters are measured at the point of closest approach to the z-axis, while d_0 and z_0 define the distance of this point from the origin of the coordinate system in the x-y plane and along the z-axis respectively. The dip angle, λ, is the angle between the track momentum and the transverse plane (x-y plane). The angle ϕ_0 is the azimuth of the track, and $\omega = 1/p_t$ is the track curvature. The track-finding and fitting procedures take into account the distribution of material in the detector and the map of the magnetic field.

The transverse momentum resolution is:

$$\frac{\sigma_{p_t}}{p_t} = 0.13 \pm 0.01 \ \% \cdot p_t + (0.45 \pm 0.03) \ \% \tag{3.1}$$

where the transverse momentum p_t is measured in GeV/c.

be the dominant limitation of track parameter resolution.

3.9   Electromagnetic Calorimeter

At energies well above 10 MeV the interaction of photons and electrons in matter are dominated by pair creation and Bremsstrahlung[7]. Alternating sequences of these interactions lead to a cascade or *shower* of electrons, positrons and photons (see Figure 3.8). As particle energies become smaller other processes such as ionization and Compton scattering also become important.[8]
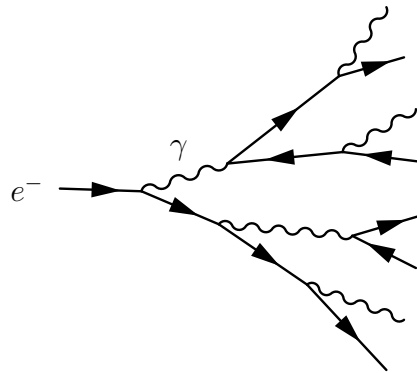
Figure 3.8: Diagram of an Electromagnetic Cascade.

The *electromagnetic calorimeter* (EMC) is designed to measure electromagnetic showers over the energy range from 20 MeV to 9 GeV. It offers excellent efficiency and very good energy and angular resolution.

The EMC is a hermetic total-absorption calorimeter composed of a finely segmented array of thallium-doped cesium iodide (CsI(Tl)) crystals. This type of crystal calorimeter has detection efficiencies close to 100 % when a photon, electron or positron impacts it with an energy above 20 MeV.

The EMC is a cylindrical barrel caped in the forward direction with a crystal readout of silicon photodiodes. Ninety percent coverage of the solid angle is provided in the centre-

---

[7]Bremmstrahlung translates driectly as braking radiation (German); where, *bremsen* means *to brake* and *Strahlung* means *radiation*. Bremsstrahlung is the interaction of an electron or positron with the Coulomb field of a nucleus.

[8]For more details see [24] [38–40].

of-mass system, with $(15.8° − 141.8°)$ coverage in the polar angle and full coverage in the

azimuthal angle. The barrel of the EMC is lined with 5760 trapezoidal CsI(Tl) crystals

arranged in 48 polar-angle rows. The crystals are oriented such that they point towards the

interaction point (IP) and they increase in length from $(16\text{-}17)X_0$[9] in steps of 0.5 X_0 every

7 crystals for $\cos(\theta)$ going from $0 \to 1$. The forward endcap contains 820 crystals, and spans

a solid angle corresponding to $0.893 \leq \cos(\theta) \leq 0.962$ in the laboratory frame.
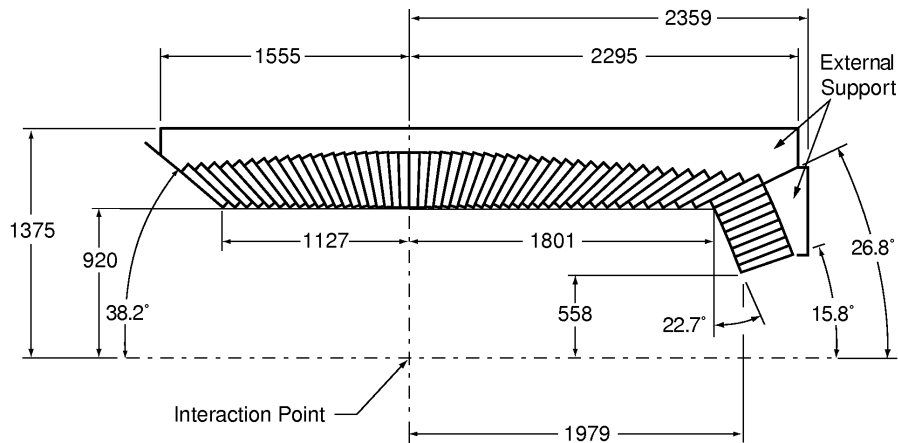
Figure 3.9: A longitudinal cross section of the top half of the EMC. Notice that the detector
is axially symmetrical around the z-axis. All dimensions are in mm.

The energy resolution of a homogeneous crystal calorimeter is given by the empirical

equation [5] [6]:

$$\frac{\sigma_E}{E} = \frac{a}{\sqrt[4]{E(\,\text{GeV})}} \oplus b \tag{3.2}$$

where E and σ_E refer to the energy of a photon and its RMS error, measured in GeV. Further,

the $\oplus$ means that the terms are added in quadrature. Angular resolution is determined by the

transverse crystal size and the distance from the interaction point. It can be parametrized

---

[9]X_0 is known as the radiation length of the material. Radiation length is both (a) the mean distance over
which a high-energy electron loses all but $1/e$ of its energy by Bremsstrahlung and (b) 7/9 of the mean free
path for pair production by a high-energy photon [24].

as the sum of an energy dependent term and a constant term [5,6],

$$\sigma_\theta = \sigma_\phi = \frac{d}{\sqrt{E(\,\text{GeV})}} + e \tag{3.3}$$

where the energy E is measured in GeV.

Parameter	Fit Value (%)	Error (%)
a	2.32	0.30
b	1.85	0.12
Parameter	Fit Value (mrad)	Error (mrad)
d	3.87	0.07
e	0.00	0.04

Table 3.2: EMC Energy and Angular Resolution Parameters [7].

A typical electromagnetic shower spreads over many adjacent crystals, forming clusters of energy deposits. Pattern recognition algorithms are used to distinguish between single clusters with one energy maximum and merged clusters with more than one *local* energy maximum (an energy maximum is commonly referred to as a *bump*). After locating all the bumps in an event, event reconstruction algorithms can determine whether a bump is associated with a charged or a neutral particle.

Electrons are separated from charged hadrons almost exclusively on the basis of the energy measurements from the EMC and the momentum measurements in the DCH. In addition, the measured energy loss and reconstructed Cherenkov angle must be be consistent with an electron. The important variable for discriminating between hadrons and electrons is the ratio of shower energy to the track momentum (E/$|\mathbf{p}|$).

3.10   DIRC and IFR

Another manifestation of the electromagnetic interaction of charged particles in matter is Cherenkov radiation. When the velocity of a charged particle exceeds the velocity of light

in a transparent medium, electromagnetic radiation is emitted.

The *Detector of Internally Reflected Cherenkov light* (DIRC) is used to separate pions and kaons from about 0.5 GeV/c to the kinematic limit of 4.5 GeV/c. Cherenkov radiation is produced in a rectangular quartz bar and it propagates along the bar by total internal reflection thereby preserving the angle of emission. A *cone* of Cherenkov light emerges from the end of the bar and is focused onto an array of photomultipliers. Images of the Cherenkov rings [10] can be reconstructed from the position and time of arrival of the signals in a set of photomultiplier tubes. By measuring both the angle of emission of Cherenkov radiation and the momentum of the charged particle it is possible to reconstruct the particle's mass.

The *steel flux return*, also known as the Instrumented Flux Return (IFR), is used to identify muons and detect neutral hadrons over a wide range of momenta and angles. The IFR uses the flux return of the magnet as a muon filter and hadron absorber. Single gap *Resistive Plate Chambers* (RPCs) with two coordinate readouts serve as detectors; they are installed in the gaps of the segmented steel walls of the barrel and the endcaps of the flux return. There are 19 RPC layers in the barrel and 18 in the endcaps. RPCs are also installed between the electromagnetic calorimeter and the magnet cryostat[11] to detect any particles exiting the EMC. The IFR provides large solid angle coverage, good efficiency and high background rejection for low momentum muons (below 1 GeV/c).

Because deterioration of the RPC performance led to poorer muon identification, the barrel and the forward endcap RPCs of the detector had to be replaced. The degraded RPCs were replaced with improved versions in the forward endcap. The barrel RPCs were replaced with limited streamer tubes (LSTs). Design, layout and performance of the upgraded components is documented in [41].

---

[10]The cone of light associated with the Cherenkov radiation when observed by photomultiplier tubes is a conic section, forming arcs or rings within the detector volume.

[11]Used to maintain low cryogenic temperatures necessary for the superconducting solenoid to produce the 1.5 Telsa magnetic field.

3.11   Event Trigger

The *BABAR* detector has a *tiered* event selection system, commonly known as a *trigger*.
Triggers are associated with various detector elements. The trigger signal causes the detector
information pertaining to these and other subdetectors to be conditionally[12] passed on to
a higher level trigger system and recorded. The design of the trigger systems in *BABAR*
attempts to maximize data-logging efficiency while keeping dead-time to a minimum. The
triggers were originally designed to select events with visible energies close 10.58 GeV, with
high track/cluster multiplicities, or high transverse momentum, or calorimeter energy for
low multiplicity final states.

The *BABAR* trigger system is composed of two independent stages which operate sequen-
tially such that the second stage is conditional upon the first. The first stage is the Level
1 (L1) hardware trigger and the second stage is the Level 3 (L3) software trigger. The L1
trigger interprets incoming detector signals while recognizing and removing beam-induced
backgrounds[13]. L1 event selection is based on data from the DCH, EMC, and IFR and the
L3 software trigger selects events which are to be stored for later processing. The Level 3
(L3) trigger uses complete event data and the L1 trigger information to select or reject an
event[14].

The L1 trigger filters events according to the charged tracks observed in the DCH, showers
detected in the EMC and hits scored in the IFR. The DCH and EMC triggers are primarily
responsible for the identification of physics events in the detector, while the IFR trigger
is responsible for rejecting events from cosmic rays and accepting collision events involving
muons and neutral hadrons. The L3 trigger reconstructs events and classifies them according
to their topology. The reconstructed quantities from the DCH and EMC are subjected to

---

[12]These conditions are often called the event signature.

[13]A small amount of common backgrounds, including beam-induced backgrounds, are accepted by the
trigger for calibration and diagnostic data.

[14]The L3 output rate was initially limited to 120 Hz due to a limitation in the write speed of computer
hard disks.

stringent requirements in order to reduce the amount of possible beam induced backgrounds and Bhabha[15] contamination.

In order to increase the likelihood of observing certain types of new physics processes the trigger was slightly modified during the last running period of *BABAR* operation. A common signature of new physics is events with a large amount of missing energy. Triggering on events with large amounts of missing energy required a shift in trigger *philosophy* such that the trigger was changed to detect signatures which might accompany these *invisible* decays. These hypothetical new physics events were typically expected to deposit less than 10 % of the centre-of-mass energy in the detector; they could have low track and photon multiplicity and many times would involve only two particles per event.[16]

Event Type	Cross Section (nb)	Production Rate (Hz)	L1 Trigger Rate (Hz)
$b\bar{b}$	1.1	3.2	3.2
other $q\bar{q}$	3.4	10.2	10.1
$e^+\ e^-$	53	159	156
$\mu^+\ \mu^-$	1.2	3.5	3.2
$\tau^+\ \tau^-$	0.9	2.8	2.4

Table 3.3: Cross Sections, productions and trigger rates for the principal physics processes at 10.58 GeV for luminosity of $3 \times 10^{33} \mathrm{cm}^{-2}\mathrm{s}^{-1}$. The $e^+\ e^-$ cross section refers to events with either the e^+, e^-, or both inside the EMC detection volume [42]. The instantaneous luminosity of $3 \times 10^{33} \mathrm{cm}^{-2}\mathrm{s}^{-1}$ is equivalent to $3\mathrm{nb}^{-1}\mathrm{s}^{-1}$. The *effective* cross section for Bhabhas is actually lower than 53 nb (small angle scattering events will not be detected, due the nature of the *BABAR* detector, the rough effective cross section is on the order of 25 nb.)

3.12   Event Reconstruction Chain

The reconstruction software uses information from the various subdetectors to reconstruct the basic particle objects, tracks in the SVT and DCH and clusters in the EMC and IFR.

---

[15]$e^+e^- \to e^+e^-$

[16]It was a challenge capture events containing these particles without allowing the trigger rates to exceed the data logging capacity.

Particle identification (PID) algorithms are used to assign probable identities to these parti-
cles. Event reconstruction takes place in three steps in which candidate particles are assigned
physical properties (e.g. momentum, charge, energy, PID).

Track finding involves a simple sequence of pattern recognition algorithms which take each
individual hit in the DCH and SVT and assigns that hit to a single charged particle. The first
stage of pattern recognition is the selection of tracks found in the DCH by the L3 trigger. In
the original version of this algorithm, all L3 tracks with a reasonable helix fit were selected,
while in the final reprocessing, only tracks with hits on at least 25 of the 40 layers and a
reasonable helix were selected[17]. Any hits (or tracks) not accepted are made available for
additional reconstruction algorithms. In addition, the track reconstruction algorithm can
add SVT hits to tracks found in the DCH, and *vice versa*. Roughly 10 % of tracks found by
the reconstruction algorithm are duplicates[18]. Duplicates, fake tracks, and tracks associated
with detector material conversions are suppressed by identification algorithms or *goodness-
of-fit* tests. Charged particles that decay within the tracking detector volume can result in
the track-finding algorithms locating both a *primary* and a *secondary* track. If two tracks
are separated by less than 1 cm and these tracks are both inside the tracking volume (with
the additional requirement that each track's momentum at the vertex point are roughly in
the same direction) the secondary track is considered a daughter particle and removed from
the primary track list.

Discrimination between charged particle types over a large kinematic range is an essential
requirement for precision measurement and the search for rare processes. The five types of
long-lived charged particles of interest are K^+, π^+, e^+, μ^+, and p.[19] Hadrons are distinguished
from each other and from leptons using information from the DIRC and dE/dx measurements
in the DCH and SVT. Muons are differentiated from hadrons through the energy deposition

---

[17]Using a simple goodness-of-fit metric.

[18]The majority of these hits appear to be generated by the same particle.

[19]In order to reduce the amount of necessary exposition, the associated anti-particles, K^-, π^-, e^-, μ^-,
and $\overline{p}$, are also grouped with the positively charged particles listed earlier.

of tracks traversing the EMC and the IFR.

3.13   Simulation of the Detector

The aim of simulation production is to create *Monte Carlo* (MC) *data-sets* which mimic real data as closely as possible while maintaining a theoretically consistent framework. Both the physical properties of a given decay and the propagation of simulated particles through the components of the detector (while modelling all possible interactions) is critical. The following stages of analysis are needed to produce the simulated data:

1. Generation of the underlying physics event;

2. Particle traversal and calculation of the idealized energy deposits in the detector;

3. Overlaying of backgrounds and digitization of the energy deposits; and

4. Reconstruction of the event.

The final step of the simulation is equivalent to that for real data being reconstructed. It takes the synthetic detector output and runs the full reconstruction chain.

3.14   Detector Summary

The luminosity attained at PEP-II makes it possible to attain the statistical sensitivity required to observe rare τ decay modes. Furthermore, the *BABAR* detector permits measurements of common τ decay properties with a precision that rivals or exceeds prior experiments. Although the experiment is optimized for B physics, it is still well suited to perform τ physics in that most of the design choices for making a τ-*factory* are similar to that of a *B-factory*.

Chapter 4

Methodology

This section outlines the methodology used to measure the ratio of $\mathcal{B}(\Upsilon(3S) \to \tau^+\tau^-)$ to $\mathcal{B}(\Upsilon(3S) \to \mu^+\mu^-)$. The individual branching fractions and estimates of the τ and muonic cross sections at $\sqrt{s} = 10.58$ GeV/c^2 are also measured.

4.1 Introduction

This is a *blind analysis* [43], it is designed to avoid the expectation of a 'right' answer from influencing the results and to remove the chance of 'tuning' a selection to emphasize a statistical fluctuation [44].

The *BABAR* collaboration uses a number of different blinding techniques.[1] For this paper the full $\Upsilon(3S)$ data sample was divided into the following three independent groups: `low`, `med`, and `high`. The *early* (`low`) and the *late* (`high`) are two small samples of data available for investigating and estimating statistical and systematic sensitivity of any proposed study. The remaining sample is 'blind' and is only available *after* the *BABAR* collaboration has reviewed and vetted the analysis and approved the *unblinding*. The remaining data is a large blind sample [the full $\Upsilon(2S)$ data sample is blind as well]. The `low` unblinded sample corresponds to 1.154 fb^{-1}of data collected earlier in the $\Upsilon(3S)$ running period (December 2007 and January 2008). The `high` unblinded sample is roughly 1.254 fb^{-1}of data which

---

[1]These include: signal box hiding, data set restrictions, MC treated as pseudo-data.

was collected near the end of the *BABAR* collaboration's data-taking period (February 2008). The blind data sample, also called `med`, corresponds to a luminosity of 25.557 fb^{-1}(or roughly 90 % of all directly produced $\Upsilon(3S)$ events).[2]

Data Set	$\sqrt{s}$ (GeV)	Luminosity (fb^{-1})	Number of τ-pairs
$\Upsilon(4S)$	10.5782	$78.309 \pm 0.017 \pm 0.348$	7.197×10^7
$\Upsilon(4S)$ (off peak)	10.5547	$7.752 \pm 0.006 \pm 0.036$	7.152×10^6
$\Upsilon(3S)$ `low`	10.3552	$1.154 \pm 0.005 \pm 0.007$	1.103×10^6
$\Upsilon(3S)$ `med`	10.3552	$25.557 \pm 0.025 \pm 0.150$	2.442×10^7
$\Upsilon(3S)$ `high`	10.3552	$1.254 \pm 0.006 \pm 0.008$	1.198×10^6
$\Upsilon(3S)$ total	10.3552	$27.963 \pm 0.027 \pm 0.168$	2.672×10^7
$\Upsilon(3S)$ (off peak)	10.3265	$2.623 \pm 0.008 \pm 0.018$	2.519×10^6
$\Upsilon(2S)$	10.0233	$13.599 \pm 0.019 \pm 0.088$	1.380×10^7
$\Upsilon(2S)$ (off peak)	9.9932	$1.419 \pm 0.006 \pm 0.011$	1.448×10^6

Table 4.1: Integrated luminosity of various data sets used in this analysis [1].

Data Set	Estimated Number of $\Upsilon(\mathbf{n}s)$
$\Upsilon(3S)$ `low`	$(5.03 \pm 0.04) \times 10^6$
$\Upsilon(3S)$ `med`	$(111.30 \pm 0.81) \times 10^6$
$\Upsilon(3S)$ `high`	$(5.46 \pm 0.04) \times 10^6$
$\Upsilon(2S)$	$(98.6 \pm 0.9) \times 10^6$

Table 4.2: Estimated number of $\Upsilon(2S)$ and $\Upsilon(3S)$ events produced.

BABAR data was produced and collected during finite operational cycles known as *runs* that are classified and grouped according to specific detector and accelerator configurations. Each run is divided into unique *run numbers* which correspond to a small sub-collection of data.

Detector upgrades and/or component failures produce unique detector responses to be identified and documented. Additionally, large detector upgrades and changes in beam collision energies will correspond to divisions between the labelled operational runs. The largest data-taking run is called `Run 5`, which has a different detector configuration from

---

[2]The blind sample of $\Upsilon(3S)$ is also called `med`.

`Run 6` (centre-of-mass energy corresponding to $\Upsilon(4S)$ events) and `Run 7` (the production of $\Upsilon(2S)$ and $\Upsilon(3S)$).

The blind sample contains roughly 90 % of all $\Upsilon(3S)$ decays and 100 % of $\Upsilon(2S)$ decays. It can be divided into two halves, the first half has similar detector and accelerator conditions to the `low` sample and the second half corresponds with the `high` sample. The integrated luminosity [1] of the blind sample is $25.557 \pm 0.025 \pm 0.150$ fb^{-1}and the early unblind sample luminosity is $1.154 \pm 0.005 \pm 0.007$ fb^{-1}and the late unblind sample is $1.254 \pm 0.006 \pm 0.008$ fb^{-1}. The $\Upsilon(3S)$ off-peak sample luminosity is $2.623 \pm 0.008 \pm 0.018$ fb^{-1}(this sample is also unblinded) and the $\Upsilon(2S)$ on-peak data set has an integrated luminosity of $13.599 \pm 0.019 \pm 0.088$ fb^{-1}and $1.419 \pm 0.006 \pm 0.011$ fb^{-1}of off-peak data.

The following are fundamental measurements in this analysis:

1. $\mathcal{B}(\Upsilon(3S) \to \tau\tau)$; (the branching fraction of $\Upsilon(3S)$ to τ-pairs)

2. $\mathcal{B}(\Upsilon(3S) \to \mu\mu)$; (the branching fraction of $\Upsilon(3S)$ to μ-pairs)

3. $\sigma_{\tau\tau}/\sigma_{\mu\mu}$; (the continuum or QED cross-section ratio at the $\sqrt{s} = m_\Upsilon(4S)$)

4. $\mathcal{R}_{\tau/\mu}$. ($\mathcal{R}_{\tau/\mu} = \mathcal{B}(\Upsilon(3S) \to \tau^+\tau^-)/\mathcal{B}(\Upsilon(3S) \to \mu^+\mu^-)$)

Each of these measurements requires some explanation. The primary term of interest is the number of events which *pass* the appropriate dilepton selection ($N_{\ell^+\ell^-}$), where $\ell \in \{\tau, \mu\}$. This term is a measure of the number of data events which are consistent with the hypothesis that a pair of tracks is equivalent to a pair of muons or τ leptons. Events which are *true* dileptons are called *signal* events and should match the selection criteria with a high probability. Events that *masquerade* as signal events are considered to be *background*. Background in this analysis occurs in two forms that must be identified and distinguished. In the first case there are backgrounds with an equivalent final state, which are produced through a different production mechanism that is of no interest in the analysis and is called

irreducible background.[3] In the second case 'background' has different particle(s) in the final state which are misidentified, this is known simply as background.

In the case of Item 1, $\Upsilon(3S)$ mesons that decay directly to a pair of τ leptons are signal events $(e^+e^- \to \Upsilon(3S) \to \tau\tau)$. Similarly, signal events for Item 2 are $\Upsilon(3S)$ mesons that decay directly to dimuons $(e^+e^- \to \Upsilon(3S) \to \mu\mu)$. In addition to the $\Upsilon(3S)$ mediated interactions, there are also standard *QED* processes $[e^+e^- \to \gamma \to \tau\tau$ (Item 1) and $e^+e^- \to \gamma \to \mu\mu$ (Item 2)]. The QED interactions are examples of *irreducible background* (only $\Upsilon(3S)$ events which decay into dilepton pairs are involved in this study). For Item 3 the signal events are the QED processes, $e^+e^- \to \gamma \to \tau\tau$ and $e^+e^- \to \gamma \to \mu\mu$, and there are no *major* sources of irreducible background.

There is an additional irreducible background factor involved in the measurements of Items 1, 2, and 4. If an $\Upsilon(3S)$ meson decays through an intermediate state, such as $\Upsilon(2S)$ and $\Upsilon(1S)$,[4] (a simple list of some of the possible cascade decay channels can be found in Table 4.3) and when the intermediate state decays to a pair of leptons and transition photons are undetected, the event signature will be nearly identical to the signal mode.

The final number of observed signal events $(e^+e^- \to \Upsilon(3S) \to \ell^+\ell^-$, where $\ell \in \tau, \mu)$ is determined by subtracting the luminosity-scaled continuum[5] $(e^+e^- \to \ell^+\ell^-)$ and all associated backgrounds from the number of observed data events for a particular mode $(\mathbf{i} = \tau\tau \quad \text{or} \quad \mu\mu)$. The signal events are $e^+e^- \to \Upsilon(3S) \to \ell^+\ell^-$, with $e^+e^- \to \gamma^* \to \ell^+\ell^-$

---

[3]The implicit concern over irreducible background can be summarized as follows:

- Often has identical selection requirements on tracks.
- May have a different number of photons in the final state.
- Selection parameters to reduce the acceptance of these events often neuter the selection efficiency of true signal events.

for example if an $\Upsilon(3S)$ was to decay to $\Upsilon(2S)$ (via $\Upsilon(3S) \to \gamma\gamma\Upsilon(2S)$) and both photons are not detected, and the $\Upsilon(2S)$ decayed to dimuons, this would be a type of irreducible background.

[4]These type of decays are called *cascade* decays. Additional modes will involve the χ_b resonance(s). A breakdown of the MC generated decays is found in Table B.3, B.4, and B.5.

[5]Events that are produced through a purely electromagnetic interaction are called QED or continuum events.

$\Upsilon(3S) \to \gamma\gamma\Upsilon(2S)$
$\Upsilon(3S) \to \gamma\gamma\Upsilon(1S)$
$\Upsilon(2S) \to \gamma\gamma\Upsilon(1S)$
$\Upsilon(3S) \to \gamma\chi_{b_2}(2\text{P})$
$\Upsilon(3S) \to \gamma\chi_{b_1}(2\text{P})$
$\Upsilon(3S) \to \gamma\chi_{b_0}(2\text{P})$
$\Upsilon(3S) \to \gamma\chi_{b_2}$
$\Upsilon(3S) \to \gamma\chi_{b_1}$
$\Upsilon(3S) \to \gamma\chi_{b_0}$
$\chi_{b_2}(2\text{P}) \to \gamma\Upsilon(2S)$
$\chi_{b_1}(2\text{P}) \to \gamma\Upsilon(2S)$
$\chi_{b_0}(2\text{P}) \to \gamma\Upsilon(2S)$
$\chi_{b_2}(2\text{P}) \to \gamma\Upsilon(1S)$
$\chi_{b_1}(2\text{P}) \to \gamma\Upsilon(1S)$
$\chi_{b_0}(2\text{P}) \to \gamma\Upsilon(1S)$
$\chi_{b_2} \to \gamma\Upsilon(1S)$
$\chi_{b_1} \to \gamma\Upsilon(1S)$
$\chi_{b_0} \to \gamma\Upsilon(1S)$

Table 4.3: Listing of a few of the cascade decay channels.

are irreducible background (and commonly called continuum background). This can be written as a background subtraction (where continuum τ-pairs or dimuon events are seen as *irreducible* background):

$$N^{\text{Observed}}(\mathbf{i}) = N^{\text{Data}}(\mathbf{i}) - \sum_j \text{bkg}(i, j) \tag{4.1}$$

where, $N^{\text{Data}}(\mathbf{i})$ is the number of selected data events for one of the selection channels (in this case labelled i), and $\text{bkg}(i, j)$ is the number of expected backgrounds of type $\mathbf{j}$ that are selected as mode $\mathbf{i}$.

4.1.1 τ Background Sources

- $e^+e^- \to \mu^+\mu^-$: The production mechanisms are identical for μ- and τ-pairs except in instances near the τ production threshold where phase space suppression due to the τ mass is relevant. In τ-pair events, a pair of back-to-back τ leptons are produced, each having half the total beam energy. Both τ-lepton decays occur independently inside

the beam pipe. As muons are '*stable*'[6] at this energy, a pair of highly energetic back-to-back tracks appearing in the detector and passing through the calorimeter while leaving only a small deposit of energy is the event signature for dimuons.[7]

- **$e^+e^- \rightarrow e^+e^-$:** With respect to electron pairs, the s-channel production is the same for all lepton pair production (see Figure 4.1b) and there is an additional t-channel reaction (or *scattering reaction*, see Figure 4.1a) that produces a pair of back-to-back electrons with full beam energy. The cross section for the s-channel process is similar to τ and muon production, contrasting with the t-channel reaction and exhibiting a huge cross-section, particularly in the forward direction (also known as *small angle scattering*). This is a dominant interaction at *BABAR*. Like dimuons, the Bhabha interaction produces a pair of highly energetic back-to-back tracks in the detector. Both tracks are associated with large energy deposits in the electromagnetic calorimeter[8].

- **$e^+e^- \rightarrow q\overline{q}$:** Fragmenting quarks ($u$,$d$, and s) produce hadrons, typically in large numbers, which can be used to distinguish these events from τ-pairs and there can also be events with low multiplicity (which would be background to τ events). Average multiplicity tends to increase with increasing centre-of-mass energy and there is also an increasing separation between the individual hadronic tracks (hadronic events are described as being more 'spherical' than τ events)[9].

- **Two-photon events ($e^+e^- \rightarrow e^+e^-\mathbf{f\overline{f}}$):** Two-photon events occur when an initial electron and a positron undergo a small deflection caused by a photon exchange (often when neither the electron nor the positron enters the detector volume) and also when

---

[6]The lifetime of a muon is long enough for it to travel through all the detector material before it decays.

[7]Muons at the GeV energy scale are commonly described as minimally ionizing and penetrating particles.

[8]Due to the small mass of the electron, the energy loss of the electron and positron, dE/dx is dominated by Bremsstrahlung and as such these tracks deposit all of their energy within a few radiation lengths (X_0)

[9]The cross section for hadron production is larger than for τ-pair production; the larger cross section is due to the number of quark flavours and the fact that initial quark flavours can have one of three colour charges.

a photon produces a pair of fermions ($\bar{f}f$) which may enter the detector. If neither electron nor positron enter the detector volume, the fermion pair is typically produced with *low mass* and low $\mathbf{p_t}$ with respect to the beam. Two-photon events are unlikely to produce τ-pairs and heavy quarks. But since a τ lepton can decay into other fermions, this type of event can appear as background within a τ selection. A Feynman diagram of the two-photon process is shown in Figure 4.2.
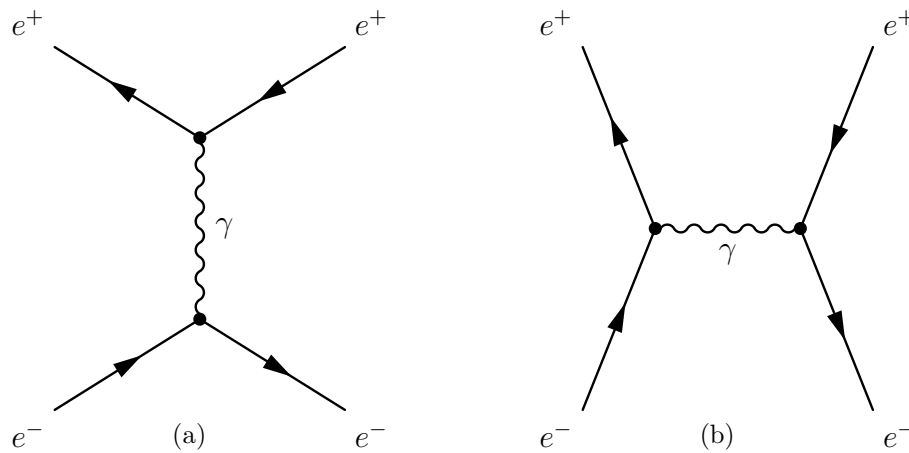
Figure 4.1: Lowest order Feynman diagrams of the possible background production of any τ event. (a) t-channel Bhabha scattering. (b) s-channel or annihilation channel for Bhabha scattering.
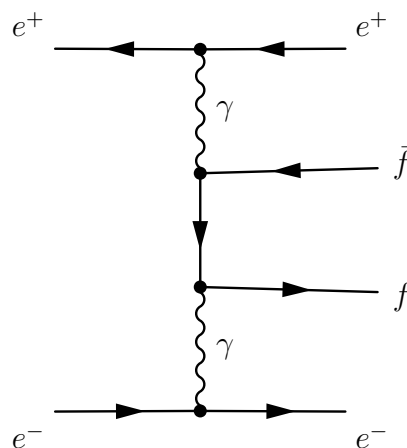
Figure 4.2: Lowest order Feynman diagram of a two-photon event, where f can be a fermion ($f \in \{e^-, \mu^-, \tau^-, u, d, c, s\}$) or this could be a composite system (like π^0, π^+).

4.1.2   Dimuon Background Sources

- **$e^+e^- \to \tau\tau$**: Since the final state of a τ-lepton decay can include a muon with an undetectable pair of neutrinos these events can be considered background to dimuon events as long as the neutrinos carry only a small amount of energy. There is only a small likelihood of this since, in the majority of τ lepton decays, it can be expected that the τ energy will be roughly evenly divided among the decay products.

- **$e^+e^- \to q\bar{q}$**: Hadronic events with one π^- and one π^+ mesons sometimes are indistinguishable from dimuon events when there are no additional hadrons present. Even without neutral hadrons in the final state, pions are far more likely to deposit energy in the electromagnetic calorimeter due to the nature of the strong interaction which can occur between the constituent quarks in both the nucleus and the π mesons. However do to the stocastic behaviour of energy deposition, a pion can deposit small amounts (comparable to that of what a typical muon might deposit), or in other words, the $\pi^\pm$ meson can be misidentified as muon.

- **Bhahbas ($e^+e^- \to e^+e^-$)**: There is a small chance that an electron will be misidentified as a muon. The more likely scenario is that the electron (or positron) will not actually collide with active detector material in the EMC therefore identification algorithms cannot determine the particle types.

- **Two-photon events ($e^+e^- \to e^+e^-f\bar{f}$)**: These can also produce dimuons with reduced momentum.

4.2   Experimental Observables

The branching fraction of $\Upsilon(3S) \to \tau^+\tau^-$ is given by,

$$\mathcal{B}_{\Upsilon(3S)\to\tau^+\tau^-} = \frac{N^{\Upsilon(3S)\to\tau\tau}}{N^{\Upsilon(3S)}} \tag{4.2}$$

$$= \frac{N^{\text{Observed}} - N^{\text{background}} - N^{\text{continuum}}}{N^{\Upsilon(3S)}} \tag{4.3}$$

Using equation (2.22) as a guide, additional parameters must be included

$$\mathcal{B}_{\Upsilon(3S)\to\tau^+\tau^-} = \frac{N_{\text{Data}} - N_{\Upsilon(3S)}^{\text{Background}} - N_{\tau\tau}^{\text{off}} \frac{\varepsilon^{\text{on}}\mathcal{L}_{\text{on}}\sigma_{\text{on}}^{\tau\tau}}{\varepsilon^{\text{off}}\mathcal{L}_{\text{off}}\sigma_{\text{off}}^{\tau\tau}}}{\varepsilon^{\text{3S}}\mathcal{L}\sigma^{\text{3S}}} \tag{4.4}$$

The term $\delta^{\text{interference}}$ has been omitted[10] and σ^{3S} is the $\Upsilon(3S)$ cross-section, $\mathcal{L}$ is the associated integrated luminosity of the on-peak $\Upsilon(3S)$ dataset (see Table 4.1 and Table 4.2). The term $\mathcal{L}\sigma^{\text{3S}}$ can be replaced by the total estimated number of produced $\Upsilon(3S)$ mesons. The associated background $(\sum_j \text{bkg}(\mathbf{i}, \mathbf{j}))$ corrections are eliminated for clarity.

In fact, the term of greatest interest is the ratio $\mathcal{R}_{\tau/\mu} = \mathcal{B}(\Upsilon(3S) \to \tau\tau)/\mathcal{B}(\Upsilon(3S) \to \mu\mu)$. To measure this it is necessary to start with the individual branching fractions $\Upsilon(3S) \to \mu\mu$ and $\Upsilon(3S) \to \tau\tau$. Noting that both are divided by the total number of $\Upsilon(3S)$ produced (or equivalently, the production cross section multiplied by the observed luminosity).

$$\mathcal{B}(\Upsilon(3S) \to \tau\tau) = \frac{N_{\tau\tau}^{\text{obs}} - b_{\tau\tau}^{\Upsilon(3S)} - N_{\tau\tau}^{\text{off}} \frac{\mathcal{L}_{\text{on}}\sigma_{\text{on}}\varepsilon_{\text{on}}}{\mathcal{L}_{\text{off}}\sigma_{\text{off}}\varepsilon_{\text{off}}}}{N_{\Upsilon}(3S)} \tag{4.5}$$

$$\mathcal{B}(\Upsilon(3S) \to \mu\mu) = \frac{N_{\mu\mu}^{\text{obs}} - b_{\mu\mu}^{\Upsilon(3S)} - N_{\mu\mu}^{\text{off}} \frac{\mathcal{L}_{\text{on}}\sigma_{\text{on}}\varepsilon_{\text{on}}}{\mathcal{L}_{\text{off}}\sigma_{\text{off}}\varepsilon_{\text{off}}}}{N_{\Upsilon}(3S)}, \tag{4.6}$$

where $N_{\tau\tau}^{\text{off}}$ means the measured number of τ pair events associated with off $\Upsilon(3S)$ resonance

---

[10]Due to the nature of Quantum Mechanics, if the final state can be synthesized by two different reaction channels, there can be interference between the two channels. This interference term is much smaller when compared with the two original reaction channels. In this case, the interference channel would be the interference between $e^+e^- \to \Upsilon(3S) \to \mu^+\mu^-$ and $e^+e^- \to \gamma* \to \mu^+\mu^-$; as well there would be a separate interference term $e^+e^- \to \Upsilon(3S) \to \tau^+\tau^-$ and $e^+e^- \to \gamma* \to \tau^+\tau^-$. The interference δ_τ and δ_μ should have an associated systematic error that is 100 % correlated (except for a small effect due to differences in mass between the τ lepton and the muon).

production, $b_{\mu\mu}^{\Upsilon(3S)}$ and $b_{\tau\tau}^{\Upsilon(3S)}$ are the estimated background contamination, and

$$N_{\Upsilon}(3S) = \sigma_{\Upsilon(3S)}\mathcal{L} \tag{4.7}$$

$$= (121.78 \pm 0.89) \times 10^6 \text{ [1]} \tag{4.8}$$

A correction for efficiency is needed when scaling $\Upsilon(4S)$ to $\Upsilon(3S)$ ($\sqrt{s} \approx 10.58$ GeV $\rightarrow$ 10.3552 GeV) which appears as the ratio ($\varepsilon_{\text{on}}/\varepsilon_{\text{off}}$). This correction is required because of the following:

1. The acceptance has changed;

2. Tracking improves with lower p_{T};

3. Energy reconstruction improves with slightly higher energies;

4. There is increased photon multiplicity at higher energies;

5. Lower boost means the chance of merging photons from $\pi^0 \rightarrow \gamma\gamma$ is reduced (more likely to find π^0); and

6. There is an increase in the mean number of hadrons produced during hadronic fragmentation.

In place of using the $\Upsilon(3S)$ off-peak data sample for subtracting off-continuum dilepton events, it is possible to use the dimuon and τ-pair events collected at $\Upsilon(4S)$ energy because $\Upsilon(4S) \rightarrow \ell^+\ell^-$ is negligible. It is best to use only $\Upsilon(4S)$ events from `Run 6` due to detector similarities and because there is the smallest temporal separation between $\Upsilon(4S)$ and $\Upsilon(3S)$ running periods and the systematic errors will be similar. Using continuum events from `Run 6` corresponds with roughly 80 fb^{-1}, as opposed to the 2.6 fb^{-1} for off-peak $\Upsilon(3S)$. Starting with an estimated statistical component of N$^{\text{off}}$ of 3.0 % for $\Upsilon(3S)$ off-peak, this scales down by a factor of $\sqrt{2.6/80}$ (or it would be reduced by roughly 80 %, to 0.55 %).

Lepton Pair	$\sqrt{s}$ (GeV)	Name	σ_{theory} (nb)
e^+e^-	9.9932	$\Upsilon(2S)$ off-peak	25.803 ± 0.067
e^+e^-	10.0233	$\Upsilon(2S)$ on-peak	25.804 ± 0.067
e^+e^-	10.3265	$\Upsilon(3S)$ off-peak	25.771 ± 0.067
e^+e^-	10.3552	$\Upsilon(3S)$ on-peak	25.756 ± 0.067
e^+e^-	10.5547	$\Upsilon(4S)$ off-peak	25.290 ± 0.067
e^+e^-	10.5782	$\Upsilon(4S)$ on-peak	25.073 ± 0.067
$\mu^+\mu^-$	9.9932	$\Upsilon(2S)$ off-peak	1.2768 ± 0.0056
$\mu^+\mu^-$	10.0233	$\Upsilon(2S)$ on-peak	1.2695 ± 0.0056
$\mu^+\mu^-$	10.3265	$\Upsilon(3S)$ off-peak	1.2019 ± 0.0053
$\mu^+\mu^-$	10.3552	$\Upsilon(3S)$ on-peak	1.1941 ± 0.0053
$\mu^+\mu^-$	10.5547	$\Upsilon(4S)$ off-peak	1.157 ± 0.0050
$\mu^+\mu^-$	10.5782	$\Upsilon(4S)$ on-peak	1.147 ± 0.0050
$\tau^+\tau^-$	9.9932	$\Upsilon(2S)$ off-peak	1.0203 ± 0.0033
$\tau^+\tau^-$	10.0233	$\Upsilon(2S)$ on-peak	1.0148 ± 0.0033
$\tau^+\tau^-$	10.3265	$\Upsilon(3S)$ off-peak	0.9604 ± 0.0031
$\tau^+\tau^-$	10.3552	$\Upsilon(3S)$ on-peak	0.9556 ± 0.0031
$\tau^+\tau^-$	10.5547	$\Upsilon(4S)$ off-peak	0.9226 ± 0.0030
$\tau^+\tau^-$	10.5782	$\Upsilon(4S)$ on-peak	0.9189 ± 0.0030

Table 4.4: Charged lepton cross section. The cross section was simulated using KK2F and BABAYAGA. The dimuon cross section are from [1]; the quoted error from [1] is given the same relative uncertainty as (1.147 ± 0.005) nb (the value determined by Banerjee *et. al.* [18]). The error on the τ cross section is set to have the same relative uncertainty as (0.919 ± 0.003) (which is larger than the estimated as estimated by KK2F) [18].Details of the simulation can be found in Appendix C. There is an acceptance cut for Bhabha events, which requires that the electron and positron are restricted to between $30 < \theta^{\text{CM}} < 150°$ (where θ^{CM} is the polar angle in the centre-of-mass frame).

The advantages of using Equation (4.5) and Equation (4.6) with $\Upsilon(4S)$ for background subtraction instead $\Upsilon(3S)$ off-peak data are as follows: First, there is no need to rely on the small sample size associated with the τ leptons in both *on-* and *off*-peak since only one sample ($N_{\tau\tau}^{\Upsilon(3S)}$) is required.[11] Second, this form reduces the largest statistical error due to the background subtraction associated with the direct determination of $\mathcal{B}(\Upsilon(3S) \to \tau\tau)$.

The τ event selection requires that the each τ lepton will decay to only one charged track and one or more unobserved neutrinos. Although the τ lepton can decay to states with three and five charged particles, the single charged particle decays are ideal because the total systematic error should be smaller. These decays can be classified into groups according to their daughter particles (one for the τ^- and one for the τ^+)[12]. For example, suppose that the τ^- decayed to $\mathbf{X}^-\nu_\tau$ and the τ^+ decayed to $\mathbf{Y}^+\nu_\tau$ the event would fall into a class denoted [$\mathbf{XY}$] or [$\mathbf{YX}$]. Although there is a small difference in the detection efficiency for electrons and positrons (similarly for μ^+ and μ^-, π^+ and π^-, K^- and K^+), these τ decay classifications are congruent and [$\mathbf{XY}$] is the same as [$\mathbf{YX}$]. It is necessary to classify these decays because the systematic errors and backgrounds for a decay such as $\tau^- \to \mu^-\nu_\tau\overline{\nu}_\mu$ are different than the decay $\tau^- \to \rho^-\nu_\tau$.[13] The branching fractions of τ^- to $e^-\ \nu_\tau\ \overline{\nu}_e$, $\mu^-\ \nu_\tau\ \overline{\nu}_e$, $\pi^-\ \nu_\tau$, and $\rho^-\nu_\tau$ are $(17.85\pm0.05)\times10^{-2}$, $(17.36\pm0.05)\times10^{-2}$, $(10.91\pm0.07)\times10^{-2}$, and $(25.51\pm0.09)\times10^{-2}$ respectively [24]. This analysis requires that one track pass an electron selector[14] and the other track be consistent with 'not' an electron (in other words failing the same electron

---

[11]In this case, on-peak means running near or slightly above an $\Upsilon(\mathbf{nS})$ resonance. Off-peak refers to any set of events that are purely QED or continuum produced τ-pairs or μ pairs; For example, the $\Upsilon(4S)$ resonances decay almost exclusively to $B\overline{B}$; in fact its decay rate to leptons is less than 1.56×10^{-5} [12]. It follows that running at the $\Upsilon(4S)$ will produce events which are identical to continuum production.

[12]Ignoring neutrinos

[13]ρ^- decays primarily through the hadronic decay $\rho^- \to \pi^-\pi^0$. To identify any ρ^- events would require the observation of two photon clusters which are consistent with a π^0 and the observation of a π^-. The identification of a π^0 introduces a systematic error of about 0.9 % in selection signal efficiency.

[14]An electron selector is a set of predefined and tested criteria used to distinguish between tracks which are said to be equivalent to an electron. There are a number different classification types and thresholds for selectors, including low 'fake' rate, high selection efficiency, and/or high purity. The electron selector used in this analysis is detailed in A.1, which has an electron identification efficiency determined to be above 90 % for momenta above 0.5 GeV/c in the laboratory frame, while the pion fake rate is below 0.1 %.

selector). This event type is denoted $[e\not{e}]$, and is designated *electron-not electron* selection. Such a selector is roughly equivalent to the union of selectors $[e\mu]\cup[e\pi]\cup[e\rho]\cup[eK]$ (with the advantage of grouping the individual particle types of the second track, instead of requiring a full identification and introducing additional systematics due the requirements on different particle identification and neutral reconstruction). The non-electron track is given the mass of a π^-. By using $[e\not{e}]$ selection there is a large reduction in contamination due to Bhabhas and two photon events. Additional selectors can be used to identify tracks which are muons, pions, or kaons (but this reduces the selection efficiency by a large amount and suffers from potential contamination due to misidentification).

Dimuon selection efficiency may exhibit similar systematic errors as τ decays (primarily due to the similar nature of the decay products being separated into hemispheres) but the ratio of efficiencies can also lead to a cancellation of specific systematic errors. There is a caveat, if a particular systematic error has a dependence on the a track's laboratory momentum, it might be expected that the track associated with τ decay will have, on average, a significantly lower momentum than a muon produced during muon-pair events such that cancellation of systematic errors will not occur. Therefore, a full investigation of all systematics must be done independently and applied to both distributions.

4.3   Data

With respect to the data sample at the $\Upsilon(3S)$ resonance, the continuum cross-section is $\sigma_{e^+e^-\to\tau^+\tau^-} = (9.550\pm0.024)\times10^{-1}$ nb and $\sigma_{e^+e^-\to\mu^+\mu^-} = (1.1958\pm0.0030)$ nb, determined to high precision using the KK Monte Carlo (MC) generator. Initially the *BABAR* collaboration measured the $\Upsilon(3S)$ cross-section to be 4.19±0.19 nb. The total estimated number of $\Upsilon(3S)$, $N_{\Upsilon(3S)} = (79.62\pm0.78)\times10^6$ (for period 1) and $N_{\Upsilon(3S)} = (42.16\pm.42)\times10^6$ (for period 2) and this value can be used in place of $\mathcal{L}\sigma_{\Upsilon(3S)}$ [1]. The error here is the systematic contribution since the statistical error is negligible in comparison. The effective number of

$\Upsilon(3S)$ and $\Upsilon(2S)$ events produced can be used to estimate the cross section of the respective resonances. Reference [1] gives $(79.62 \pm 0.78) \times 10^6$ and $(42.16 \pm 0.42) \times 10^6$ for period 1 and period 2 respectively. This will reduce the effective error to 1 % from 5 % and this value is highly correlated with the luminosity error and the theoretical cross-section errors. Using the estimated number of $\Upsilon(3S)$ events and the luminosity, the effective cross section, $\sigma_{\Upsilon(3S)} = N_{\Upsilon(3S)}/\mathcal{L} = ((79.62 \pm 0.78) \times 10^6 + (42.16 \pm 0.42) \times 10^6)/27.963 \pm 0.027 \pm 0.168 \text{ fb}^{-1} = 4.355 \pm 0.031 \pm 0.026$ nb (where statistical error has been added in quadrature); yields a result which is in contrast to, but consistent with and more precise than the earlier measured value of $(4.19 \pm 0.19$ nb). Additionally, the $\Upsilon(2S)$ cross section was originally estimated to be 7.32 nb with an error of roughly 4.5 %, again using the BAD 2186 numbers, $(98.6 \pm 0.9) \times 10^6/(13.599 \pm 0.019 \pm 0.102 \text{ fb}^{-1}) = 7.251 \pm 0.067 \pm 0.054$ nb.

Signal events are simulated using KK [45] and TAUOLA [46,47] with a fixed set of τ branching fractions[15]. The $\tau^+\tau^-$ background processes are simulated by KK [48](dimuons) while the $q\bar{q}$ processes are simulated with Jetset7.4 [49] and EvtGen [50] [51]. Radiative corrections for all processes are simulated using PHOTOS [52]. The detector response to generated particles is simulated using GEANT 4 [53]. Simulated events were used to establish the selection criteria, estimate the systematic uncertainties and estimate the background rates, as well as provide a mechanism to determine efficiencies.

For Bhabha events, $e^+e^- \to e^+e^-(\gamma)$, the BHWIDE generator is used with an additional cut, restricting simulated and detected tracks in the lab frame to within $17.93 < \theta < 131.06°$, where θ is the polar angle, the minimal track energy is 0.1 GeV, and the number of photons is required to be 10 or less. The cross-section for Bhabhas is calculated by the event generator BABAYAGA[16] and $e^+e^- \to \gamma\gamma$ events are simulated using the BKQED generator.

These Monte Carlo generators are used to estimate the cross sections of all background

---

[15]The branching fractions are from PDG [12,24].

[16]Section C.3, with the additional requirements of track polar angle (θ) in the range $30 < \theta < 150°$, lepton energy greater than 0.1 GeV, and a minimal photon energy of 0.1 MeV. The number of photons generated is not restricted.

modes. Further, in order to produce comparison plots between data and simulated events, a scaling weight has to be estimated. Using the number of events generated, the luminosity and the estimated cross section, the scaling weight is defined as:

$$\omega(\mathbf{i}) = \frac{\mathcal{L}\sigma(\mathbf{i})}{N_{\text{gen}}(\mathbf{i})}. \tag{4.9}$$

Type	$\sqrt{s}$ (GeV)	*BABAR* Monte Carlo Number (Full Alias)	N_{GEN}	Generator
$\tau^+ \tau^-$	10.3265	3429 (SP-3429-Run7-Y3S_OffPeak-R24)	6.5×10^6	KK2F & TAUOLA
$\mu^+ \mu^-$	10.3265	3981 (SP-3981-Run7-Y3S_OffPeak-R24)	20×10^6	KK2F
$e^+ e^-$	10.3265	2400 (SP-2400-Run7-Y3S_OffPeak-R24)	44×10^6	BHWIDE
uds	10.3265	998 (SP-998-Run7-Y3S_OffPeak-R24)	15^6	EvtGen
$c\bar{c}$	10.3265	1005 (SP-1005-Run7-Y3S_OffPeak-R24)	23×10^6	EvtGen
$\tau^+ \tau^-$	10.5782	3429 (SP-3429-Run6-R24)	140×10^6	KK2F & TAUOLA
$\mu^+ \mu^-$	10.5782	3981 (SP-3981-Run6-R24)	94×10^6	KK2F
$e^+ e^-$	10.5782	2400 (SP-2400-Run6-R24)	81×10^6	BHWIDE
uds	10.5782	998 (SP-998-Run6-R24)	327×10^6	EvtGen
$c\bar{c}$	10.5782	1005 (SP-1005-Run6-R24)	209×10^6	EvtGen
$\tau^+ \tau^-$	10.3552	3429 (SP-3429-Run7-Y3S_OnPeak-R24)	57×10^6	KK2F & TAUOLA
$\mu^+ \mu^-$	10.3552	3981 (SP-3981-Run7-Y3S_OnPeak-R24)	82×10^6	KK2F
$e^+ e^-$	10.3552	2400 (SP-2400-Run7-Y3S_OnPeak-R24)	368×10^6	BHWIDE
$\Upsilon(3S)$	10.3552	8739 (SP-8739-Run7-Y3S_OnPeak-R24)	257×10^6	EvtGen
uds	10.3552	998 (SP-998-Run7-Y3S_OnPeak-R24)	153×10^6	EvtGen
$c\bar{c}$	10.3552	1005 (SP-1005-Run7-Y3S_OnPeak-R24)	191×10^6	EvtGen

Table 4.5: MC Data Set Definitions.

4.4   Event Selection

$\Upsilon(3S) \to \tau^+\tau^-$ and $\Upsilon(3S) \to \mu^+\mu^-$ event selection begins by choosing those events which have a shape consistent with the kinematic constraint from $e^+e^- \to \tau^+\tau^-(\gamma)$ and $e^+e^- \to \mu^+\mu^-(\gamma)$ respectively.[17] All events are required to have two well-reconstructed tracks with opposite charges.[18] In the $\tau^+\tau^-$ case, one of the τ decays must be a track identified as an electron (see Figure 2.3), while the other τ decay, neglecting neutrinos, is reconstructed from a single charged track and restricted to be 'not an electron'. In addition, the $\tau^+\tau^-$ decay modes are classified and investigated: $[e\mu]$, $[\mu\mu]$, $[e\pi]$, and $[\mu\pi]$. Further $[ee]$ decays are not considered because the large Bhabha $(e^+e^- \to e^+e^-)$ cross-section results in a lot of background (in addition to contamination from two photon events[19] as well as photonic conversions). The highest effective selection rate is produced by the $[e\not{e}]$ selector. This selector achieves results that are reasonably separated from all major background modes except for contamination from Bhabha events (where one of the electrons or positrons has not been identified correctly).

4.4.1   Pre-selection

To allow for a *common* pre-selection, the *BABAR* collaboration defines a subset of all events, called a 'skim'. Skims are used to select events with a specific physics signature or decay topology. The event selection of τ- (and μ)-pair events begins with the *BABAR* τ skims. The [1-1] τ-skim is designed to keep μ- and τ-pair events which are consistent with a [1-1] topology (an event is said to have [1-1] topology if the tracks can be isolated into separate hemispheres in the centre-of-mass system). Other τ skims are designed to keep τ-pair events

---

[17]The $e^+e^- \to \Upsilon(3S) \to \ell^+\ell^-$ should have nearly identical kinematics to $e^+e^- \to \gamma \to \ell^+\ell^-$ (see Figure 2.2). The primary difference is that the QED or continuum production can undergo an emission of initial state radiation. Emission of initial state radiation cannot occur in the $\Upsilon(3S)$ production mode (assuming the total beam energy is only slightly above the $\Upsilon(3S)$ mass).

[18]Tracks that appear to be associated with a photon conversion are not considered. Photonic conversion comes about through pair production of two oppositely charged particles when a photon interacts with detector material $\gamma^\star \to t^+t^-$ (where t is a track); usually this produces electron-positron pairs.

[19]See Figure 4.2.

classified with [3-3], or [1-N] (N $\geq$ 3) events. An event with [1-N] or [3-3] topology can be reclassified as a [1-1] τ-pair (or μ-pair) event if the additional tracks are consistent with photon conversions.[20] A collection of filters, called background filters, are available to provide a consistent methodology of event selection and reduce backgrounds for particular physics analysis (these are called background filters or **BGF**). The initial starting point for a number of skims is a simple set of background filters.

Events in the dimuon sample are required to pass the *BABAR* background filter, **BGF-MuMu**. Events in the τ-pair sample are required to pass either of **BGFTau** or **BGFTwoProng**. These requirements are designed primarily to reduce the number of Bhabha events and the contamination of dimuons and two-photon events in the τ-pair selection (and similarly the number of τ leptons in the dimuon sample). The **BGFTau** filter uses good reconstructed tracks and considers a calorimeter cluster to be associated with a track if it is within 100 mrad in θ of the track, and a has lateral moment less than 0.8. In addition, it requires the following:

- Distance of closest approach of any track vertex (with respect to the beam spot) in the $x - y$ plane to be less 1 cm;

- Distance of closest approach of any track vertex (with respect to the beam spot) in the z plane to be less 4 cm;

- Two tracks;

- Tracks to have opposite charge;

- $\sum_i |\mathbf{p}_i^{\mathrm{CM}}| < 9.0$ GeV/c;

- $\sum_i \mathrm{E}_i < 5.0$ GeV;

---

[20]A photon conversion involves a high energy photon interacting within the detector material before the EMC and causes the pair production of an electron-positron pair, written symbolically as: $\gamma* \to e^+e^-$.

- One track has $E_i/|\mathbf{p}_i^{cm}| < 0.8$;

- $\mathbf{p}_\perp^{CM}/(\sqrt{s} - |\mathbf{p}_1^{CM}| - |\mathbf{p}_2^{CM}|) > 0.07$[21];

where $\mathbf{p}_i^{CM}$ is the centre-of-mass momentum of the ith ($i \in \{1, 2\}$) track, E_i is the calorimeter energy associated with the track, and $\mathbf{p}_\perp^{CM}$ is the transverse momentum (orthogonal to the beam direction). The **BGFTau** filter provides high efficiency and a reasonably high purity preselection for simple [1-1] τ-pair events. The **BGFMuMu** filter uses good reconstructed tracks and requires the following:

- Two Tracks;[22]

- $|\mathbf{p}_1^{CM}| > 4.0$ GeV/c and
  $|\mathbf{p}_2^{CM}| > 2.0$ GeV/c;

- $2.8 < \sum_i \theta_i < 3.5$ radians ;

- $\sum_i E_i^{ECM} < 2.0$ GeV;

where, $\mathbf{p}_i^{CM}$ is the centre-of-mass momentum, E_i^{ECM} is the energy associated with a track, and θ_i is the polar angle of the ith track in the centre-of-mass frame. Finally **BGFTwoProng** selection has a large overlap with **BGFTau** selection described above. Events with the following will pass **BGFTwoProng**:

- Two Tracks;

- $E_i^{ECM} < 3.0$ GeV;

- The track with higher momentum (in the centre-of-mass) is required to have a lab polar angle (θ) greater than -0.75 radians (roughly equivalent to the track being in the acceptance of EMC);

---

[21]The denominator must be greater than 0 GeV. This last cut is designed to reduce two photon events, which often have more balanced transverse momentum than τ events.

[22]There is no total charge requirement.

- $\sum_i |\theta_i^{\mathrm{LAB}}| > 0.1$ radians;

- $|\mathbf{p}_\perp| > 4.0$ GeV/c for one of the tracks **or**

  $\left| |\mathbf{p}_1|_\perp - |\mathbf{p}_2|_\perp \right| < 0.3$ GeV/c;

where, $p_\perp$ is the transverse momentum of the event, θ_i is the ith's track polar angle and $\mathrm{E}_i^{\mathrm{ECM}}$ is the ith's track measured deposit of calorimeter energy.

In addition to the topology filters and simple physics filters, there are detector level triggers that events have to pass in order to be selected and stored in the data acquisition stage. For an event to be considered in the analysis, the level-3 (or software) trigger in either the drift chamber or electromagnetic calorimeter is required to be consistent with a physics event.

The muons produced in $e^+e^- \rightarrow \mu^+\mu^-(\gamma)$ should be back-to-back in the centre-of-mass frame,[23] whether produced electromagnetically or through a $\Upsilon(3S)$ meson. At centre-of-mass energies of 10 GeV τ decays can be separated in the centre-of-mass frame. It is convenient to select events by splitting them into hemispheres along the plane orthogonal to the *thrust*[24] [54] axis in order to divide the event into two distinct and isolated sections. All events are required to have a 1-1 charged track topology - one track in each hemisphere. In order to distinguish between τ and dimuon production the missing energy characteristic of τ decays due to the presence of neutrinos is exploited.

To enable high-purity particle identification of selected tracks in events, these tracks must be within the geometric acceptance of both the DIRC and the EMC ($-0.76 < \cos\theta < 0.80$). This allows the use of different particle selectors and permits the results to be investigated since selectors commonly rely upon hits within the EMC and DIRC.

The histograms use colour coding, as in Figure 4.3 ($\Upsilon(3S)$) and Figure 4.4 ($\Upsilon(4S)$). $\Upsilon(3S)$ events which subsequently decay through a $\Upsilon(2S)$ meson are classified as $\Upsilon(3S) \rightarrow \gamma\gamma\Upsilon(2S)$

---

[23]Except in the case where there is *hard* initial or final state radiation. Hard typically means that the photon emitted has energy above 100 MeV.

[24]The thrust axis aligns strongly with the direction of τ-lepton decay product and the direction of the individual muon (for dimuon events).

[there is more than one decay channel between the $\Upsilon(3S)$ to the $\Upsilon(2S)$, for example $\Upsilon(3S) \rightarrow \gamma\gamma\Upsilon(2S)$ and $\Upsilon(3S) \rightarrow \gamma\chi_{b2}(2\mathrm{P}) \rightarrow \gamma\gamma\Upsilon(2S))$]. Decays of the $\Upsilon(3S)$ meson that go through either a $\Upsilon(1S)$ or $\Upsilon(2S)$ (or both) are called cascade decays and these decays (see Table 4.3) are intrinsic backgrounds because both the $\Upsilon(1S)$ and $\Upsilon(2S)$ can decay into τ or muon pairs with an increase in the number of photons in the final state.

(a)   (b)
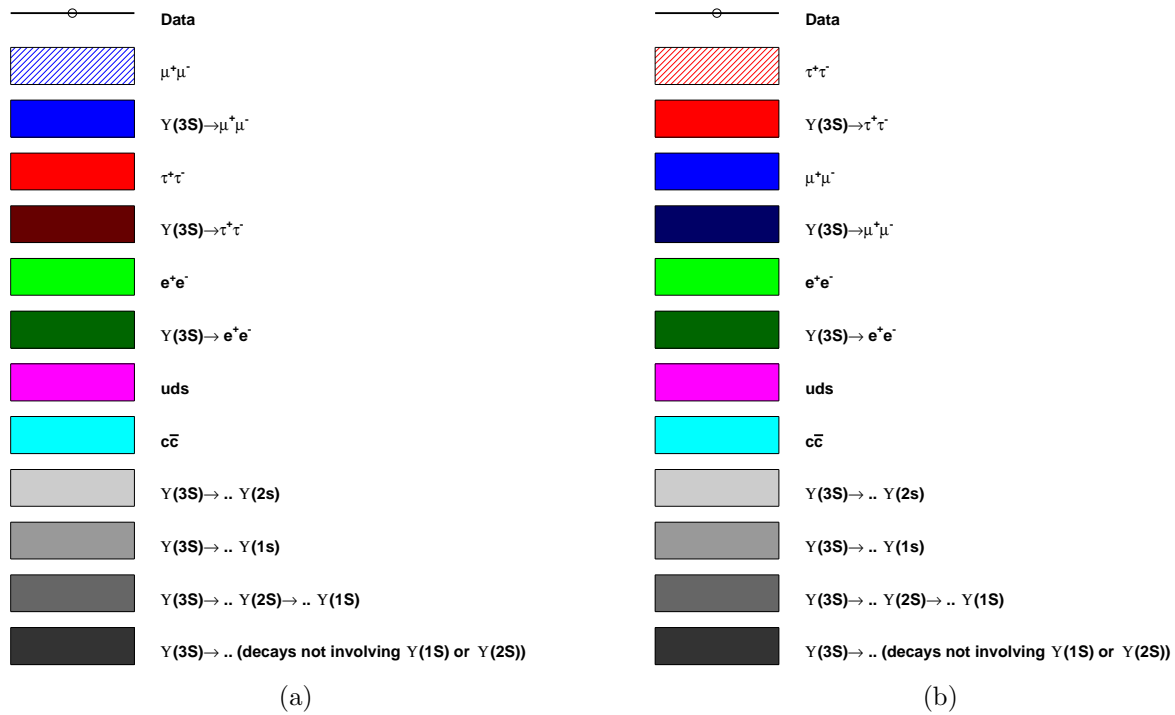
Figure 4.3: Breakdown of Monte Carlo simulated events ($\Upsilon(3S)$).
(a) Colour coding for dimuon selection;
(b) Colour coding for τ-pair selection.

In dimuon selection the energy which must be deposited in the EMC of each track will be greater than 50 MeV and at least one track must have less than 400 MeV deposited in the EMC. Dimuon events are separated from τ events using the variable $[-\ln(\mathrm{M}_{\mathrm{missing}}/\sqrt{s})]$, denoted $-\ln(\mathcal{M}/\sqrt{s})$ (see Figure 4.15 for the $-\ln(\mathcal{M}/\sqrt{s})$ distribution without the cut on missing mass being applied). Missing mass ($\mathcal{M}$) is defined as the invariant mass of the
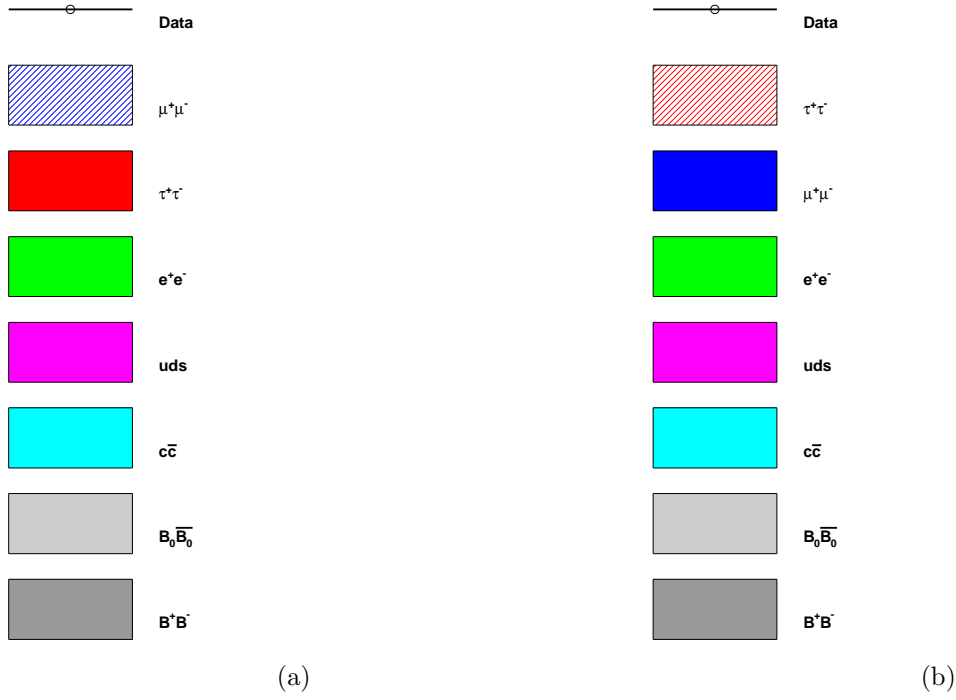
Figure 4.4: Breakdown of Monte Carlo simulated events ($\Upsilon(4S)$).
(a) Colour coding for dimuon selection;
(b) Colour coding for τ-pair selection.

4-vector,

$$p^{\mu}_{\text{total}} - p^{\mu}_{\text{observed}}, \tag{4.10}$$

where p^{μ}_{total} is from the beam parameters and $p^{\mu}_{\text{observed}}$ is the total reconstructed 4-momentum.

(a) Dimuon selection

(b) τ selection

(c)

(d)
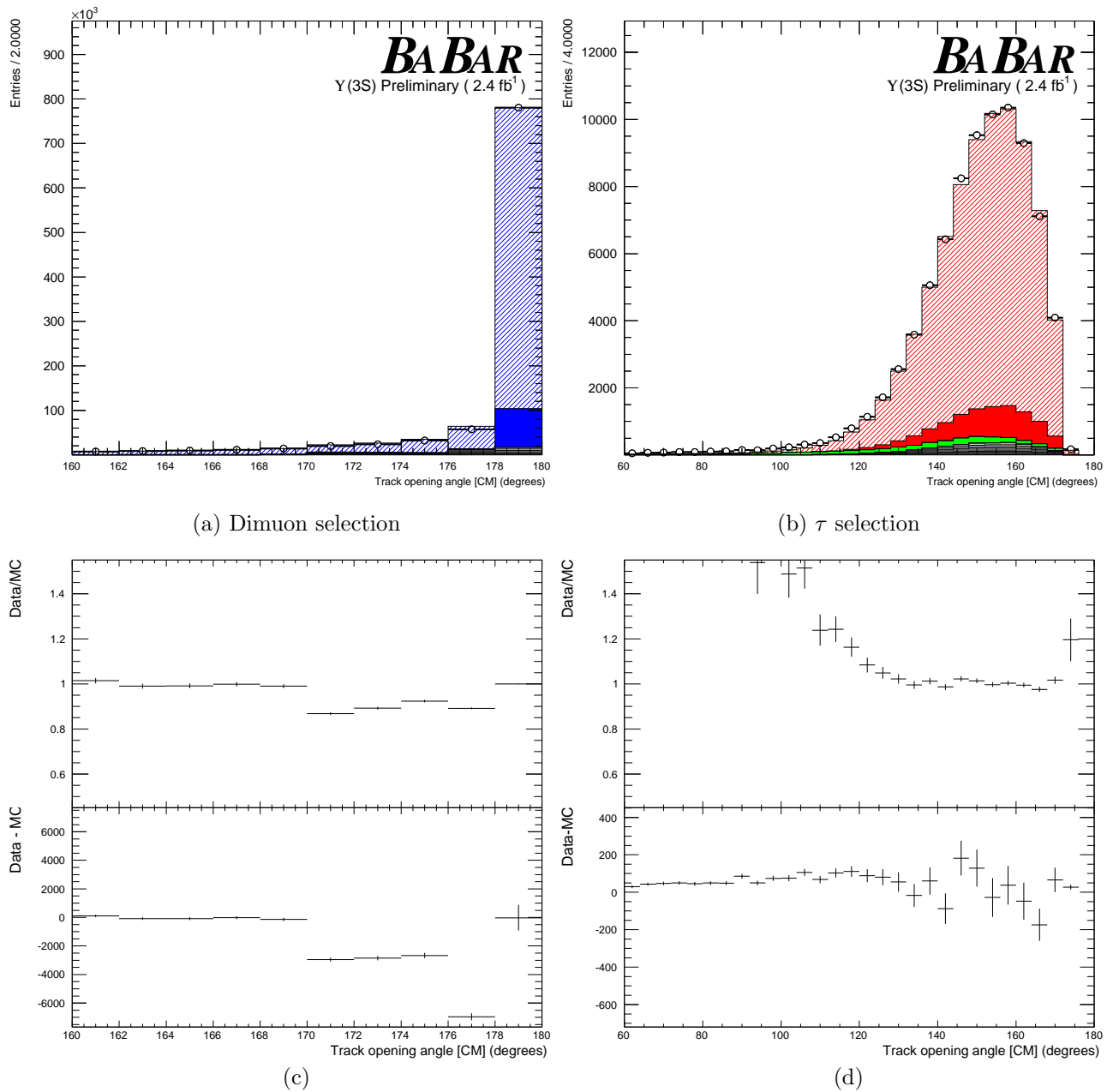
Figure 4.5: Selection plot of track opening angle in the centre-of-mass frame $(\Upsilon(3S))$. The dataset being plotted is `Run 7`. All plots show the Data and Monte Carlo with all selections, but the on one on tracking opening angle. Estimate of the Track Opening Angle in the centre-of-mass Frame:

Figure (a) there is no additional selection applied to track opening angle (dimuons).

Figure (b) the τ selection occurs at $132°$.

Figure (c) the difference between Data and MC histograms and ratio are plotted for (a).

Figure (d) the difference between Data and MC histograms and ratio are plotted for (b).

(a) Dimuon selection

(b) τ selection

(c)

(d)
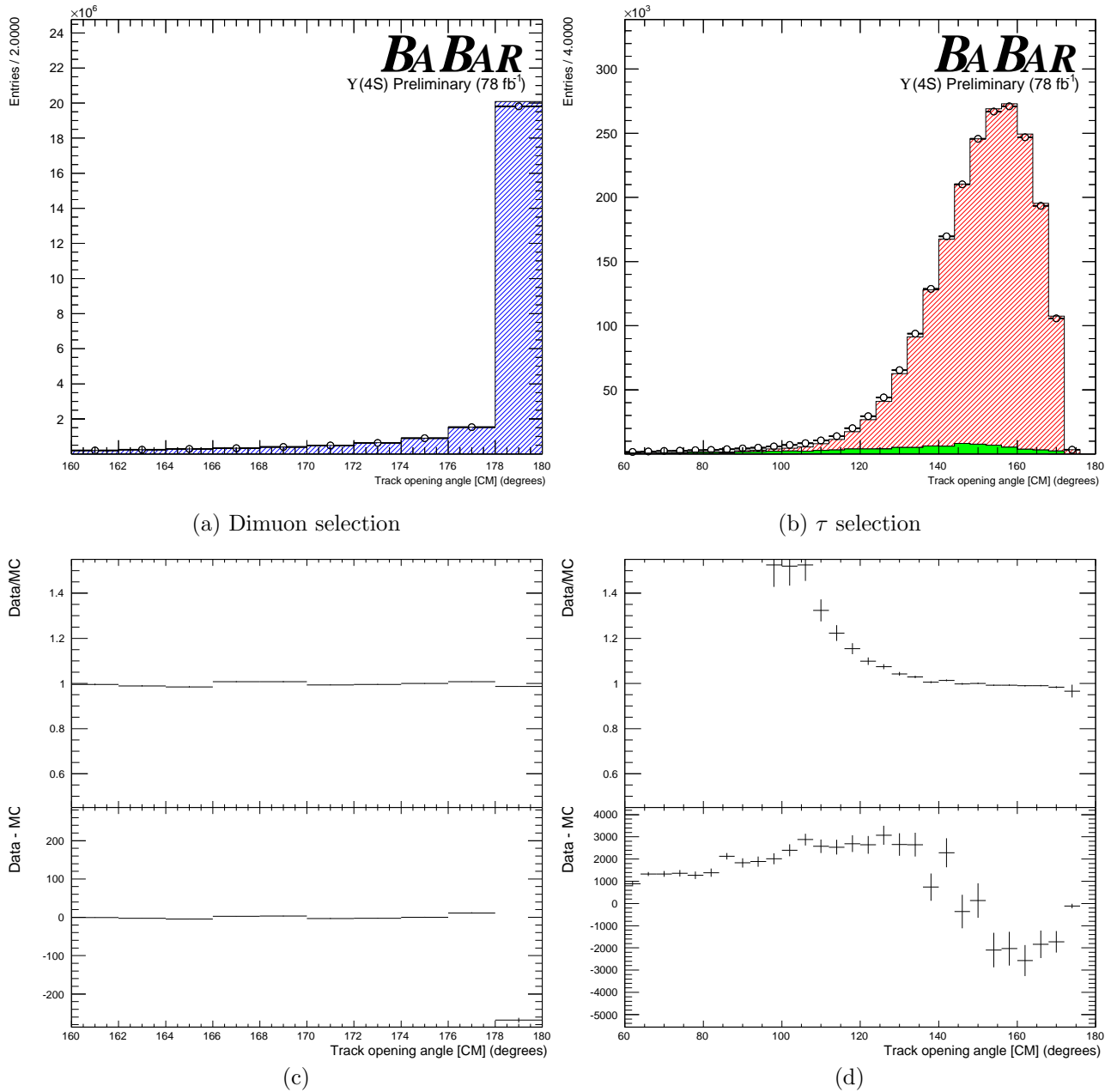
Figure 4.6: Selection plot of track opening angle in the centre-of-mass frame ($\Upsilon(4S)$). The dataset being plotted is Run 6. Estimate of the Track Opening Angle in the centre-of-mass Frame ($\Upsilon(4S)$):

Figure (a) there is no additional selection applied on track opening angle (dimuons).

Figure (b) the τ selection occurs at 132°.

Figure (c) the difference between Data and MC histograms and ratio are plotted for (a).

Figure (d) the difference between Data and MC histograms and ratio are plotted for (b).

(a) Dimuon selection

(b) τ selection

(c)

(d)
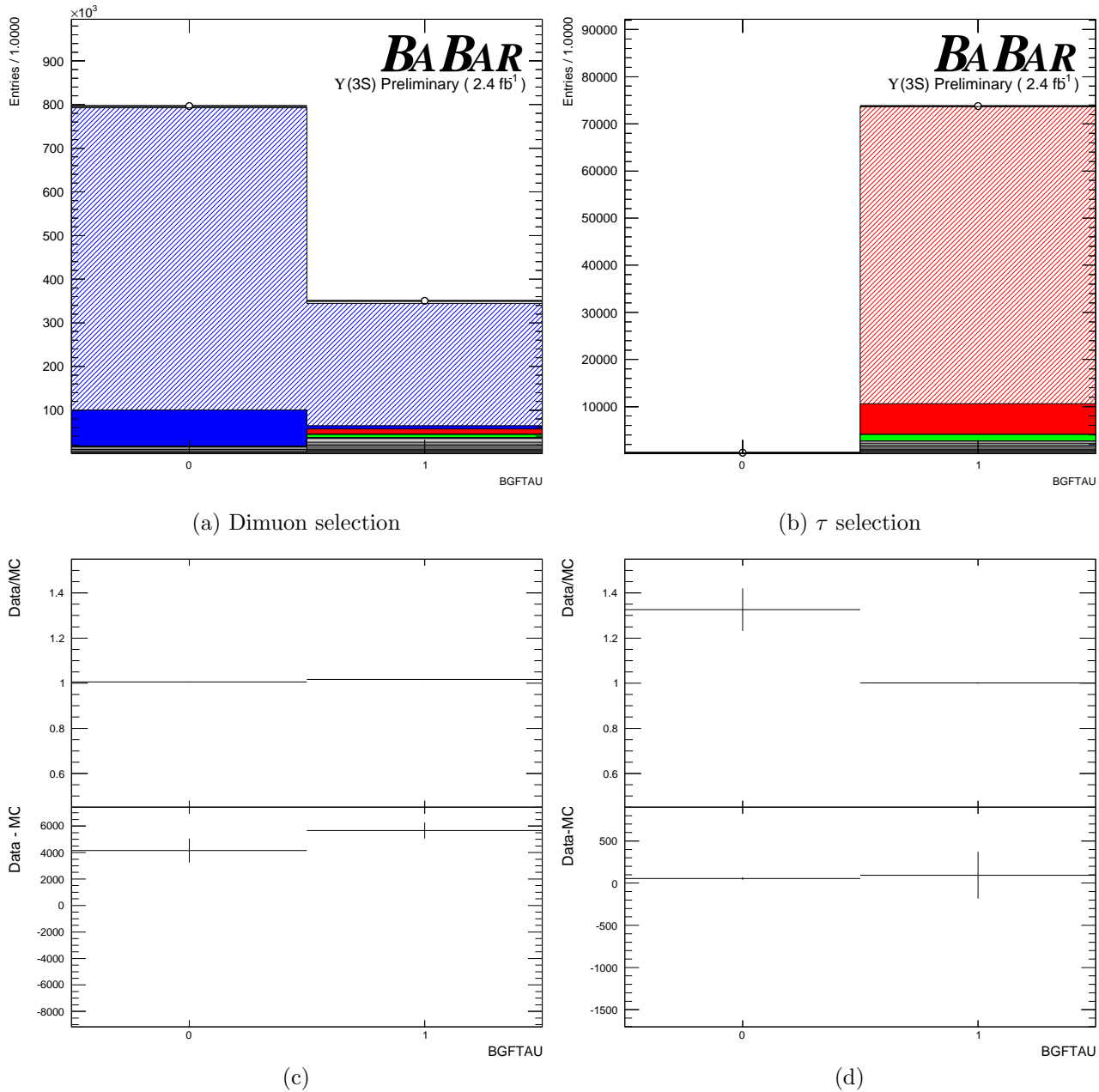
Figure 4.7: <u>Selection plot of τ Background Filter ($\Upsilon(3S)$)</u>. The dataset being plotted is `Run 7`. Estimate of the number of events passing the τ Background Filter.

Figure (a) there is no additional selection applied (dimuons).

Figure (b) the τ selection is equivalent to: (**BGFTau**||**BGFTwoProng**), where || is the logical **OR** operation.

Figure (c) the difference between Data and MC histograms and ratio are plotted for (a).

Figure (d) the difference between Data and MC histograms and ratio are plotted for (b).

(a) Dimuon selection

(b) τ selection

(c)

(d)
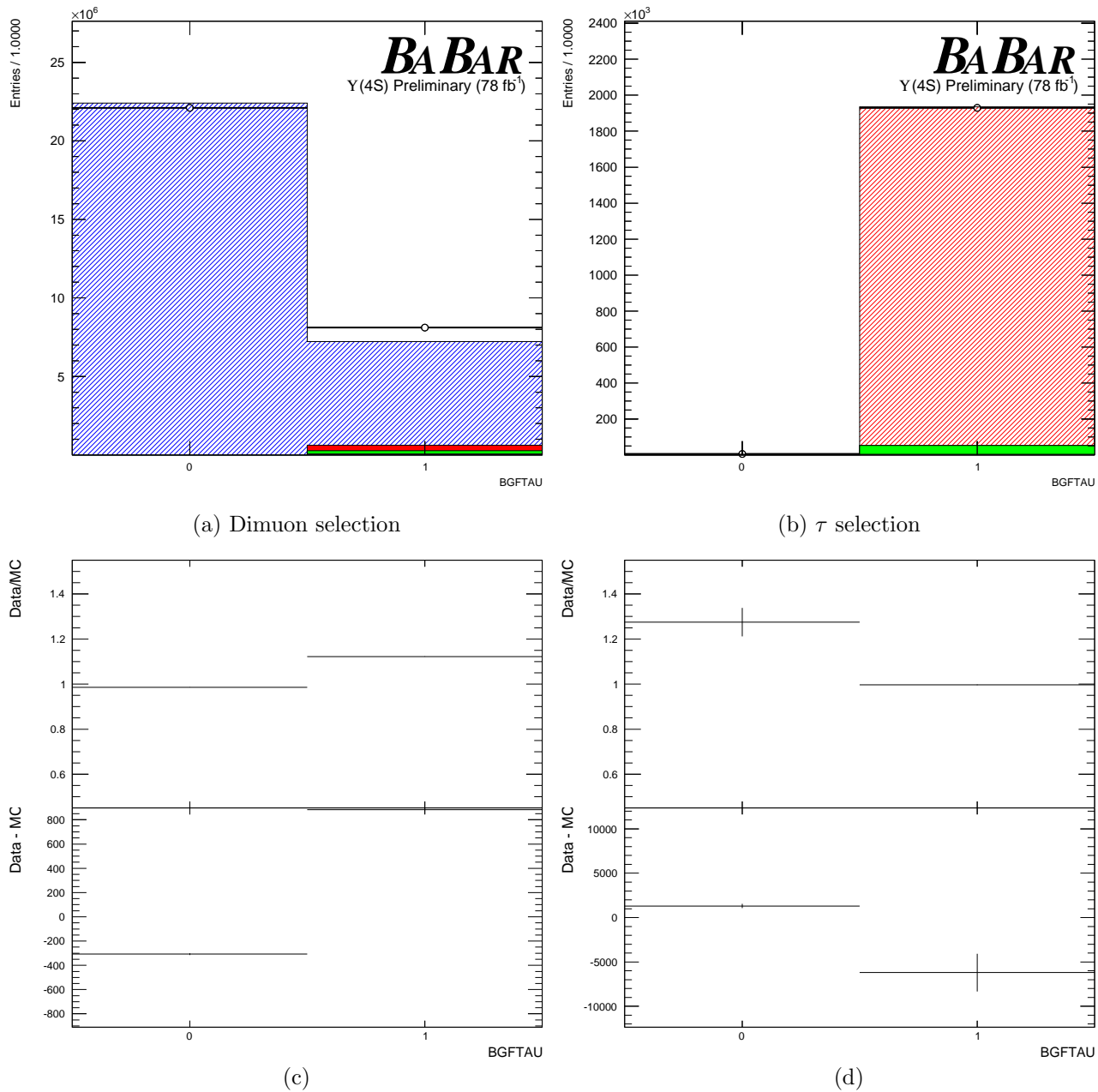
Figure 4.8: Selection plot of τ Background Filter ($\Upsilon(4S)$). Estimate of the number of events passing the τ Background Filter.
Figure (a) there is no additional selection applied (dimuons).
Figure (b) the τ selection is equivalent to: (**BGFTau**||**BGFTwoProng**), where || is the logical **OR** operation.
Figure (c) the difference between Data and MC histograms and ratio for Figure (a).
Figure (d) the difference between Data and MC histograms and ratio for Figure (b).

(a) Dimuon selection

(b) τ selection

(c)

(d)
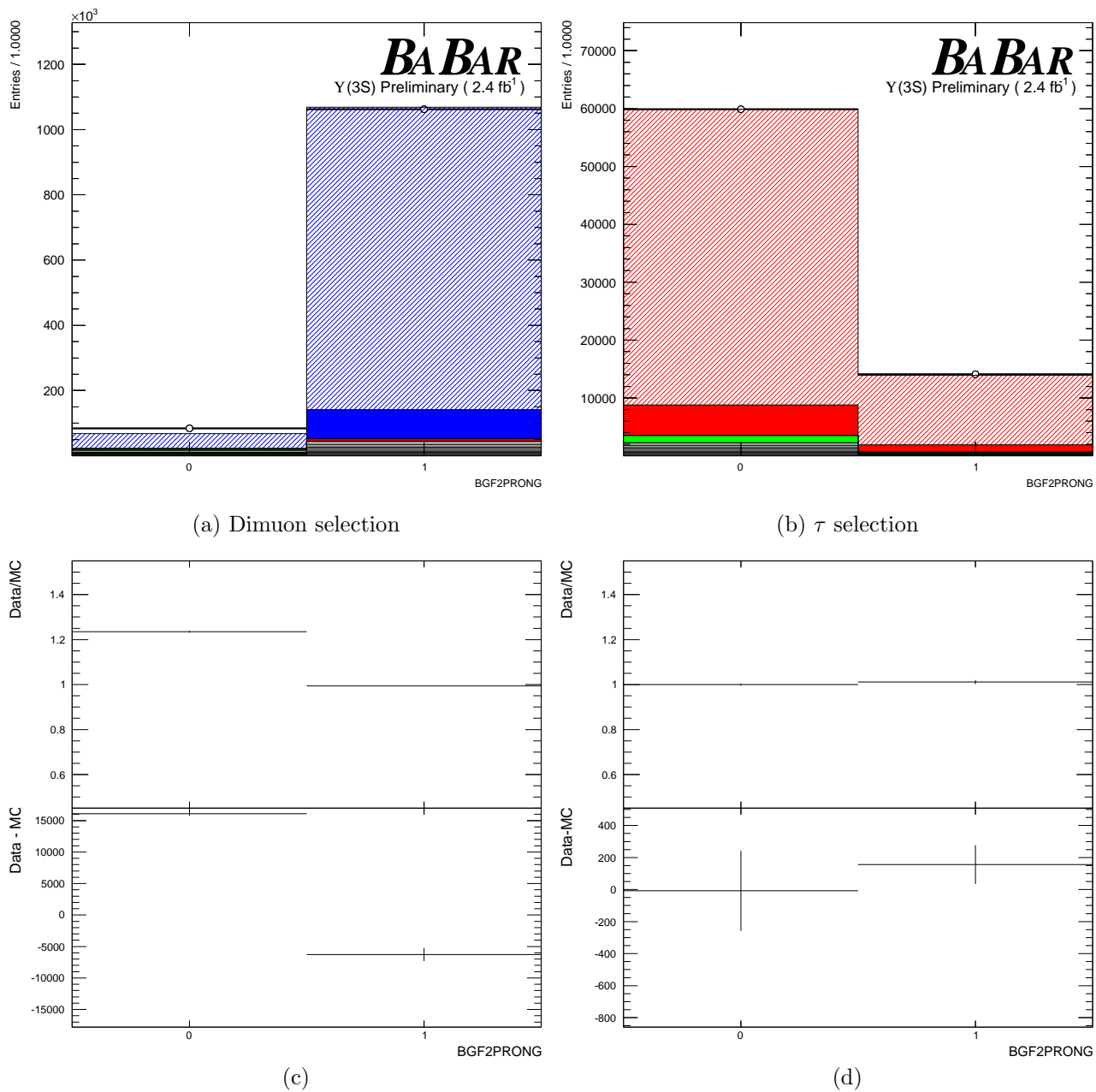
Figure 4.9: Selection plot of Two prong Background Filter ($\Upsilon(3S)$). The dataset being plotted is Run 7. Estimate of the number of events passing the Two Prong Background Filter.

Figure (a) there is no additional selection applied (dimuons).

Figure (b) the τ selection is equivalent to: (**BGFTau**||**BGFTwoProng**), where || is the logical **OR** operation.

Figure (c) the difference between Data and MC histograms and ratio for Figure (a).

Figure (d) the difference between Data and MC histograms and ratio for Figure (b).

(a) Dimuon selection

(b) τ selection

(c)

(d)
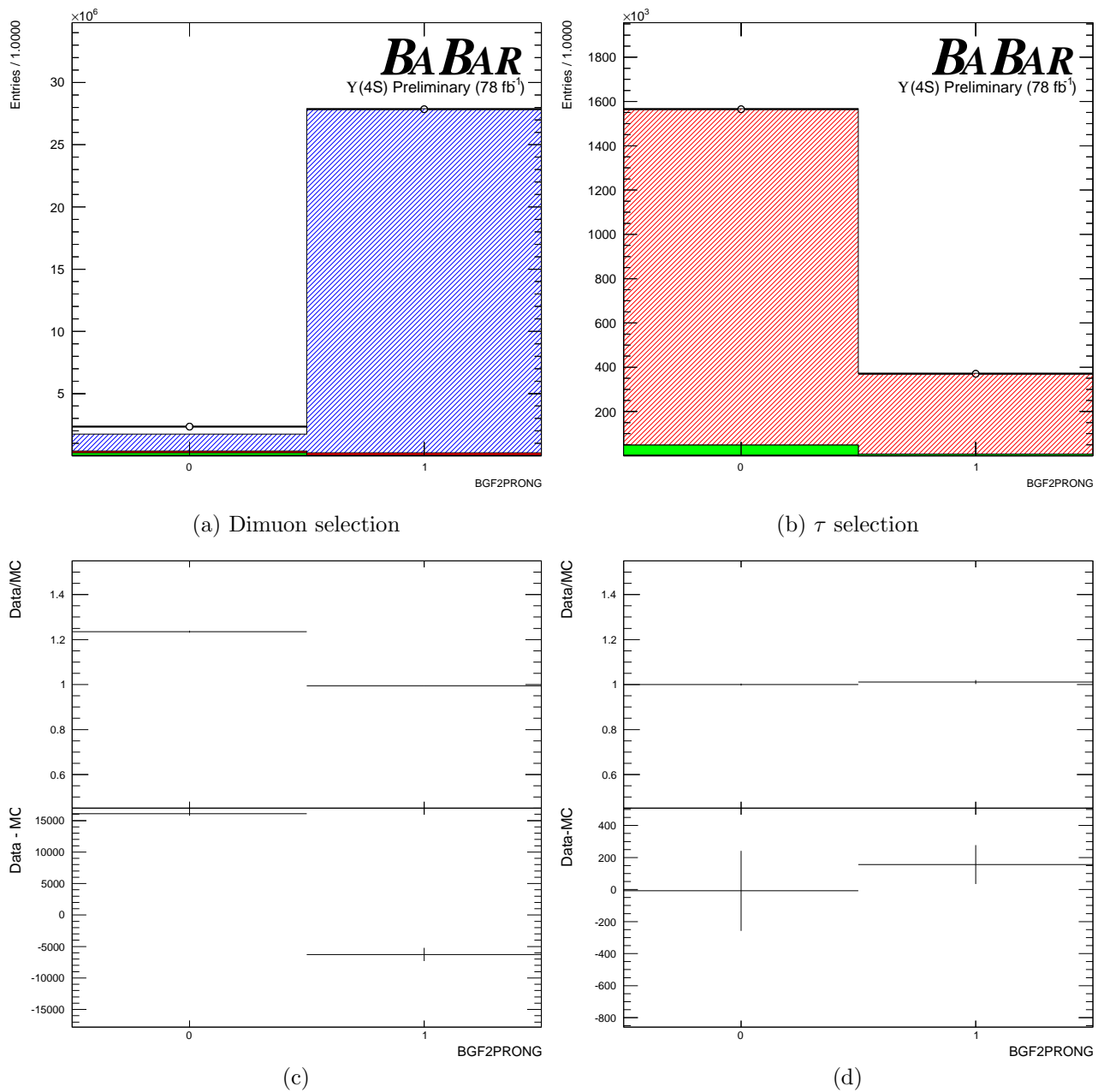
Figure 4.10: Selection plot of Two prong Background Filter ($\Upsilon(4S)$). The dataset being plotted is `Run 6`. Estimate of the number of events passing the Two Prong Background Filter.

Figure (a) there is no additional selection applied (dimuons).

Figure (b) the τ selection is equivalent to: (**BGFTau**||**BGFTwoProng**), where || is the logical **OR** operation.

Figure (c) the difference between Data and MC histograms and ratio for Figure (a).

Figure (d) the difference between Data and MC histograms and ratio for Figure (b).

(a) Dimuon selection

(b) τ selection

(c)

(d)
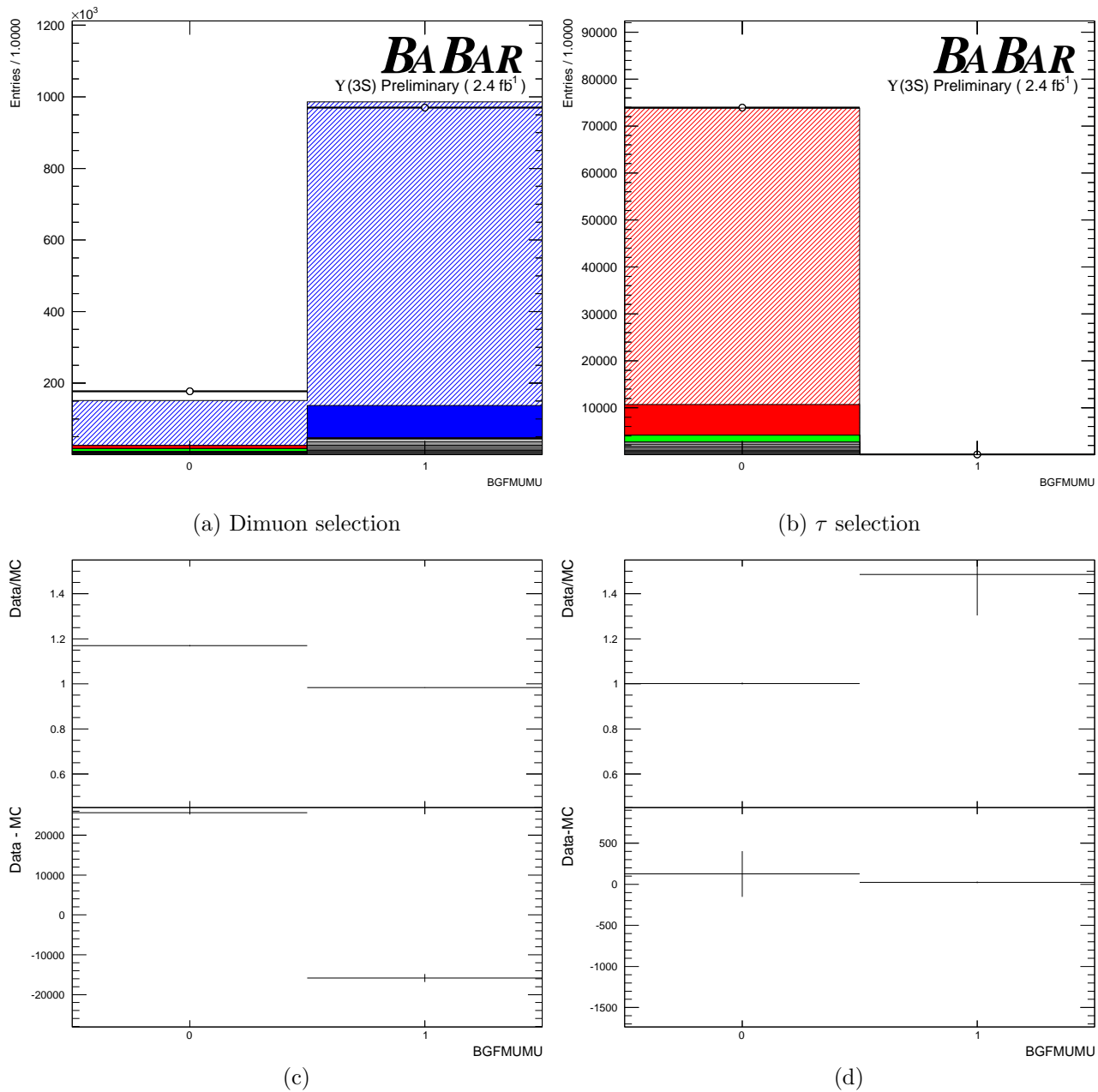
Figure 4.11: Selection plot of Dimuon Background Filter ($\Upsilon(3S)$). The dataset being plotted is Run 7. Estimate of the number of events passing the Dimuon Background Filter (**BGFMuMu**). Variable being plotted is (BGFMuMu).

Figure (a) the selection is equivalent to: **BGFMuMu** > 0 (dimuons).

Figure (b) there is no additional selection applied to the τ.

Figure (c) the difference between Data and MC histograms and ratio for Figure (a).

Figure (d) the difference between Data and MC histograms and ratio for Figure (b).

(a) Dimuon selection

(b) τ selection

(c)

(d)
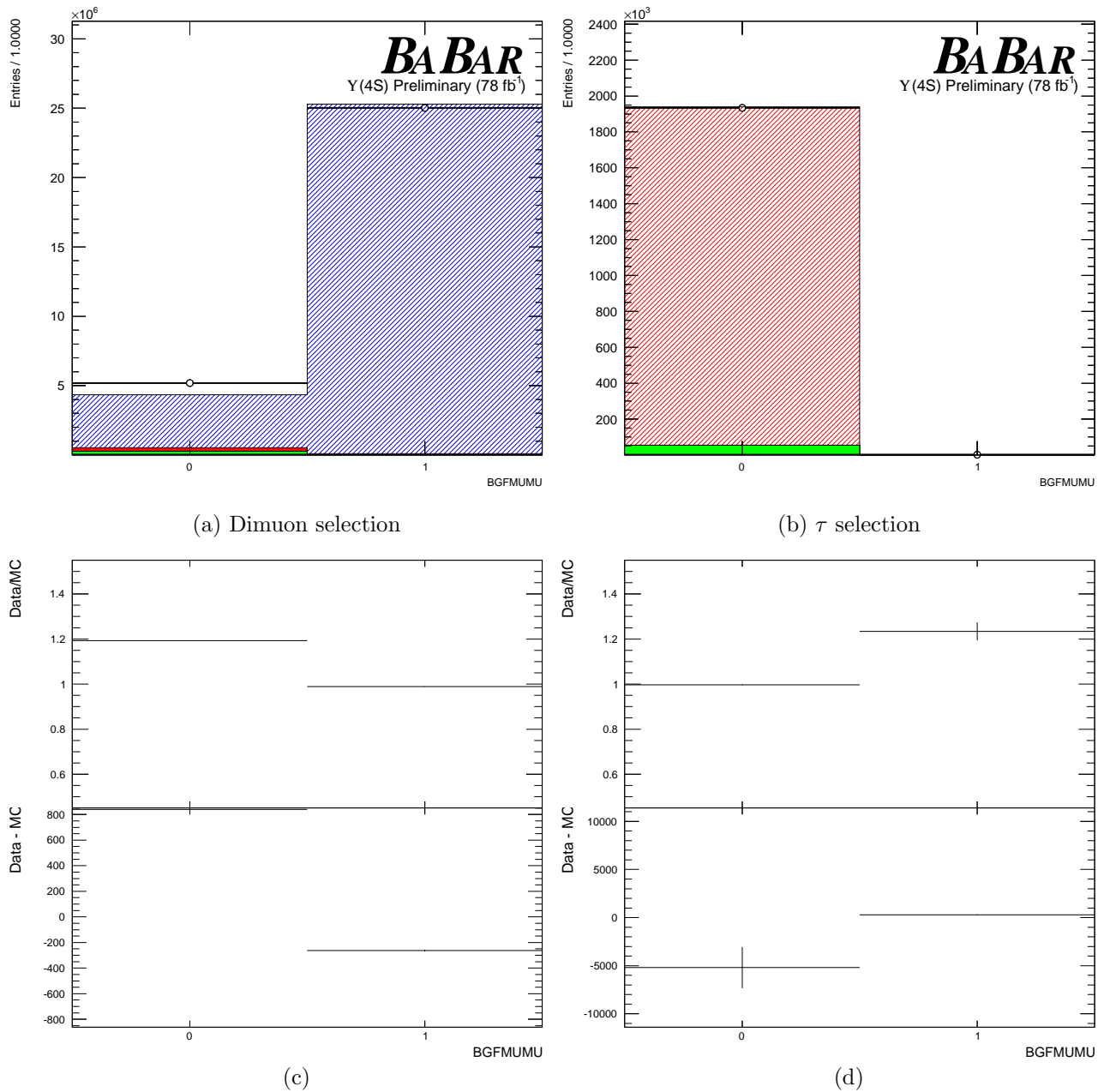
Figure 4.12: Selection plot of Dimuon Background Filter ($\Upsilon(4S)$). The dataset being plotted is Run 6. Estimate of the number of events passing the Dimuon Background Filter (**BGF-MuMu**).

Figure (a) the selection is equivalent to: **BGFMuMu** > 0 (dimuons).

Figure (b) there is no additional selection applied to the τ.

Figure (c) the difference between Data and MC histograms and ratio for Figure (a).

Figure (d) the difference between Data and MC histograms and ratio for Figure (b).

(a) Dimuon selection

(b) τ selection

(c)

(d)
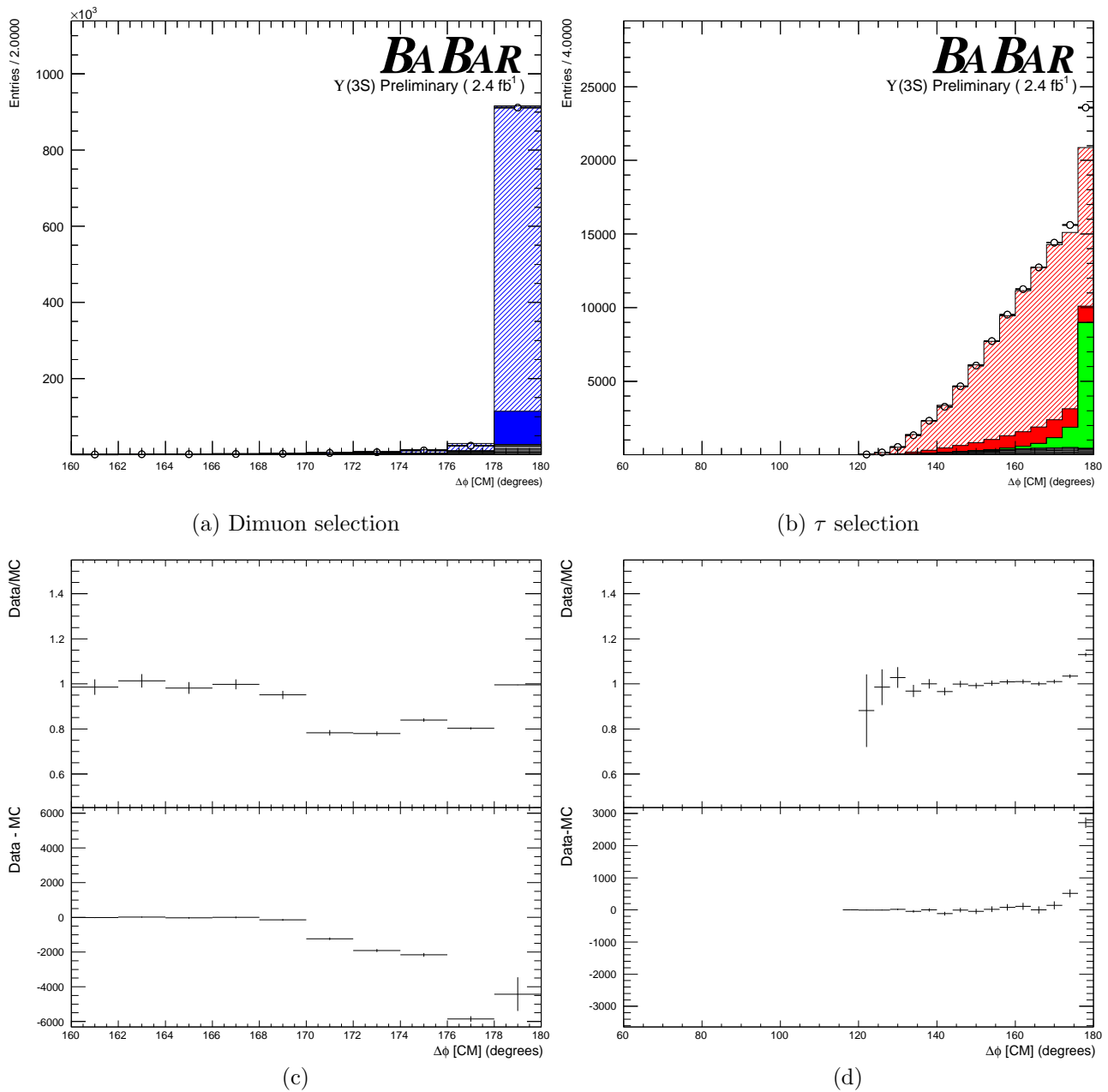
Figure 4.13: <u>Selection plot of</u> $\Delta\phi$ in the centre-of-mass ($\Upsilon(3S)$). The dataset being plotted is `Run 7`. Histogram of $\Delta\phi$ in the centre-of-mass.gure (a) there is no additional selection applied (dimuons).gure (b) the τ selection is $\Delta\phi_{\mathrm{CM}} < 172°$.gure (c) the difference between Data and MC histograms and ratio for Figure (a).gure (d) the difference between Data and MC histograms and ratio for Figure (b).

(a) Dimuon selection

(b) τ selection

(c)

(d)
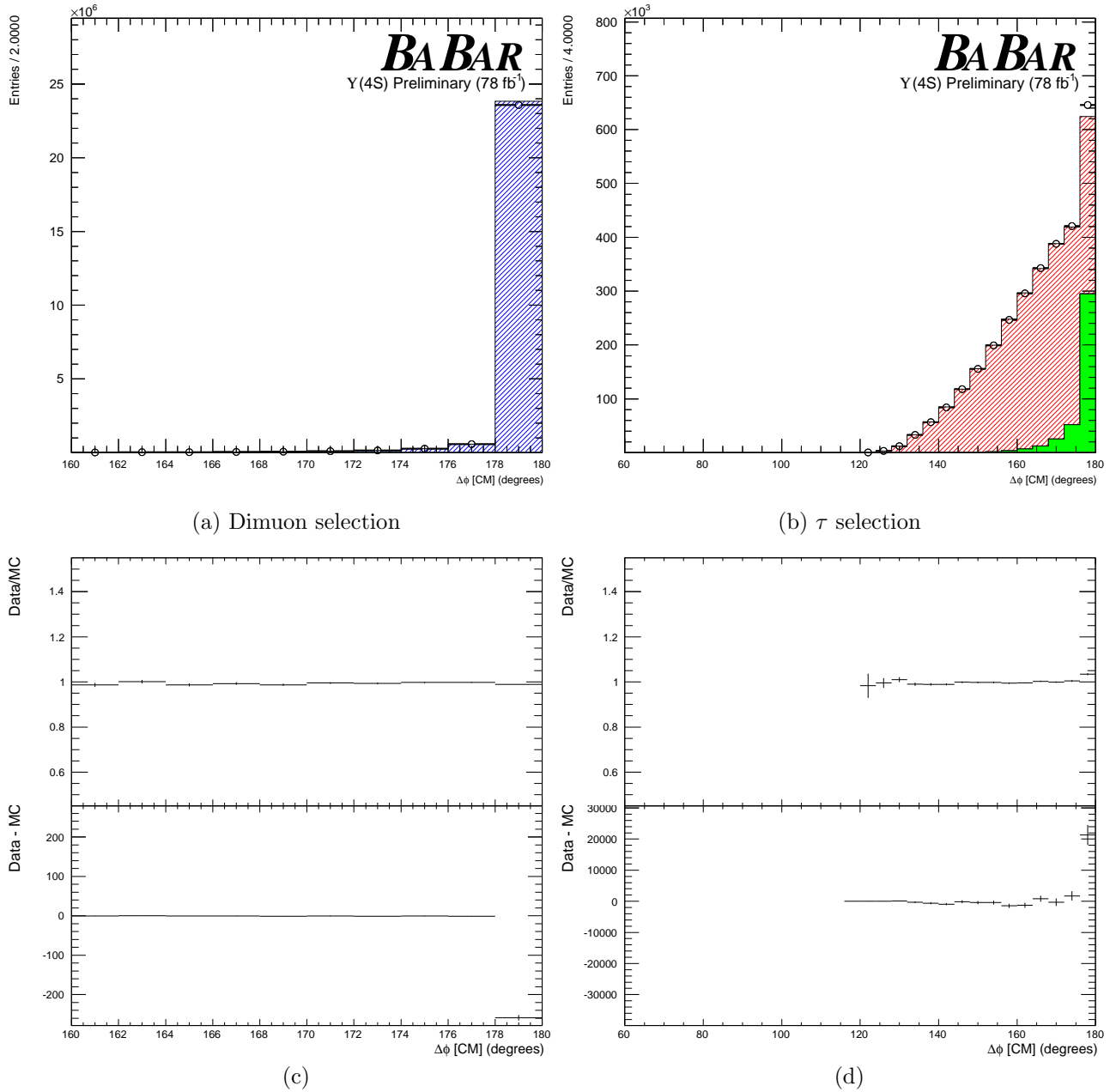
Figure 4.14: Selection plot of $\Delta\phi$ in the centre-of-mass ($\Upsilon(4S)$). The dataset being plotted is Run 6. Histogram of $\Delta\phi$ in the centre-of-mass.

Figure (a) there is no additional selection applied (dimuons).

Figure (b) the τ selection is $\Delta\phi_{\mathrm{CM}} < 172°$.

Figure (c) the difference between Data and MC histograms and ratio for Figure (a).

Figure (d) the difference between Data and MC histograms and ratio for Figure (b).

Imposing particle identification on the daughter particles of τ decays allows for an investigation of the refinements of dimuon weak selection where the *Particle IDentification* (PID) selector muBDTLoose[25] is used to pass one (1-PID) track or both (2-PID) tracks. These are denoted $[\mu\mu^{\text{NO PID}}]$, $[\mu\mu^{\text{1-PID}}]$, and $[\mu\mu^{\text{2-PID}}]$ respectively. Applying additional restrictions to the tracks, the efficiency of selection drops substantially with minimal improvement in background rejection. These selectors were not used in the final measurement.

4.4.2 Weak Dimuon Selection

In general, the energy deposited in the EMC from both tracks must be greater than 50 MeV. This enforces the condition that the tracks entered a crystal, as opposed to passing through a crack, and that the crystal is operational. In addition, the following are also required:

- $-\ln(\not{M}/\sqrt{s}) > 2$ Removes a large number of events which involve missing energy (τ and two photon events); See Figure 4.15 and Figure 4.16.

- Both tracks pass the dimuon background filter. This imposes the following condition on both tracks: $|\mathbf{p}_0^{\text{CM}}| > 4$ GeV and $|\mathbf{p}_1^{\text{CM}}| > 2$ GeV. See Figure 4.11 and Figure 4.12.

- Either track has $\text{E}_{\text{EMC}} < 0.4$ GeV. No PID selection. This removes Bhabha events from the selection.

- Events with two photon clusters that are equivalent to a π^0 are removed (this requirement is only applied to a single hemisphere).

4.4.3 τ Selection

τ selection relies on particle identification selectors - *electron likelihood tight* (see Section A.1); and cuts (or selection requirements) on the opening angle between the two tracks in the centre-of-mass, $\Delta\phi$, the individual tracks's measured momentum, the total estimated event

---

[25]Muon identification relies upon a bagged decision tree (BDT) algorithm that yields greater than 80 % efficiency for selecting muons.

(a) Dimuon selection

(b) τ selection

(c)

(d)
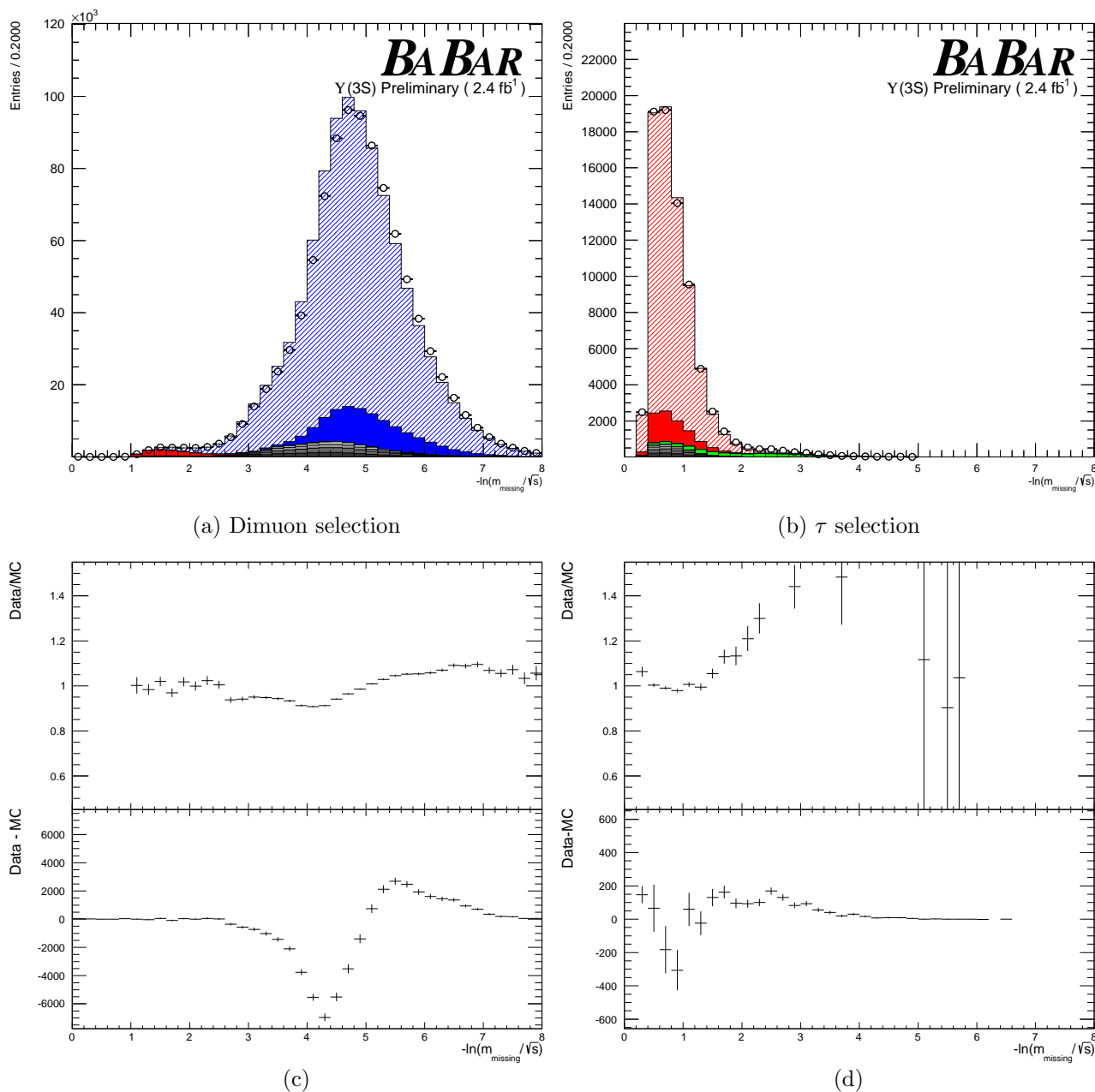
Figure 4.15: Selection plot of Log of the Missing Mass ($\Upsilon(3S)$). Estimate of the missing mass associated with the event. Variable being plotted is: $-\ln(\not{M}/\sqrt{s})$. The shift in the missing mass spectrum for the dimuons corresponds to an estimated 2 MeV difference in the total scale between data events and Monte Carlo events. The estimated mean for the data distribution is 4.841, which corresponds to a missing mass of $81.8\,\mathrm{MeV}/c^2$ while the MC distribution has a mean of 4.7991 corresponding to a missing mass of 85.2 MeV/c^2 (assuming the same total beam energy of $10.3552\,\mathrm{GeV}$). The total beam energy of the QED Monte Carlo events is lower by approximately 4 MeV. The effects of this shift is estimated by the beam energy systematic (which corresponds to a 4 MeV shift in the total beam energy).

Figure (a) the majority of dimuons fall to the right of 2 (events with $-\ln(\not{M}/\sqrt{s}) > 2$ are accepted in the final dimuon selection).

Figure (b) the majority of τ events fall to left of 2 (events with $-\ln(\not{M}/\sqrt{s}) < 2$ are accepted in the final τ selection).

Figure (c) the difference between Data and MC histograms and ratio for Figure (a).

Figure (d) the difference between Data and MC histograms and ratio for Figure (b).

(a) Dimuon selection

(b) τ selection

(c)

(d)
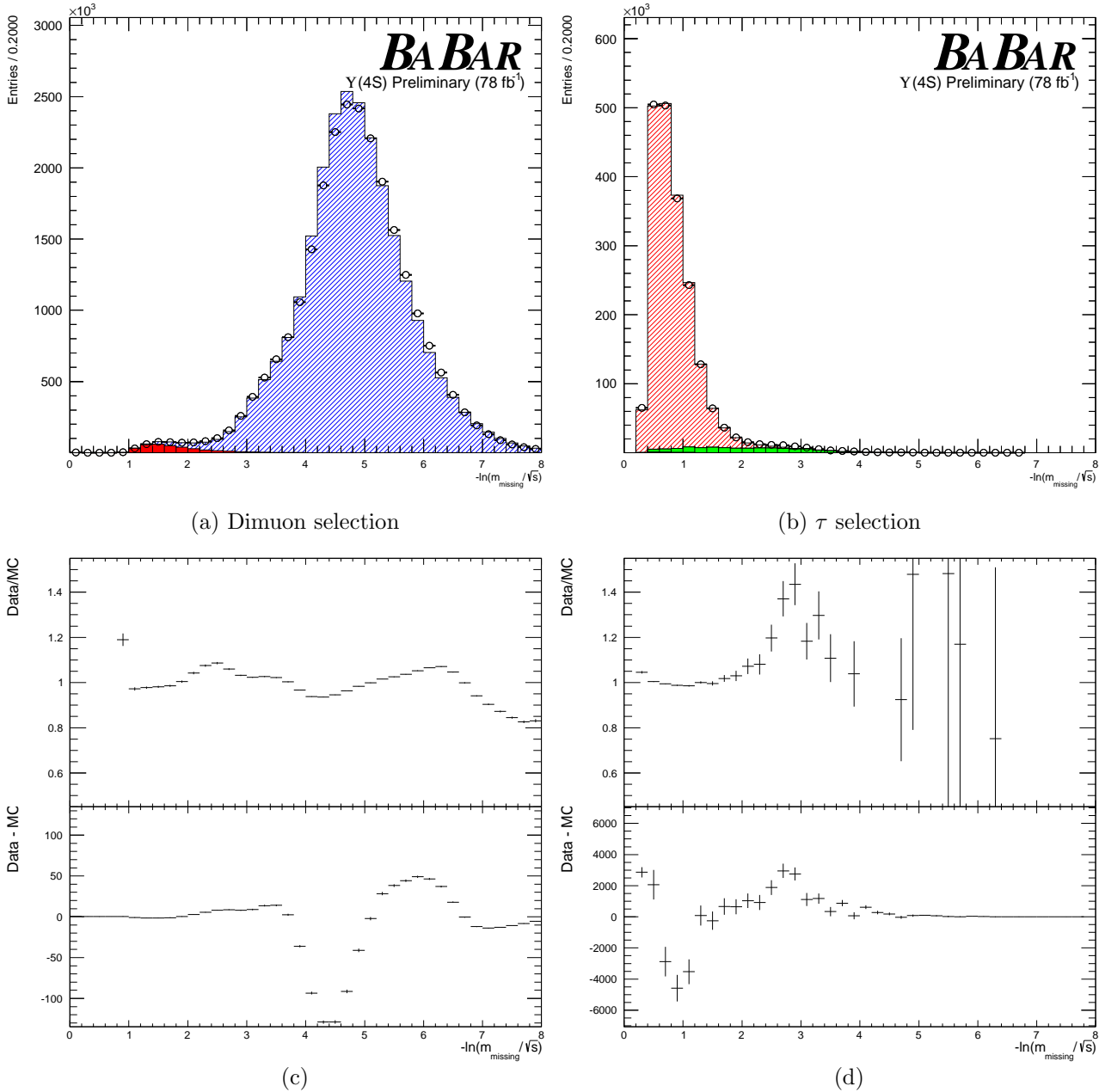
Figure 4.16: <u>Selection plot of Log of the Missing Mass ($\Upsilon(4S)$).</u> Estimate of the missing mass associated with the event. Variable being plotted is: $-\ln(\not M /\sqrt{s})$. The shift in the missing mass spectrum for the dimuons corresponds to an estimated 2 MeV difference in the total scale between data events and Monte Carlo events. The estimated mean for the data distribution is 4.80672, which corresponds to a missing mass of $86.5\,\mathrm{MeV}/c^2$ while the MC distribution has a mean of 4.80044 corresponding to a missing mass of 87.0 MeV/c^2 (assuming the same total beam energy of 10.58 GeV). Further the effects of this shift is estimated by the beam energy systematic (which corresponds to a 4 MeV shift in the total beam energy).

Figure (a) the majority of dimuons fall to the right of 2 (events with $-\ln(\not M /\sqrt{s}) > 2$ are accepted in the final dimuon selection).

Figure (b) the majority of τ events fall to left of 2 (events with $-\ln(\not M /\sqrt{s}) < 2$ are accepted in the final τ selection).

Figure (c) the difference between Data and MC histograms and ratio for Figure (a).

Figure (d) the difference between Data and MC histograms and ratio for Figure (b).

energy, the missing mass, and π^0 veto. $\Delta\phi$ (the difference in the azimuth between the decay products of the two τ leptons) is defined as follows:

$$\Delta\phi = \begin{cases} |\phi_1^{\mathrm{CM}} - \phi_2^{\mathrm{CM}}| & \textbf{if}|\phi_1^{\mathrm{CM}} - \phi_2^{\mathrm{CM}}| < 180° \\ 2\pi - |\phi_1^{\mathrm{CM}} - \phi_2^{\mathrm{CM}}| & \textbf{if}|\phi_1^{\mathrm{CM}} - \phi_2^{\mathrm{CM}}| > 180°. \end{cases} \tag{4.11}$$

- The opening angle between the two tracks in the centre-of-mass (denoted $\Delta\theta > 132°$). This removes two-photon events. See Figure 4.5 and Figure 4.6.

- $\Delta\phi < 172°$ (defined in Equation (4.11)). This removes a large number of Bhabha events. See Figure 4.13 and Figure 4.14.

- Track momentum; both tracks are required to have at least 0.700 GeV/c. This guarantees that events will hit at least the EMC.

- $0.3 < \mathrm{E_{visible}}/\mathrm{E_{initial}} < 0.7$; Removes a large amount of Bhabhas, dimuons, and two-photon events.

- $\mathrm{E_{EMC}}/|\mathbf{p}_{\mathrm{track}}| > 0.5$ (this is not applied in the selection, but is documented due to the nature of the electron selector); this is one of the primary variables used in the electron likelihood tight selector (see Section A.1 for a discussion on the electron likelihood selector).

- $-\ln(\not{M}/\sqrt{s}) > 2$; removes a large number of events which do not have missing energy (Bhabhas, dimuons, hadrons). See Figure 4.15 and Figure 4.16.

- Events with two photon clusters that are equivalent to a π^0 and found in the electron's hemisphere are rejected.

where $\mathrm{E_{initial}} = \mathrm{E_{LER}} + \mathrm{E_{HER}}$, $\mathrm{E_{visible}}$ is the total observed energy of the event. In order to guarantee that the tracks reach the DIRC and EMC the momentum of the tracks must be larger than 0.7 GeV/c. Since τ decays involve neutrinos, the variable $\mathrm{E_{visible}}/\mathrm{E_{initial}}$

must be between 0.3 and 0.7. $\Delta\phi$ must be less than 172° in order to remove Bhabha and dimuon contamination (which are primarily back-to-back and thus have $\Delta\phi \approx 180$º). To remove hadronic and two photon backgrounds (see Figure 4.2 for the two-photon Feynman diagram) the opening angle in the centre-of-mass must be greater than 132°. The distribution of selected events for the track opening angle is shown in Figure 4.5.

Alternate τ selections were also investigated and included $[\mu\mu]$, $[e\pi]$ and $[\mu\pi]$. For $[\mu\mu]$ and $[\mu\pi]$ events $\mathbf{p}_{\mathrm{missing}}^{\perp}$ must be greater than 1.6 GeV/c in the centre-of-mass (this cut removes two photon events). To remove radiative Bhabha events (see Figure 4.1) in $[e\pi]$ the energy deposited in the calorimeter by the track identified as a pion must be $\mathrm{E}_{\mathrm{EMC}}/|\mathbf{p}| < 0.8$. All of these selections had significantly lower selection efficiency and higher background contamination, and thus were rejected in favour of $[e\not{e}]$.

4.4.4 π^0 Rejection

The veto on π^0 is the same in both dimuon selection and τ selection. It is roughly equivalent to the *BABAR* selector known as `pi0VeryLoose`. The candidate π^0 is formed from two isolated EMC clusters or hits that are consistent with photons. The π^0 candidate is required to have a mass within the range of 90-165 MeV/c^2 and have a helicity[26] in the range of (-0.95,0.95).

4.5   Breakdown of Backgrounds

Using Monte Carlo simulated events, the background rates are shown in Table 4.6 and 4.7. The MC events were normalized to the combined `low` and `high` unblind integrated luminosity.

---

[26]The cosine of the angle between the direction of the π^0 candidate and the angle of the photon in the rest frame of the π^0.

Background Source	$[\mu\mu^{\text{NO PID}}]$ Number of Events
Hadronic Background (uds)	143.5 ± 1.5
Hadronic Background ($c\bar{c}$)	< 1
Bhabhas	103.1 ± 4.2
τ Contamination	2942 ± 11
Two-photon	< 1
$\Upsilon(3S)$ Cascades	$(1.050 \pm 0.0013) \times 10^5$

Table 4.6: Monte Carlo projections of dimuon backgrounds. The estimated number is based upon luminosity scaling to the unblind period, roughly 2.408 fb^{-1} of data. Entries with 0 correspond to the case where no Monte Carlo simulated events passed selection. Entries with < 1 correspond to the cases where the estimated number of events that would pass selection was non-zero but less than 1.

Background Source	τ ($[e\not{e}]$) Number of Events
Hadronic Background (uds)	2.00 ± 0.18
Hadronic Background ($c\bar{c}$)	60.67 ± 0.87
Bhabhas	1452 ± 16
Dimuon Contamination	2.11 ± 0.27
Two-photon	< 1
$\Upsilon(3S)$ Cascades	887 ± 43

Table 4.7: Monte Carlo projections of τ backgrounds. The estimated number is based upon luminosity scaling to the unblind period, roughly 2.402 fb^{-1} of data. Entries with 0 correspond to the case where no Monte Carlo simulated events passed selection. Entries with < 1 correspond to the cases where the estimated number of events that would pass selection was non-zero but less than 1.

Chapter 5

Analysis Tools and Software

5.1   N-tuple Production

BaBar code is built from objects[1] called modules. Each module uses a collection of *inter-nal*, *measured*, and/or *constructed* data and data-types to perform a few well-defined tasks. Modules are designed to serve several purposes which include the following: to manage histograms, to load detector conditions, to read the data from the database, to reconstruct particles, to perform particle identifications, to obtain Monte Carlo simulation information (also known as *truth*), and to perform user analysis. In addition, there are special-purpose modules such as the following: input modules and output modules to control the input and output of data and filter modules to control subsequent data processing. Whenever there is an analysis task to be done, a module is created to do that task.

The modules are strung together along an ordered analysis path. Running an analysis job creates (or *instantiates*) an 'object' called the *Framework*. The Framework passes data from module to module until it reaches the last module of the analysis path. Each module uses the prior module's output data to perform its own task.

---

[1]This is synonymous with the idea of *objects* as defined within various programming languages.

$\mathbf{p}_{\text{low}}$ (GeV/c)	$\mathbf{p}_{\text{high}}$ (GeV/c)	θ_{low}	θ_{high}	ϕ_{low}	ϕ_{high}	$\varepsilon(x)$	$\sigma_{\varepsilon(x)}$	$\mathbf{N}_{\text{passed}}$	$\mathbf{N}_{\text{prior}}$
0.000000	0.500000	0.00	17.00	-180.00	-120.00	0.000000	0.000000	0	0
0.000000	0.500000	0.00	17.00	-120.00	-60.00	0.000000	0.000000	0	0
0.000000	0.500000	0.00	17.00	-60.00	0.00	0.000000	0.000000	0	0
0.000000	0.500000	0.00	17.00	0.00	60.00	0.000000	0.000000	0	0
0.000000	0.500000	0.00	17.00	60.00	120.00	0.000000	0.000000	0	0
0.000000	0.500000	0.00	17.00	120.00	180.00	0.000000	0.000000	0	0
0.500000	0.700000	0.00	17.00	-180.00	-120.00	0.000000	0.000000	0	0
...									
0.900000	1.100000	25.00	33.00	-180.00	-120.00	0.822695	0.022736	232	282
0.900000	1.100000	25.00	33.00	-120.00	-60.00	0.754777	0.024217	237	314
0.900000	1.100000	25.00	33.00	-60.00	0.00	0.655518	0.027364	196	299
0.900000	1.100000	25.00	33.00	0.00	60.00	0.895833	0.018113	258	288
0.900000	1.100000	25.00	33.00	60.00	120.00	0.736527	0.024037	246	334
0.900000	1.100000	25.00	33.00	120.00	180.00	0.683673	0.027013	201	294

Table 5.1: PIDTable layout. Columns **1** and **2** are the momentum interval, $[p_1, p_2)$. Columns **3** and **4** are θ intervals, $[\theta_3, \theta_4)$. Columns **5** and **6** are ϕ intervals, $[\phi_5, \phi_6)$. Columns **7** and **8** are the efficiency of the selector and its associated error, $\varepsilon_7 \pm \sigma_8$. Column **9** is the number of control sample tracks passing the selector, N_9^{passed}. Column **10** is the original number of control sample tracks (prior to the selector), N_{10}^{prior}.

5.2   TauMiniUser

'User' n-tuples are established through the analysis module TauMiniUser. 'TauMiniUser' provides a selection of events consistent with Bhabhas events, dimuons, τ pairs, and low multiplicity hadronic events.

5.3   Particle Identification Tables

Particle Identification (PID) tables are used to correct the estimated selection *efficiency* for different particle types as a function of momentum, θ, and ϕ. Similar to a spreadsheet, each table row corresponds to a particular region of momentum space (see Table 5.1). The grouping of each region of momentum space is commonly referred to as a *bin* (analogous to a histogram bin).

There are 19 bins with respect to momentum (most are roughly 0.2 GeV/c in width). There are 16 bins in θ (the intervals are about $8-12°$), and 6 bins in ϕ, where each interval is 60°.

$$\mathrm{p} \in \{0.0, 0.5, 0.7, 0.9, 1.1, 1.3, 1.5, 1.7, 1.9, 2.1, 2.3, 2.5, 2.7, 2.9, 3.1, 3.3, 3.5, 4.5, 5.0, 99.0\};$$

$$\theta_{\mathrm{low}} \in \{0, 17, 25, 33, 41, 49, 57, 68.6, 80.2, 91.8, 103.4, 115, 123, 131, 139, 147, 155\};$$

$$\phi \in \{-180, -120, -60, 0, 60, 120, 180\};$$

The tables are organized so that they loop over θ only once. This means that they have to loop over momentum and ϕ multiple times. There are very few ϕ bins because the *BABAR* detector was nearly symmetric in ϕ, so that efficiency usually does not vary with ϕ. When the efficiency is observed to vary with ϕ it is usually an indication something is wrong. For example, RPC problems in the IFR (during `Run 5`) caused the efficiency to be non-symmetric on ϕ and this can lead to a ϕ-dependent muon efficiency.

The efficiency of a selector, denoted x, is the fraction of true x that passes the selector. Thus,

$$\varepsilon^{\mathrm{PID}}(x) = \frac{\mathbf{N}^{\mathrm{pass}}(x)}{\mathbf{N}^{\mathrm{true}}(x)} \tag{5.1}$$

control samples are used to measure the efficiency of a PID selector where $\mathbf{N}^{\mathrm{true}}(x)$ is known. For example, Figure 5.1 shows the estimated data selection efficiency for determining if a track is an electron (using the a control sample of Bhabha events). The *BABAR* Particle Identification group uses the following types of control samples to measure PID selector efficiencies:

1. Data - samples of some decay that has (x) as a decay product and can be selected fairly easily without requiring the use of the PID selector;

2. Monte Carlo Control Samples - Using simulated events as *pseudo-data*; and

3. Monte Carlo Truth Samples - Using simulated events with the Monte Carlo truth

information.

The results for each type of sample are stored in different PID tables. The label of each PID table refers to the information it contains. For example, the associated PID Table for muon neural net selector (with a high selection efficiency selection, designated very loose), is stored in the following directory structure,

$$\texttt{run6/muons+/mu.mumug2.NN.VeryLoose.} \tag{5.2}$$

The name and directory structure provides the following information: run number[2], particle with charge[3], measurement of muon efficiency[4], control sample[5], and the selector[6].

5.3.1 Efficiency of particle selectors

The PID tables are used to determine the *true* number of particles (x) in a sample of particles that have passed a selector for that particle (x):

$$\mathrm{N}^{\mathrm{true}}(x) = \mathrm{N}^{\mathrm{pass}}(x)/\varepsilon(x) \tag{5.3}$$

5.3.2 Data/MC corrections for studies using PID selectors

PID tables are also used to correct for Data/MC differences in the PID selectors. The best way to explain the use of these corrections is with the example of reconstructing the decay $D^0 \rightarrow K^+\pi^-$. Reconstruction for kaons (K^+), would require a sample of charged tracks that pass a kaon selector. For pions (π^-), reconstruction would utilize a sample of charged tracks which pass a pion selector. Additional selection criteria are used to reconstruct the D^0. The sample is tested using Monte Carlo, measured for overall efficiency $\varepsilon(D^0)_{\mathrm{MC}}$ (where all the

---

[2]`Run 6.`
[3]μ^+
[4]μ
[5]`mumug2` or $e^+e^- \rightarrow \mu^+\mu^-\gamma$
[6]`NN.VeryLoose`, which is a neural net selector with a high selection efficiency.

terms within the square brackets are MC quantities) as follows:

$$\varepsilon(D^0)_{\text{MC}} = \left[\varepsilon(K^+)\varepsilon(\pi^-)\varepsilon(\text{other})\right]_{\text{MC}} \tag{5.4}$$

A final selection can be applied to the data. In the data sample, the overall efficiency (where all the terms within the square brackets are data associated quantities) is:

$$\varepsilon(D^0)_{\text{Data}} = \left[\varepsilon(K^+)\varepsilon(\pi^-)\varepsilon(\text{other})\right]_{\text{Data}} \tag{5.5}$$

Because $\varepsilon(D^0)_{\text{Data}}$ is unknown and only $\varepsilon(D^0)_{\text{MC}}$ is available. The term $\varepsilon(\text{other})$ can be considered to be the same in data and MC (at least initially). Therefore if there is any difference in $\varepsilon(D^0)$ in data and MC, it must be from the PID selectors,

$$\varepsilon(D^0)_{\text{Data}} = \varepsilon(D^0)_{\text{MC}} \frac{\varepsilon(K^+)_{\text{Data}}}{\varepsilon(K^+)_{\text{MC}}} \frac{\varepsilon(\pi^-)_{\text{Data}}}{\varepsilon(\pi^-)_{\text{MC}}} \tag{5.6}$$

The ratio $[\varepsilon(x)_{\text{Data}}/\varepsilon(x)_{\text{MC}}]$ is called the (x)-PID weight. This ratio is used to correct for Data/MC differences in PID selectors. The *BABAR* PID group supports three different methods to correct for Data/MC differences: PID weighting, PID tweaking, and PID killing.

This analysis used PID weighting done at the event level. Starting with a single unique event, PID weighting proceeds as follows:

1. Read in all the needed PID Tables (there can be more than one PID Table used in the analysis and each PID Table has to have values calculated for its various control samples);

2. Obtain a collection of tracks and the associated reconstructed values (charge, momentum, angles, Monte Carlo event truth);

3. Use the PID Tables as a lookup to determine $\varepsilon(e^-)$ or $\varepsilon(e^+)$ for both data and Monte Carlo events;

4. Check which tracks pass the appropriate PID selector;

5. If the negative track was identified as an electron and the positive charged track was identified as not an electron. Then generate the appropriate PID weight for the overall event, $[\varepsilon(e^-)_{\text{Data}}/\varepsilon(e^-)_{\text{MC}}] \times [1 - \varepsilon(e^+)_{\text{Data}}/(1 - \varepsilon(e^+)_{\text{MC}})]$;

6. Events with PID weights that are outside the range $[0.5, 2]$, are set to 1.0 (because large discrepancies in the Data/MC agreement should not be re-weighted, but investigated and understood more completely).

5.4 Boost Simulation and Analysis Code

Using a simple *n-tuple* interface, a proxy is used to handle queries (enabling non-destructive modification at the single event level) with respect to all parameters. Changes to centre-of-mass or lab frame reconstructed values are propagated to other parameters which derive from the modified parameter. This allows for modifications at runtime to be automatic (and consistent across all Monte Carlo n-tuples).

Various parameters can be altered prior to selection, including (and not limited too) the estimated track momentum (see Figure 5.7), the measured track angle (see Figure 5.8) and the initial beam energy (see Figure 5.6). After modifying the paramters, the analysis software updates all parameters which are dependent on the perturbed value. The effects of altering these parameters changes the estimated selection efficiency and the estimated background contamination. For example, altering the momentum resolution causes slight changes in the Monte Carlo event distributions of:

- track opening angle (see Figure 5.2);

- $-\ln(\cancel{M}/\sqrt{s})$ (see Figure 5.3);

- estimated visible total energy (see Figure 5.4);

- $\Delta\phi$ (see Figure 5.5).
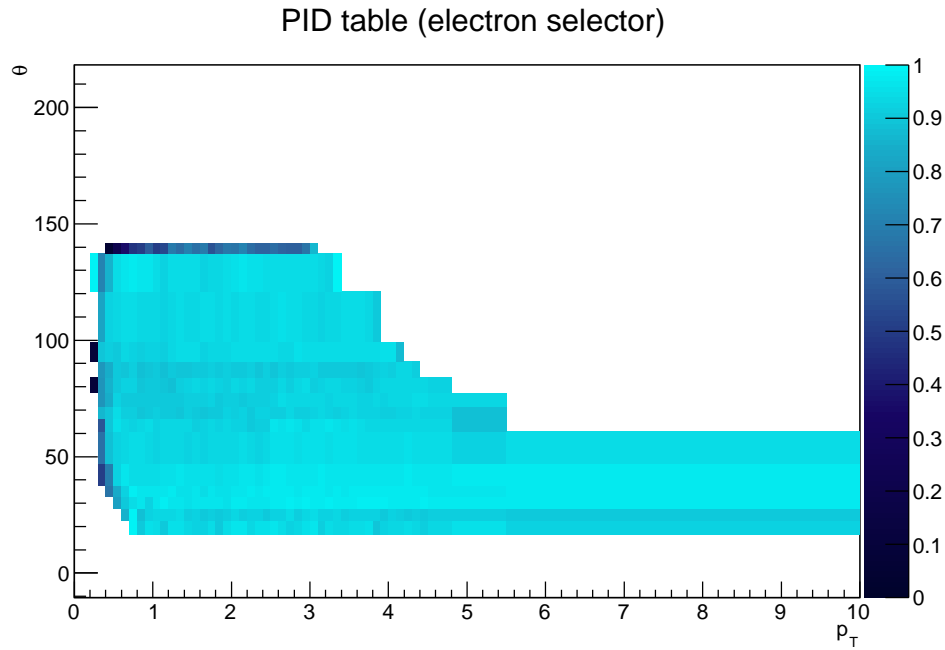
Figure 5.1: The non-zero values of the data effective efficiency for the Run 6 electron selector.

(a) Dimuon selection

(b) τ selection
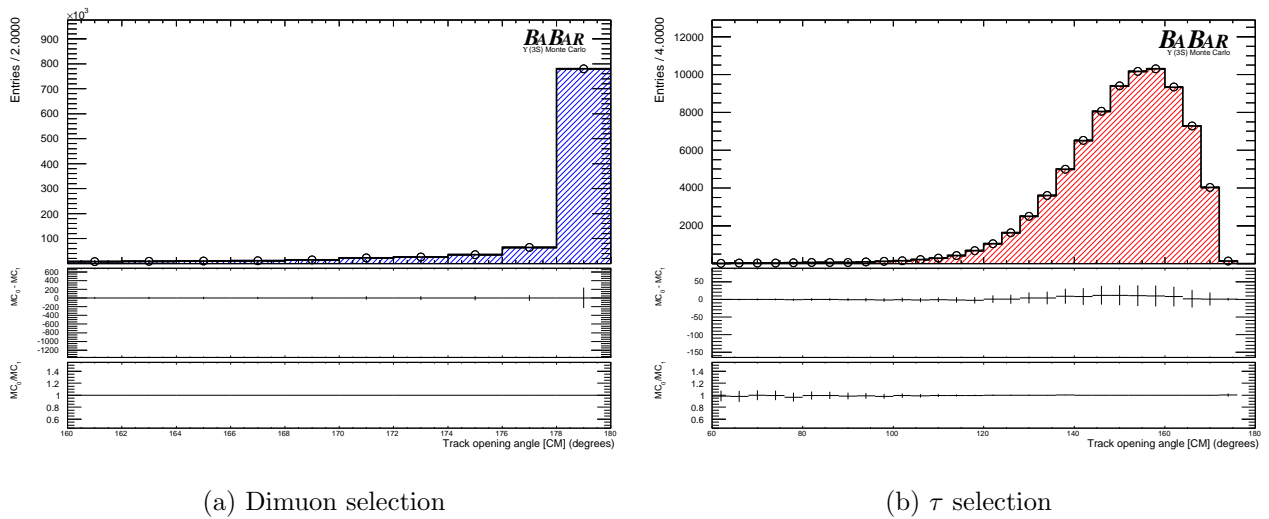
Figure 5.2: Effect of momentum resolution systematic shift on track opening angle in the CM. The data points are the unshifted case; The filled histogram shows the effect of the perturbation of the stochastic simulation.

(a) Dimuon selection

(b) τ selection
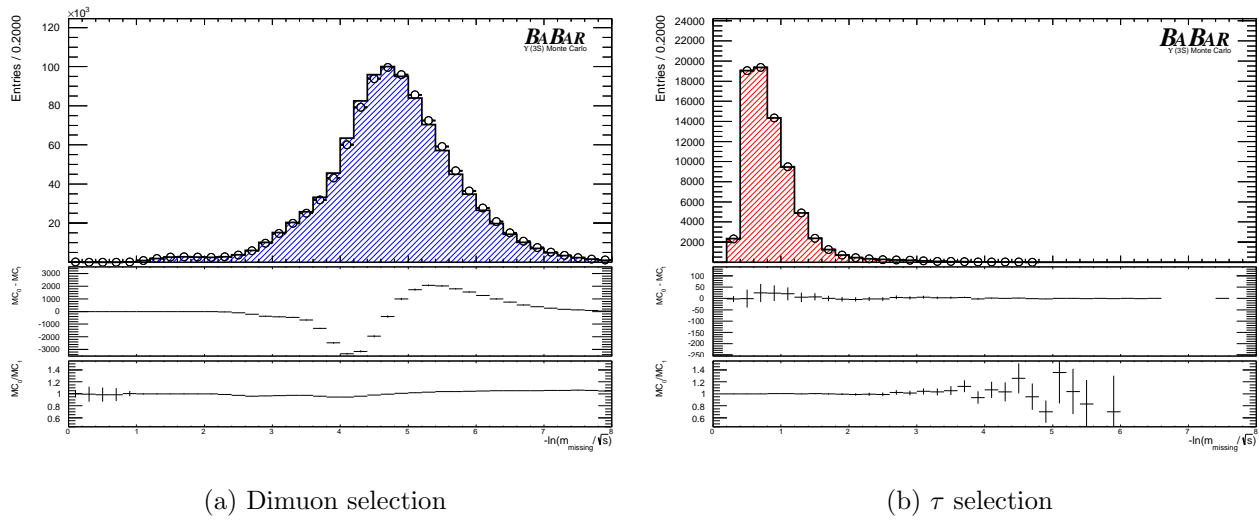
Figure 5.3: Effect of momentum resolution systematic shift on $-\ln \not{p}$. The data points are the unshifted case; The filled histogram shows the effect of the perturbation of the stochastic simulation. The effect of perturbing the momentum resolution appears to cause a similar shift as found in the data/MC agreement in Figure 4.15.

(a) Dimuon selection

(b) τ selection
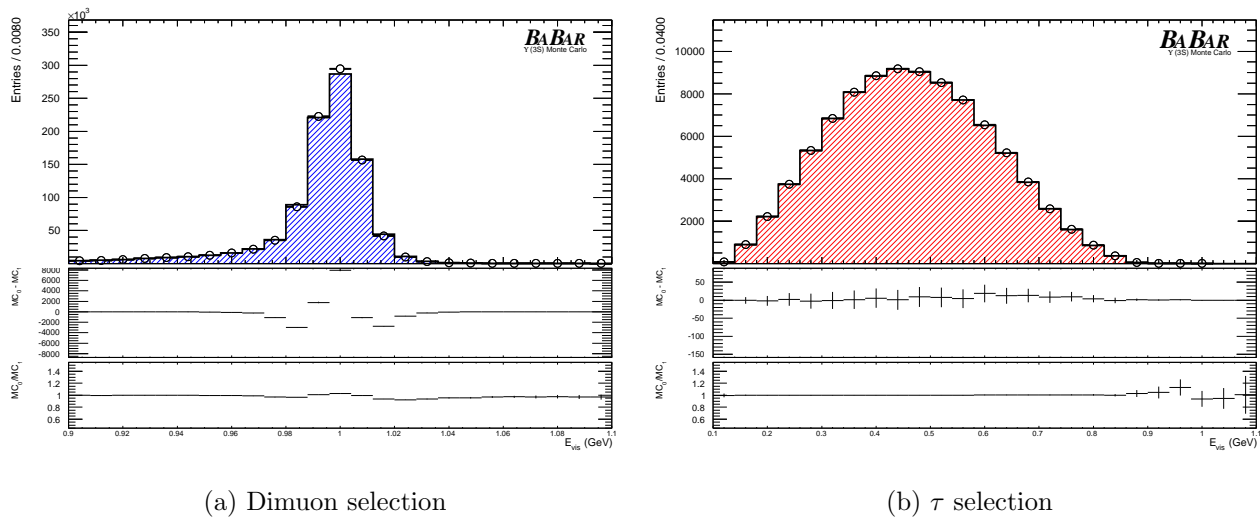
Figure 5.4: Effect of momentum resolution systematic shift on total visible energy (divided by the maximum beam energy). The data points are the unshifted case; The filled histogram shows the effect of the perturbation of the stochastic simulation.

(a) Dimuon selection

(b) τ selection
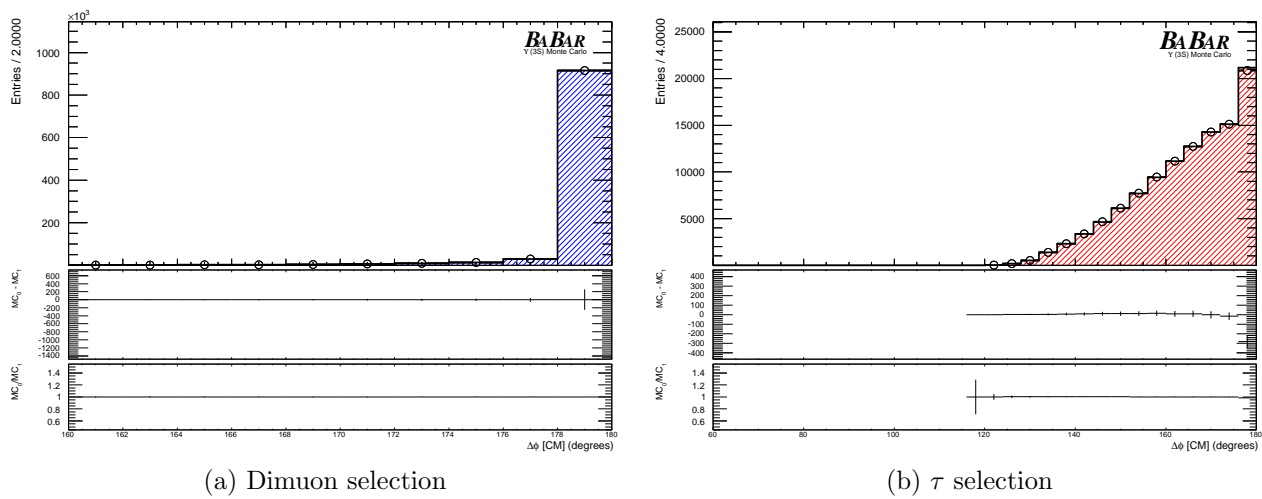
Figure 5.5: Effect of momentum resolution systematic shift on $\Delta\phi$ in the CM. The data points are the unshifted case; The filled histogram shows the effect of the perturbation of the stochastic simulation.

(a)   (b)
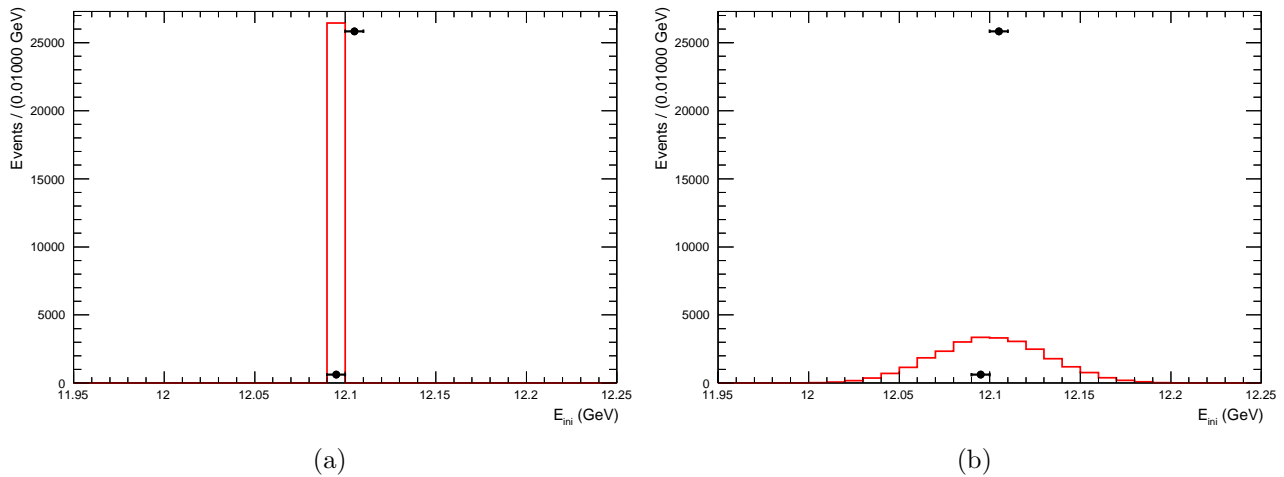
Figure 5.6: Effect of beam energy scale and resolution shifts on the initial energy. The **points** are the unshifted (or original values) and the histogram shows the effect of the systematic alteration.
(a) beam energy scale on the initial energy on a small sample of τ MC events ($\Upsilon(4S)$);
(b) beam energy resolution spread on the initial energy on a small sample of τ MC events ($\Upsilon(4S)$);

5.5 Error Propagation Calculator

An error propagation calculator (EPC) handles numerical simulation of functions that are composed of a large number of independent errors ($\mu_i \pm \sigma_{\mu_i}$). The EPC computes an estimated central value of the function and the associated standard deviation with respect to a subset of all errors. This is equivalent to normal error propagation provided the number of trials is *large* and the functions being evaluated are *well behaved*. The following must be noted:

1. This will only be as accurate as the number of simulations (N) (the estimated error on the mean scales as $1/\sqrt{N}$); and

2. The estimated error on σ scales as $1/\sqrt{2N}$ [28].

(a)

(b)
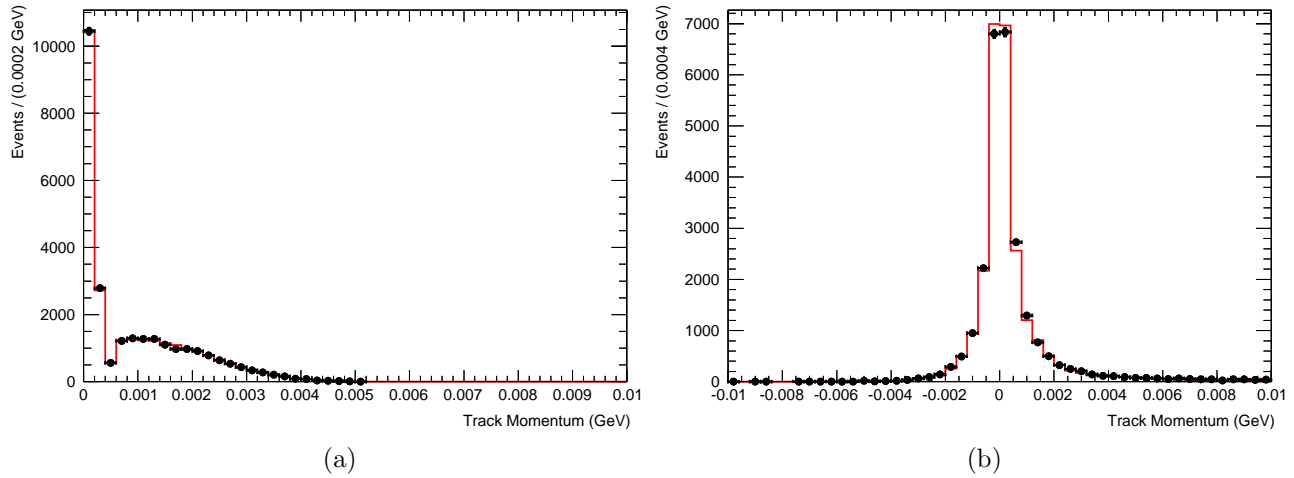
Figure 5.7: Effect of momentum scale and resolution systematic on the reconstructed laboratory momentum. The **black** points show the shift in reconstructed momentum for the first track $(|\mathbf{p}_{\text{unshifted}}| - |\mathbf{p}_{\text{shifted}}|)$ and the red histogram shows the shift in reconstructed momentume for the second track.
Figure (a) shows the effect of the momentum scale shift.
Figure (b) shows the effect of the momentum resolution shift.
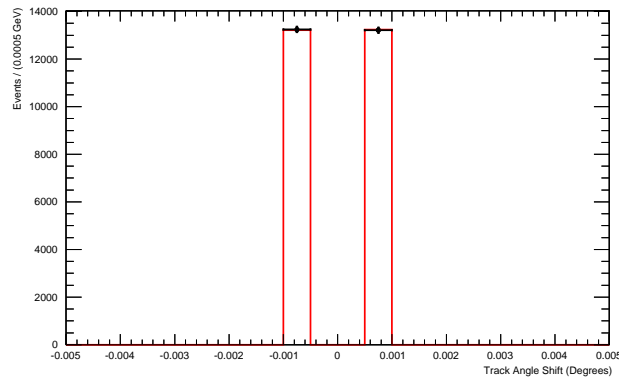
(a)

Figure 5.8: Effect of angular reconstruction resolution systematic shift on the reconstructed track angle. The **black** points shows the angular shift for the first track $(\theta_{\text{unshifted}} - \theta_{\text{shifted}})$ and the the red histogram shows the angular shift for the second track.

The result of the normal error approximation,

$$\sigma_f = \sum_{i,j} \frac{\partial f}{\partial x_i} \frac{\partial f}{\partial x_j} \sigma_{x_i} \sigma_{x_j} \tag{5.7}$$

is valid only for *small* errors. *Small errors* means that the differential with respect to any of the variables (x_i) does not change much over a few σ_i. Further problems can arise if any of the parameters, x_i, is similar in size to its associated error σ_i [28,55]. Using a numerical simulation for error propagation can provide an alternate method to the normal first order calculations (without the need to calculate a large number of derivatives)[7]. In this analysis, due to the large number of parameters used in various calculations, the numerical simulation is valid unless there are significant correlations between variables.

---

[7]This can also be done numerically assuming the function is *smooth*.

Chapter 6

Results and Systematic Studies

This section summarizes the projection of experimental sensitivity and the current status of the analysis.

6.1 Efficiencies

The selection efficiency of various modes must be known in order to correctly calculate the branching fraction and the estimated continuum cross section ratio. Efficiency is often (although not always) a quantity which requires the use of Monte Carlo simulated data[1]. Canonically, efficiency is defined as the number events that are accepted divided by the total number of events prior to selection. Clearly efficiency will have a binomial error since the data set is divided into two groups: (a) selected (with probability p) and (b) not selected (with probability $1 - p$). In such cases efficiency (ε) is defined as follows:

$$\varepsilon = \frac{N_{\text{selected}}}{N}, \tag{6.1}$$

where, N is the number of events prior to selection, and $N_{\text{selected}} \leq N$. Treating this as the associated probability p of the binomial distribution (which has a variance of $Np(1 - p)$) the error immediately becomes $\sqrt{p(1 - p)/N}$ or, in terms of the efficiency, $\sqrt{\varepsilon(1 - \varepsilon)/N}$. At best, the estimated efficiency is an unbiased estimate of the true efficiency and has a

---

[1]There are some cases where effective efficiency can be defined with regard to a specific data set, often called a control sample. A control sample is often used to improve data and Monte Carlo agreement.

statistical error estimate.

6.2 Systematic Uncertainties

Systematic uncertainties are measurement errors that are not due to statistical fluctuations in real or simulated data samples [56]. Neither trigger efficiency errors (determined from data statistics), nor detector acceptance errors (determined from Monte Carlo statistics), are treated as full systematic uncertainties. Therefore, they can be dealt with as statistical uncertainties. In the final result, such errors will be presented separately and then added to estimate the total systematic uncertainty.

The following list of the sources of systematic errors[2] and biases in high energy physics is important for all data analysis:

- ill-defined or poorly understood detector acceptances and trigger efficiencies;

- incorrect detector calibrations;

- poorly understood detector resolutions;

- ill-defined background;

- uncertainties in both simulation and underlying theoretical models;

- uncertainties with respect to input parameters such as cross sections, branching fractions, lifetimes, luminosity, and other factors often called 'external uncertainties';

- computational errors (floating point precision);

Systematic uncertainties may also originate from event reconstruction and selection processes, Monte Carlo simulation and detector modelling of backgrounds, as well as uncer-

---

[2]The terms systematic uncertainties, systematic errors or systematic are employed as synonyms through this paper.

tainties in estimating the signal efficiency. Blind analysis is often necessary to ensure that outcomes are not influenced by researcher bias.

Systematic uncertainties that arise from external sources include the luminosity measurement (which has its own set of statistical and systematic errors), the theoretical production cross sections of τ pairs and dimuons (and including other modes, such as Bhabha events), and the measured cross section for the $\Upsilon(3S)$

The theoretical cross sections for calculations are obtained using the Monte Carlo generator software. The generators are run in the `GeneratorsQA` framework.[3]

Systematic uncertainties are estimated by modifying the values of all Monte Carlo events. Given a Monte Carlo event, the reconstructed values or initial input parameters are perturbed to take into account the known detector resolutions and scale effects. Perturbation requires the use of Monte Carlo *truth*,[4] the Monte Carlo reconstructed values and a measured systematic parameter known in both Data and Monte Carlo events (e.g., momentum resolution, energy resolution, beam spread, etc.). This permits the study of a series of modifications[5] to all parameters of interest (including selection efficiency and background contamination rates) in order to establish the size of the shift in each specific item and the branching fraction ratio ($\mathcal{R}_{\tau/\mu}$). These estimates are often difficult (requiring large amounts of both computer and research time) since they involve the entire data-set, pseudo-random number generation and appropriate perturbation to measured parameters (scale, size, shifts, resolution alterations).

---

[3]In order to make this procedure less complex *BABAR* provides a Monte Carlo framework to handle setting up the appropriate generator. This proxy operates the `KK2F` Monte Carlo generator [45].

[4]There are a number categories that are used to describe Monte Carlo parameters, these include: simulated detector response (Monte Carlo hits and detector response), simulated reconstruction (Monte Carlo track and neutral reconstruction) and generator level Monte Carlo event information (Monte Carlo truth).

[5]In this case, the modifications are to a Monte Carlo value like the magnitude of the reconstructed track momentum or to initial input parameters (for example the beam energy). These modifications may be a fixed shift in the estimated scale of a particular parameter or a stochastic simulation to modify the spread of a parameter.

6.3 Luminosity Systematic Uncertainty

Although the luminosity uncertainty is determined from Bhabha, dimuon and two-photon events, the calculation also requires a knowledge of the ratio of integrated luminosities.[6] This ratio [1] was measured by the *BABAR* collaboration. The ratio of $\Upsilon(4S)$ `Run 6` on-peak to $\Upsilon(3S)$ `Run 7` on-peak is $78.350 \pm 0.013 \pm 0.417$ fb^{-1}/$25.557 \pm 0.025 \pm 0.150$ fb^{-1}. The `low` and `high` data samples when combined have a luminosity of $1.154 \pm 0.005 \pm 0.007$ fb^{-1} + $1.254 \pm 0.006 \pm 0.008$ fb^{-1}, while the unblind sample has $25.557 \pm 0.025 \pm 0.150$ fb^{-1}. The luminosity statistical and systematic errors between different data sets are treated as uncorrelated.

6.4 Momentum Scale, Resolution, and Angle

The systematic uncertainty due to scale modelling of the tracker was estimated by varying the momentum of all tracks in the Monte Carlo and then checking to see if this produced a modification in the total number of events that pass the selection. The corresponding scale and resolution uncertainties are discussed in [57]. Systematic uncertainty associated with the momentum scale is taken as the resultant change in the branching fraction ratio and certain other parameters of interest ($\mathcal{R}_{\tau/\mu}$, $\mathcal{B}(\Upsilon(3S) \to \tau\tau)$, $\mathcal{B}(\Upsilon(3S) \to \mu\mu)$, $\sigma_{\tau\tau}/\sigma_{\mu\mu}$) when the momentum scale of all Monte Carlo simulated tracks is shifted as follows:

$$\mathbf{p}_{\text{MC}}^{\text{shifted}} = \mathbf{s}(q) \times \mathbf{p}_{\text{MC}}^{\text{reco}} \tag{6.2}$$

where q is the charge of the track, $\mathbf{p}_{\text{MC}}^{\text{reco}}$ is the reconstructed momentum, and $\mathbf{s} \approx 1 - \delta \approx 0.999$.[7] For each mode, the effective selection efficiencies are used to calculate the shifted branching fraction ratio and the difference between the shifted ratio and the unshifted ratio

---

[6]Between 3S on-peak and off-peak luminosity.

[7]In the case of negative charged tracks, the ratio of data to Monte-Carlo momentum scale after reconstruction was 0.998294/0.998354. The positive charged tracks had a momentum scale ratio of 0.997573/0.998290 [57].

is the estimated systematic error. In the case $[\mu\mu^{\text{NO PID}}]$ $[e\not{e}]$, the shift in momentum scale causes the ratio to shift by $\delta\mathcal{R}_{\tau/\mu}$, +0.00035, which corresponds to a shift of +0.033 %. Therefore a systematic error of 0.033 % will be applied to the $\mathcal{R}_{\tau/\mu}$ in this case.

The systematic uncertainty due to the tracking detectors' resolution modelling is estimated by varying the reconstructed momentum of all tracks in the Monte Carlo samples as follows:

$$\mathbf{p}_{\text{MC}}^{\text{shifted}} = \text{S}(q)_{\text{p}} \times (\mathbf{p}_{\text{MC}}^{\text{reco}} - \mathbf{p}_{\text{MC}}^{\text{truth}}) + \mathbf{p}_{\text{MC}}^{\text{truth}} \tag{6.3}$$

where, q is the charge of the track, $\text{p}_{\text{MC}}^{reco}$ is the reconstructed momentum, $\text{p}_{\text{MC}}^{\text{truth}}$ is the truth momentum of the Monte Carlo simulated event, and S_{p} is the Data/Monte Carlo momentum resolution ratio. The effective momentum resolution ratio is 0.949 for positive tracks and 0.943 for negative tracks. The shift observed in the branching fraction ratio due to changing the momentum resolution is 0.18 %.

The modelling of momentum angle (θ) in the MC is accurate to 0.897×10^{-3} radians [57], so that the momentum angle is shifted by 0.897 milliradians and the resulting change in the branching fraction ratio is the uncertainty σ_θ. The shift in the ratio, $\delta\mathcal{R}_{\tau/\mu}$, is +0.00001 in the $[\mu\mu^{\text{NO PID}}]$ $[e\not{e}]$ case and corresponds to a negligible systematic error of 0.0001 %.

6.4.1 Energy Scale and Resolution

The energy scale and energy resolution systematic is determined in an analogous way to that used for momentum scale and momentum resolution. The initial error (based upon prior BaBar analyses) was expected to be on the order of 0.2 %. The systematic error associated with the energy scale is 0.057 %. The energy scale systematic involved shifting the measured value of all reconstructed photon clusters (E_{reco}) with a non-zero truth value (E_{true}) and which were not reconstructed photon conversions,

$$\text{E}_{\text{reco}}^{\star} = \text{E}_{\text{reco}} + \lambda. \tag{6.4}$$

where $\lambda = -2$ MeV [57].

On the other hand, the resolution is perturbed as follows:

$$E^\star_{\text{reco}} \;=\; E_{\text{true}} + (E_{\text{reco}} - E_{\text{true}}) \times \lambda \tag{6.5}$$

where λ is a Gaussian-generated random number with a mean corresponding to the Data/MC resolution ratio — (0.0281 GeV/0.0297 GeV) (measured by fitting a photon transition peak) with a standard deviation corresponding to the associated error of that term (14 %). The resulting E_{reco} must be positive and the overall systematic uncertainty associated with this was 0.305 % (in the case of the ratio, $\mathcal{R}_{\tau/\mu}$).

6.4.2   Beam Energy Scale and Energy Spread Systematic Error

The mean beam energy is known to an accuracy of 4 MeV [6], therefore the systematic uncertainty resulting from the beam energy scale is determined by shifting the centre-of-mass energy by 4 MeV. The maximum shift in the measured parameter induced by any of the four possible shifts of beam energy will define its associated systematic uncertainty. Since the beam energy shift between on- and off-peak might be in different directions, the overall size of the systematic should be estimated using all four possible cases. Previous *BABAR* analyses estimated the contribution to branching fraction measurements to be on the order of 0.05 % for τ decays. This shift should also have a similar effect on efficiencies as the momentum scale shift and the overall systematic uncertainty on $\mathcal{R}_{\tau/\mu}$ is found to be 0.007 %.

The *beam spread* systematic uncertainty was estimated by replacing the initial Monte Carlo beam energy with a Gaussian-distributed beam energy which has the same mean as the initial beam energy and a width of 2.5 MeV. When using boost spread as a measure of beam spread, the estimated uncertainty is around 1 MeV; therefore the result from a 2.5 MeV variation should be an over-estimate of the overall systematic uncertainty. Perturbing the beam energy in this manner led to an overall systematic error of 0.07 % on the $\mathcal{R}_{\tau/\mu}$.

6.4.3   Background Branching Ratios

Some of the intrinsic backgrounds have large uncertainties in the branching fractions: An example of this can be seen in the case of $\Upsilon(3S)$ decays through intermediate hadronic channels into $\Upsilon(2S)$ or $\Upsilon(1S)$ and subsequently to dimuons or τ-pairs. These backgrounds are subtracted from the observed number of τ- or μ-pairs. To estimate the systematic error, due to the lack of perfectly measured branching ratios, the estimated number of events passing the selection of these background decays is shifted up or down by the estimated error on the individual decay channels. This modification to the estimated background contamination causes a shift in the branching fraction ratio ($\mathcal{R}_{\tau/\mu}$).

The branching fractions could be off by a global 10 % in the case of the $\Upsilon(3S)$ cascade decays [12]. A large fraction of the estimated background is due to intermediate hadronic cascades. The estimated background changes by roughly 3 % (since there are four different subtypes of cascades) and the overall ratio changes by 0.09 %. This systematic uncertainty was perturbed in both the positive and negative directions (with the largest fluctuation taken as the systematic error). However, there should be a compensating effect on other backgrounds and decays which tends to decrease in frequency. For example, if $\Upsilon(2S)$ associated cascades fluctuate up, the expectation is that $\Upsilon(1S)$ decays would consequently have to account for a smaller number of decays of $\Upsilon(3S)$. Therefore a value of 0.09 % can be assigned as the overall systematic error due to uncertainty in cascade branching fractions[8]. To the first order, these cascade decays have no systematic uncertainty when calculating the cross section ratio at $\sqrt{s} = m_{\Upsilon(4S)}$.

Other backgrounds, such as two-photon, Bhabhas, hadronic, dimuon contamination of τ selection, and τ contamination of dimuon selections were investigated. The estimated number of events associated with background contamination is given by the equation,

---

[8]A large number of these backgrounds can be removed by removing events where a neutral cluster has a measured energy consistent with the known transition peaks; this would reduce statistical sensitivity of the final measurement.

$$\text{Bkg}^{\text{type}}(\sqrt{s}) = \varepsilon^{type}\mathcal{L}(\sqrt{s})\sigma^{type}, \tag{6.6}$$

where ε is the estimated selection efficiency, $\mathcal{L}$ is the luminosity recorded by the BABAR detector at some centre-of-mass energy $(\sqrt{s})$, and σ^{type} is the theoretical cross section at the same centre-of-mass energy. Although all backgrounds exhibit a correlation with luminosity, the dominant associated error is selection efficiency. These numbers are found in Table 6.24.

6.4.4 τ Branching Fraction Systematic

The lifetime of the τ lepton is so short that all τ leptons produced will decay to other particles before the they can reach the detector material. The selection *efficiency* for τ decays necessitates adding an additional term, to quantify the associated branching fractions. Hence, the actual estimated number of τ lepton pairs selected has the following form:

$$N_{\tau\tau}^{\text{selected}} = N_{\tau\tau}^{\text{produced}}\varepsilon(\tau \to e\nu\nu)\mathcal{B}(\tau \to e\nu\nu) \sum_{\lambda=\mu,\pi,\rho,a_1} \big(\varepsilon(\tau \to \lambda\nu)\mathcal{B}(\tau \to \lambda\nu(\nu))\big), \tag{6.7}$$

where $\varepsilon(\lambda)$ is the efficiency of selection of the mode λ, and $\mathcal{B}(\lambda)$ is the PDG measured branching fraction of the mode λ. The selection efficiency for each of these modes is documented in Tables 6.6-6.10. Each of these modes is simulated with an effective branching fraction (i.e, the generator contains fixed branching fractions, as shown in Table 6.1 and Table 6.2). However, each of these values should must have an associated measurement error. The Particle Data Group (PDG)[9] aggregates particle physics results (including branching fraction and ratios), measured by different experimental groups, and provides a world average and an associated error. The PDG values are listed in Table 6.3. Implicitly, there must be an additional systematic uncertainty[10] and a correction[11] associated with the τ selection

---

[9]An international collaboration that reviews particle physics and related areas of astrophysics, and compiles/analyses data on particle properties.

[10]This is due to the uncertainty associated with the measured branching fraction.

[11]Because the branching fractions used at the generator level have not been updated to the current world average, the incorrect branching fractions at the generator level needs to be corrected.

efficiency of both continuum[12] and $\Upsilon(3S)$ decays[13].

Decay Mode	EvtGen Branching Fraction	Branching Fraction
$e^-\overline{\nu}_e\nu_\tau$	0.1778	(0.1783 ± 0.0004) [12]
$\mu^-\overline{\nu}_\mu\nu_\tau$	0.1731	(0.1741 ± 0.0004) [12]
$\pi^-\nu_\tau$	0.1095	(0.1083 ± 0.0006) [12]
$\pi^-\pi^0\nu_\tau$	0.2531	(0.2552 ± 0.0009) [12]
$K^-\nu_\tau$	0.00686	(0.00700 ± 0.00010) [12]
$\pi^-2\pi^0\nu_\tau$	0.0910	(0.0930 ± 0.0011) [12]
$\pi^-3\pi^0\nu_\tau$	0.0100	(0.0105 ± 0.0007) [12]

Table 6.1: Branching Fraction Comparison between EvtGen and PDG world averages. The Heavy Flavour Averaging Group (HFAG) [58] provides an alternate (but similar estimate to the PDG); PDG [12].

Decay Mode	TAUOLA Branching Fraction	Branching Fraction
$e^-\overline{\nu}_e\nu_\tau$	0.17865206	(0.1783 ± 0.0004) [12]
$\mu^-\overline{\nu}_\mu\nu_\tau$	0.17355202	(0.1741 ± 0.0004) [12]
$\pi^-\nu_\tau$	0.11084165	(0.1083 ± 0.0006) [12]
$\pi^-\pi^0\nu_\tau$	0.25375548	(0.2552 ± 0.0009) [12]
$K^-\nu_\tau$	0.0069460408	(0.00700 ± 0.00010) [12]
$\pi^-(2\pi)\nu_\tau$	0.18356709	(0.0930 ± 0.0011) [12]
$\pi^-3\pi^0\nu_\tau$	0.012619074	(0.0105 ± 0.0007) [12]

Table 6.2: Branching Fraction Comparison between TAUOLA and PDG world averages. The TAUOLA branching fractions are reproduced exactly as they appear within the code.

$\Upsilon(3S)$ decays are generated through the EVTGEN generator which produces all decay channels. Pertinent details are highlighted in Section B.2. Each decay channel has a branching fraction and decay mechanism such that the dynamics of the decay modes are estimated properly. Due to the fact that high energy physics (HEP) experiments extend over many years, the branching fractions in the generators have remained fixed, in contrast to the values estimated by the PDG (which are regularly updated with more recent measurements).

Similarly, QED or continuum decays are generated through KK2F and TAUOLA. The branching fractions are listed in TauolaDecayModes.txt (see Appendix B). Some decay modes also

---

[12]Uses KK2F and TAUOLA.

[13]Uses EVTGEN

have differences from the current PDG branching fractions.

The following checks are used to verify the veracity of this procedure:

- The associated systematic error on efficiency ratios ($\varepsilon_{\tau\tau}^{\text{4S continuum}}/\varepsilon_{\tau\tau}^{\text{3S continuum}}$) should be almost zero.

- The associated systematic uncertainty on $\varepsilon_{\tau\tau}^{\text{4S continuum}}$ to the first order should be identical to $\varepsilon_{\tau\tau}^{\text{3S continuum}}$.

- The associated systematic uncertainty on $\varepsilon_{\tau\tau}^{\Upsilon(3S)\to\tau^+\tau^-}$ should be different and uncorrelated with continuum events.

- The associated bias of the efficiency ratio ($\varepsilon_{\tau\tau}^{\text{4S continuum}}/\varepsilon_{\tau\tau}^{\text{3S continuum}}$) should be negligible.

Decay Mode	Branching Fraction (%)
$\tau^- \to e^- \overline{\nu}_e \nu_\tau$	17.83 ± 0.04
$\tau^- \to \mu^- \overline{\nu}_\mu \nu_\tau$	17.41 ± 0.04
$\tau^- \to (\text{had})^- \nu_\tau (\text{neutrals} = 0)$	11.53 ± 0.06
$\tau^- \to (\text{had})^- \nu_\tau (\text{neutrals} \geq 1)$	36.58 ± 0.10

Table 6.3: PDG Branching Fractions of one prong τ decays.

Although these branching fractions are known to a precision of roughly 1 part in 450, this uncertainty will have an effect on any measurement using reconstructed τ decays. As a check, the error on $\tau \to e\overline{\nu}_e\nu_\tau$ will give a relative uncertainty on any value with $\varepsilon(\tau)$ of $0.04/17.83 = 0.22$ %. Further, the associated error of the sum term (neglecting the efficiency of observing the separate modes - assuming they are exactly the same) is calculated using the sum of the relative errors added in quadrature. This leads to a final relative uncertainty of 0.29 %[14] where all errors have been added in quadrature.

---

[14]This estimate ignores the relative differences in selection efficiency and the overall corrections for the generated branching fractions, which is correctly done in this analysis.

Decay Mode	Relative Fraction (%)	Relative Error (%)
$\tau^- \to \mu^- \overline{\nu}_\mu \nu_\tau$	26.572	0.061
$\tau^- \to (\text{had})^- \nu_\tau (\text{neutrals} = 0)$	55.830	0.153
$\tau^- \to (\text{had})^- \nu_\tau (\text{neutrals} \geq 1)$	17.598	0.092
Total	100.000	0.189

Table 6.4: Relative Fraction and Relative Error of associated decay modes.

Decay Mode	Energy Scale (GeV)	Events Selected	Events Generated	Efficiency
$e^- \overline{\nu}_e \nu_\tau$	$\sqrt{s} = m_{\Upsilon(3S)}$	1.5668189×10^6	$0.17865206 \times 57322000$	0.15299
$\mu^- \overline{\nu}_\mu \nu_\tau$	$\sqrt{s} = m_{\Upsilon(3S)}$	1.831×10^2	$0.17355202 \times 57322000$	0.00001840
$\pi^- \nu_\tau$	$\sqrt{s} = m_{\Upsilon(3S)}$	2.5648×10^3	$0.11084165 \times 57322000$	0.00040355
$\pi^- \pi^0 \nu_\tau$	$\sqrt{s} = m_{\Upsilon(3S)}$	2.0544×10^3	$0.25375548 \times 57322000$	0.00014124

Table 6.5: Estimated continuuum τ selection efficiency for the electron hemisphere ($\sqrt{s} = m_\Upsilon(3S)$). "Events generated" for each mode is actually a random variable. It has an associated error, which is estimated as $\sqrt{Np(1-p)}$.

Decay Mode	Energy Scale (GeV)	Events Selected	Events Generated	Efficiency
$e^- \overline{\nu}_e \nu_\tau$	$\sqrt{s} = m_{\Upsilon(3S)}$	24873.3	$0.17865206 \times 57322000$	0.002428868
$\mu^- \overline{\nu}_\mu \nu_\tau$	$\sqrt{s} = m_{\Upsilon(3S)}$	414133	$0.17355202 \times 57322000$	0.041628314
$\pi^- \nu_\tau$	$\sqrt{s} = m_{\Upsilon(3S)}$	301736	$0.11084165 \times 57322000$	0.04749007
$\pi^- \pi^0 \nu_\tau$	$\sqrt{s} = m_{\Upsilon(3S)}$	549930	$0.25375548 \times 57322000$	0.037806863
$K^- \nu_\tau$	$\sqrt{s} = m_{\Upsilon(3S)}$	19537.4	$0.00694604 \times 57322000$	0.049069106
$\pi^- 3\pi^0 \nu_\tau$	$\sqrt{s} = m_{\Upsilon(3S)}$	24185.1	$0.0126191 \times 57322000$	0.033434756

Table 6.6: Estimated continuuum τ selection efficiency for the not-electron hemisphere ($\sqrt{s} = m_\Upsilon(3S)$). "Events generated" for each mode is actually a random variable. It has an associated error, which is estimated as $\sqrt{Np(1-p)}$. The efficiency includes the branching fraction, and is scaled by a factor of $\mathcal{B}(\tau \to ...)$. The size of the associated branching fraction error is 0.03 % for the first four types. 0.16 % for fifth type. 0.12 % for type sixth type.

Decay Mode	Energy Scale (GeV)	Events Selected	Events Generated	Efficiency
$e^-\overline{\nu}_e\nu_\tau$	$\sqrt{s} = m_{\Upsilon(3S)}$	187861	$0.022 \times 0.1778 \times 257432000$	0.186560484
$\mu^-\overline{\nu}_\mu\nu_\tau$	$\sqrt{s} = m_{\Upsilon(3S)}$	16.8046	$0.022 \times 0.1731 \times 257432000$	0.000017141
$\pi^-\nu_\tau$	$\sqrt{s} = m_{\Upsilon(3S)}$	319.405	$0.022 \times 0.1095 \times 257432000$	0.000515041
$\pi^-\pi^0\nu_\tau$	$\sqrt{s} = m_{\Upsilon(3S)}$	230.589	$0.022 \times 0.2531 \times 257432000$	0.000160864

Table 6.7: Estimated $\Upsilon(3S) \to \tau\tau$ selection efficiency for the electron hemisphere. Since there are many decay channels simulated, decays of the $\Upsilon(3S)$ to τ-pairs should have an associated Poisson distributed error of 0.42 % ($\sqrt{0.022 \times 257432000}/0.022 \times 257432000 = \sqrt{5663504}/5663504 = 0.000420201$). Total relative error on $e^-\overline{\nu}_e\nu_\tau$ would be roughly 0.1 %. The efficiency includes the branching fraction, and is scaled by a factor of $\mathcal{B}(\tau \to ...)$ and scaled by the generator branching fraction of 0.022 ($\mathcal{B}(\Upsilon(3S) \to \tau\tau)$).

Decay Mode	Energy Scale (GeV)	Events Selected	Events Generated	Efficiency
$e^-\overline{\nu}_e\nu_\tau$	$\sqrt{s} = m_{\Upsilon(3S)}$	3008.04	$0.022 \times 0.1778 \times 257432000$	0.002987216
$\mu^-\overline{\nu}_\mu\nu_\tau$	$\sqrt{s} = m_{\Upsilon(3S)}$	50979.4	$0.022 \times 0.1731 \times 257432000$	0.052023722
$\pi^-\nu_\tau$	$\sqrt{s} = m_{\Upsilon(3S)}$	35565.3	$0.022 \times 0.1095 \times 257432000$	0.057349171
$\pi^-\pi^0\nu_\tau$	$\sqrt{s} = m_{\Upsilon(3S)}$	60981.4	$0.022 \times 0.2531 \times 257432000$	0.042542208
$K^-\nu_\tau$	$\sqrt{s} = m_{\Upsilon(3S)}$	2308.24	$0.022 \times 0.00686 \times 257432000$	0.059411652
$\pi^-3\pi^0\nu_\tau$	$\sqrt{s} = m_{\Upsilon(3S)}$	2034.52	$0.022 \times 0.0100 \times 257432000$	0.035923343

Table 6.8: Estimated $\Upsilon(3S) \to \tau\tau$ selection efficiency for the not-electron hemisphere. Since there are many decay channels simulated, decays of the $\Upsilon(3S)$ to τ-pairs should have an associated Poisson distributed error of 0.42 % ($\sqrt{0.022 \times 257432000}/0.022 \times 257432000 = \sqrt{5663504}/5663504 = 0.000420201$). The efficiency includes the branching fraction, and is scaled by a factor of $\mathcal{B}(\tau \to ...)$ and scaled by the generator branching fraction of 0.022 ($\mathcal{B}(\Upsilon(3S) \to \tau\tau)$).

Decay Mode	Energy Scale (GeV)	Events Selected	Events Generated	Efficiency
$e^-\overline{\nu}_e\nu_\tau$	$\sqrt{s} = m_{\Upsilon(4S)}$	3.63559×10^6	$0.17865206 \times 139424000$	0.14595848
$\mu^-\overline{\nu}_\mu\nu_\tau$	$\sqrt{s} = m_{\Upsilon(4S)}$	512.147	$0.17355202 \times 139424000$	0.0000021165
$\pi^-\nu_\tau$	$\sqrt{s} = m_{\Upsilon(4S)}$	6891.13	$0.11084165 \times 139424000$	0.000445265
$\pi^-\pi^0\nu_\tau$	$\sqrt{s} = m_{\Upsilon(4S)}$	5295.87	$0.25375548 \times 139424000$	0.000149687

Table 6.9: Estimated continuuum τ selection efficiency for the electron hemisphere ($\sqrt{s} = m_\Upsilon(4S)$). "Events generated" for each mode is actually a random variable. It has an associated error, which is estimated as $\sqrt{Np(1-p)}$. The efficiency includes the branching fraction, and is scaled by a factor of $\mathcal{B}(\tau \to ...)$. The size of the associated branching fraction error is 0.02 % for the first type.

Decay Mode	Energy Scale (GeV)	Events Selected	Events Generated	Efficiency
$e^-\overline{\nu}_e\nu_\tau$	$\sqrt{s} = \Upsilon(4S)$	64952.7	$0.17865206 \times 139424000$	0.002607664
$\mu^-\overline{\nu}_\mu\nu_\tau$	$\sqrt{s} = \Upsilon(4S)$	951074	$0.17355202 \times 139424000$	0.039304936
$\pi^-\nu_\tau$	$\sqrt{s} = \Upsilon(4S)$	697003	$0.11084165 \times 139424000$	0.045101826
$\pi^-\pi^0\nu_\tau$	$\sqrt{s} = \Upsilon(4S)$	1.2831×10^6	$0.25375548 \times 139424000$	0.036266658
$K^-\nu_\tau$	$\sqrt{s} = \Upsilon(4S)$	45448.4	$0.00694604 \times 139424000$	0.046929268
$\pi^-3\pi^0\nu_\tau$	$\sqrt{s} = \Upsilon(4S)$	56166	$0.0126191 \times 139424000$	0.031923285

Table 6.10: Estimated continuuum τ selection efficiency for the not-electron hemisphere ($\sqrt{s} = m_\Upsilon(4S)$). "Events generated" for each mode is actually a random variable. It has an associated error, which is estimated as $\sqrt{Np(1-p)}$. The efficiency includes the branching fraction, and is scaled by a factor of $\mathcal{B}(\tau \to ...)$. The size of the associated branching fraction error is 0.02 % for the first four types. 0.1 % for fifth type. 0.075 % for type sixth type.

To get a complete estimate of the bias and the *PDG* branching fraction systematic uncertainty the following procedure is necessary:

1. Take τ decay modes and rescale the numbers to match the PDG.

2. Recalculate efficiencies and generate a scale to correct for bias;

3. Introduce an additional uncertainty associated with each mode

which can be represented as,

$$\varepsilon^{\text{corrected}}(\sqrt{s}, \lambda) = \frac{\mathcal{B}(\tau \to \lambda, \text{PDG})}{\mathcal{B}(\tau \to \lambda, \text{Generator})}\varepsilon^{\text{measured}}(\sqrt{s}, \lambda). \tag{6.8}$$

Determining the final selection efficiency requires a correction to the initial estimated selection efficiency of the electron track multiplied by the correction to the not-electron track ($\not{e}$). The efficiency correction for `EvtGen` simulated decays is calculated to be 1.0061 ± 0.0025 for the electron track and 1.0028 ± 0.0022 for the not-electron track (this involves all possible one-track branching fractions that are not electrons as well as the associated tracks that involve mis-identified electrons). All of this leads to the following full correction of 1.0089 ± 0.0033 (which has an estimated uncertainty close to the earlier estimate 0.29 %).

TAUOLA simulates τ decays at different centre-of-mass energies. However the branching fractions are independent of centre-of-mass energy. It should be noted that the measured efficiency will be different because of the random nature of the simulated processes and the changes in detection efficiencies due to a different centre-of-mass frame boosts. In this case, three corrections were calculated, one for each of: $\varepsilon_{\Upsilon(4S)}$, $\varepsilon_{\Upsilon(3S)}$ and $\varepsilon_{\Upsilon(4S)}/\varepsilon_{\Upsilon(3S)}$ (see Table 6.11).

	e Correction	$\not{e}$ Correction	Total
$\varepsilon_{\Upsilon(4S)}$	0.9975 ± 0.0025	0.9980 ± 0.0022	0.9955 ± 0.0033
$\varepsilon_{\Upsilon(3S)}$	0.9975 ± 0.0025	0.9980 ± 0.0022	0.9955 ± 0.0033
$\varepsilon_{\Upsilon(4S)}/\varepsilon_{\Upsilon(3S)}$	—	—	0.999981 ± 0.000013

Table 6.11: Branching Fraction Correction for τ Decays as simulated by TAUOLA.

6.4.5   Particle Identification

The particle identification (PID) group's control samples (from which the official BABAR PID tables are produced) have track and photon multiplicities and distributions that can be different from those of the τ and μ events in this analysis. These differences alter efficiency corrections and subsequently the Data-to-MC weights of PID selectors. Using a set of control samples, PID tables are produced to correct the relative differences between data and MC selection efficiencies. These tables are made up of cells or bins of transverse momentum (p), track polar angle (θ), and track azimuthal angle (ϕ).

The PID tables are used to generate a per-event *weight* used as a correction of the Monte Carlo simulations to account for detector modelling deficiencies. Further, since these tables are generated on a per-run basis, this also provides a means of correcting for the variation over time of these runs. Due to the underlying random nature of both data and Monte Carlo control samples, it is necessary to determine the systematic error involved in applying PID corrections. The PID environmental uncertainty is the difference between the data-PID efficiency and the MC-PID efficiency after being corrected.

6.4.6 Systematic Error Due to PID Table Statistics

The systematic uncertainty associated with applying PID corrections was determined using *toy simulation.* This involved the generation of 100 alternative PID tables. Each of which was generated through a process of random changes to each bin[15] (i.e. each of these updated bins was created using a random number generator to simulate a new value for the selection efficiency). The bin-wise toy efficiency is simulated using a binomial distribution when the total number of events prior to selection is small ($N_{\mathrm{prior}} \leq 20$), otherwise it uses the following Gaussian trial:

$$\varepsilon_i^{\mathrm{TOY}} = \lambda(\mu = \varepsilon^{\mathrm{Original}_i}, \sigma = \sigma_\varepsilon^{\mathrm{Original}}) \tag{6.9}$$

where, i is the associated bin, ε is used to denote the data or MC selection efficiency, σ_ε is the associated statistical error of the efficiency and λ is a Gaussian random variable with a mean of $\varepsilon^{\mathrm{Original}_i}$ and a width of $\sigma_\varepsilon^{\mathrm{Original}}$. This is a bootstrapping method, using the original PID table as a generator for a new PID table, where the size of the fluctuations are estimated by the statistics of the control samples.

The tracks used to generate PID tables for the electron selectors are low-multiplicity events (the electron PID selector uses radiative Bhabha events as the control sample, while muon PID control samples involve dimuons). The event selection for this paper is low-multiplicity τ events. The selection environment has equivalent multiplicity to the control samples used to generate the PID tables[16] so the toy PID table simulation standard deviation (RMS) will be used as the full systematic uncertainty for the statistical uncertainty associated with PID corrections.

Using PID introduces uncertainty with respect to each bin's effective efficiency (data) and truth efficiency determination (MC). Due to the nature of random processes it can be expected that the statistical distribution and purity of the PID control samples will be a

---

[15]So, given a particular p_t, θ, ϕ bin: a toy PID table would have different entries.

[16]Further the tracks should be reasonably separated in both cases.

Poisson process at the bin level.[17] At the detector level there can be correlations between PID control samples and the observed final states, but this type of systematic error is negligible when considering two-track events.

Once the data and the Monte Carlo toy PID tables are generated, the mean value of the PID *weight* is used as a measure of the change due to PID table statistical variation. Since each toy PID table can be used in place of the original PID table, the associate spread (or RMS) of this distribution is taken as the effective relative error on the selection efficiency. The estimated mean PID weight for the τ selection is,

1. 1.00453 ± 0.00078 ($e^+e^- \to \tau^+\tau^-$ at $\sqrt{s} = m_{\Upsilon(4S)}$);

2. 1.00181 ± 0.00038 ($\Upsilon(3S)$);

3. 1.00198 ± 0.00038 ($e^+e^- \to \tau^+\tau^-$ at $\sqrt{s} = m_{\Upsilon(3S)}$).

The effective mean PID weight is a modification of the overall estimated efficiency, as follows,

$$\varepsilon(\text{total}) = \varepsilon(\text{PID weight})\varepsilon(\text{selection}) \tag{6.10}$$

where $\varepsilon(\text{PID weight})$ is the effective mean PID weight and $\varepsilon(\text{selection})$ is the selection efficiency without PID weighting. The overall estimated systematic error due to the statistical variation with respect to PID selection and weighting is given in Tables 6.25, 6.26, and 6.28. There are no PID selectors for $e^+e^- \to \mu^+\mu^-$, therefore there are no errors associated with the use of PID tables (see Table 6.27).

6.5 π^0 Systematic

In this analysis the π^0 veto is only applied to one hemisphere (either the higher lab momentum muon for dimuon selection or the track identified as an electron for τ-pair selection).

---

[17]Technically the distribution should be a multidimensional probability distribution (with global Poisson behaviour) because the simple bin-wise assumption will over-estimate errors.

	Selected	Prior	Pseudo-efficiency
Dimuon (Data)	2.50239×10^7	2.50828×10^7	0.997651 ± 0.0000097
Dimuon (MC)	2.52873×10^7	2.53432×10^7	0.997794 ± 0.0000093
τ (Data)	1.93551×10^6	1.95633×10^6	0.989358 ± 0.000073
τ (MC)	1.94044×10^6	1.96029×10^6	0.989874 ± 0.000072

Table 6.12: Pseudo-efficiency and the number of events that pass the dimuon selection ($\Upsilon(4S)$).

Since both selections require events which do not have π^0 in one of the hemispheres, the contamination by uds and $c\bar{c}$ events is decreased.

Because vetoing events with a π^0 introduces an additional systematic error it is necessary to quantify the size of this systematic. This is done by establishing a *pseudo-efficiency* comparison between Data and MC for both τ and dimuon selection. It is called a pseudo-efficiency (ε^*), because the true number of data events is unknown and it is given by,

$$\varepsilon^* = \frac{\mathrm{N_{selected}}}{\mathrm{N_{prior}}} \tag{6.11}$$

where $\mathrm{N_{selected}}$ is the number of events that pass the selection after applying the π^0 veto and $\mathrm{N_{prior}}$ is the number of events that pass the selection without applying the π^0 veto. The ratios,

$$\varepsilon^*_{\mu\mu}(\mathrm{DATA})/\varepsilon^*_{\mu\mu}(\mathrm{MC}) \tag{6.12}$$

and

$$\varepsilon^*_{\tau\tau}(\mathrm{DATA})/\varepsilon^*_{\tau\tau}(\mathrm{MC}) \tag{6.13}$$

provide a metric to estimate the systematic for applying the π^0 veto to dimuon and τ-pair selection.

Table 6.12 shows the pseudo-efficiency in each selection case. The relative deviation from unity will be taken as the estimated systematic uncertainty (see Table 6.13). Although, some cancellation of the systematic errors between τ and μ selection efficiency is expected

	Pseudo-efficiency Ratio	Estimated Systematic
Dimuon	0.9998567 ± 0.000014	0.015%
τ	0.9994787 ± 0.00010	0.052%

Table 6.13: Pseudo-efficiency ratio related to π^0 veto.($\Upsilon(4S)$).

$(\varepsilon_{\tau\tau}(\sqrt{s_0})/\varepsilon_{\mu\mu}(\sqrt{s_0}))$ the conservative approach is to assume no cancellation and add the two systematic errors in quadrature. Therefore the estimated systematic error is 0.054 % (on both the cross section ratio and $\mathcal{R}_{\tau/\mu}$), but in the case of the estimated individual τ efficiency ratios, i.e. $\varepsilon_{\tau\tau}(\sqrt{s_0})/\varepsilon_{\tau\tau}(\sqrt{s_1})$, the error will be treated as 100 % correlated (similar to the dimuon efficiency ratio $\varepsilon_{\mu\mu}(\sqrt{s_0})/\varepsilon_{\mu\mu}(\sqrt{s_1})$).

6.5.1 Boost

For $\Upsilon(3S)$ on-peak data, the centre-of-mass energy was fixed to $m_{\Upsilon(3S)} = 10.3552$ GeV/c^2. This was achieved at PEP-II by tuning the beam energies. The low energy beam was kept at a fixed energy of $\text{E}_{\text{LER}} = 3.11175$ GeV and the high energy beam was adjusted to the desired centre-of-mass energy which should be accurate to ± 2 MeV. The off peak energy is required to be $m_{\Upsilon(3S)} - 30$ MeV achieved by tuning the high energy beam. The estimated size of the boost error is about 10^{-3} which corresponds roughly to an angular mis-alignment of 1 to 3 mrad.

In order to minimize the associated systematic error due to accelerator estimation, a *lab-to-centre-of-mass* boost correction was determined.

Beginning at the centre-of-mass system of an associated $\Upsilon(\mathbf{nS})$, with a fixed mass, $\text{M}_{\Upsilon(\mathbf{nS})}$ the momentum of such a system is given by

$$p^\mu = (\text{M}_{\Upsilon(\mathbf{nS})}, \mathbf{0}) \qquad (6.14)$$

where, $\mathbf{0}$ is the momentum vector (by definition identical to the zero vector). Using the canonical form for a Lorentz boost out of the centre-of-mass system to an effective lab

frame[18],

$$p^{\mu}_{\text{LAB}} = \Lambda^{\mu}_{\nu}(-\boldsymbol{\beta}_z, \mathbf{0}, \mathbf{0})p^{\nu} \tag{6.15}$$

where $\Lambda^{\mu}_{\nu}(-\boldsymbol{\beta}_z, \mathbf{0}, \mathbf{0})$ is the Lorentz transformation matrix of a boost along the z-axis, which takes the form,

$$\begin{pmatrix} \gamma & \beta\gamma & 0 & 0 \\ \beta\gamma & \gamma & 0 & 0 \\ 0 & 0 & 1 & 0 \\ 0 & 0 & 0 & 1 \end{pmatrix} \tag{6.16}$$

The symbol γ is defined as $\gamma = 1/\sqrt{1-\beta^2}$. Using the beam configuration as defined in the lab frame of the *BABAR* detector produces the explicit form, $p^{\mu}_{\text{LAB}} = (E, \mathbf{p}_z, 0, 0)$ which is the sum the electron and positron beams[19] while E_+ is the energy of the high energy electron-beam and E_- is the energy of the low energy positron-beam. The sum of the electron and positron beams four-momenta is just, $p^{\mu}_{\text{LAB}} = (E_+ + E_-, \mathbf{E}_+ - \mathbf{E}_-, \mathbf{0}, \mathbf{0})$. Going through a few steps of algebra,

$$E_{\pm} = \frac{\gamma}{2}(\mathrm{M}_{\Upsilon(\mathbf{n}\mathrm{S})} \pm \beta\mathrm{M}_{\Upsilon(\mathbf{n}\mathrm{S})}) \tag{6.17}$$

this can be rewritten as

$$E_+ = \frac{\mathrm{M}_{\Upsilon(\mathbf{n}\mathrm{S})}}{2} \frac{\sqrt{1+\beta}}{\sqrt{1-\beta}} \tag{6.18}$$

and

$$E_- = \frac{\mathrm{M}_{\Upsilon(\mathbf{n}\mathrm{S})}}{2} \frac{\sqrt{1-\beta}}{\sqrt{1+\beta}} \tag{6.19}$$

The missing momentum is calculated by subtracting the measured event momentum from the estimated total initial momentum (this particular quantity can be calculated in either

---

[18]The boost components in the x, y directions are much smaller than in the z direction and can be ignored to first order.

[19]Which can be treated as $(E_+, \mathbf{E}_+, \mathbf{0}, \mathbf{0})$ and $(E_-, -\mathbf{E}_-, \mathbf{0}, \mathbf{0})$, where the electron mass has been ignored ($m_e \ll E_-$ and $m_e \ll E_+$)

the centre-of-mass or the laboratory frame).

$$p^{\mu}_{\text{missing, LAB}} = p^{\mu}_{\text{LAB}} - \sum_{\text{tracks}} p^{\mu}_{\text{LAB}} - \sum_{\text{neutrals}} p^{\mu}_{\text{LAB}} \qquad (6.20)$$

and

$$p^{\mu}_{\text{missing, CM}} = p^{\mu}_{\text{CM}} - \sum_{\text{tracks}} p^{\mu}_{\text{CM}} - \sum_{\text{neutrals}} p^{\mu}_{\text{CM}} \qquad (6.21)$$

The missing cosine of the polar angle, which will be denoted $\cos\not{\theta}$, is estimated using the missing momentum of the total event. Suppose the missing momentum is given as, $(\text{E}_{\text{miss}}, \text{p}_{\text{miss}})$, then the missing cosine of the polar angle would be defined as

$$\cos\not{\theta} = \text{p}_z/|\mathbf{p}|. \qquad (6.22)$$

Using the default boost and the known mass of the $\Upsilon(3S)$ a distinct difference can be observed between data and simulated events (MC). Since the boost vectors are known for the MC events, the information in the CM frame is correct (by construction). Further, the dominant boost parameter is β_z (pointing in the direction of the electron beam). Fixing β_x and β_y values and letting the β_z value vary over a small range near the default point, the measured boost in the z direction can be used to minimize the difference between the data and the MC distributions of $\cos\not{\theta}$, using a simple χ^2 (or quality factor statistic).

Figures 6.1 and 6.2 show the $\cos\not{\theta}$ distributions for different β_z values. The black points represent measured data boost, the yellow distributions represent the MC ($e^+e^- \to \mu^+\mu^-$) and the sand colour distributions represent $e^+e^- \to \Upsilon(3S) \to \mu^+\mu^-$. From these plots it can be shown how changes in the data boost (β_z) effect the $\cos\not{\theta}$ distribution and enable improved agreement between the data and MC distributions. For example, in Figure 6.1(a) and Figure 6.2(d) there is disagreement between data and MC histograms.

(a) $\beta_z = 0.46620$ (b) $\beta_z = 0.46700$

(c) $\beta_z = 0.46750$ (d) $\beta_z = 0.46755$
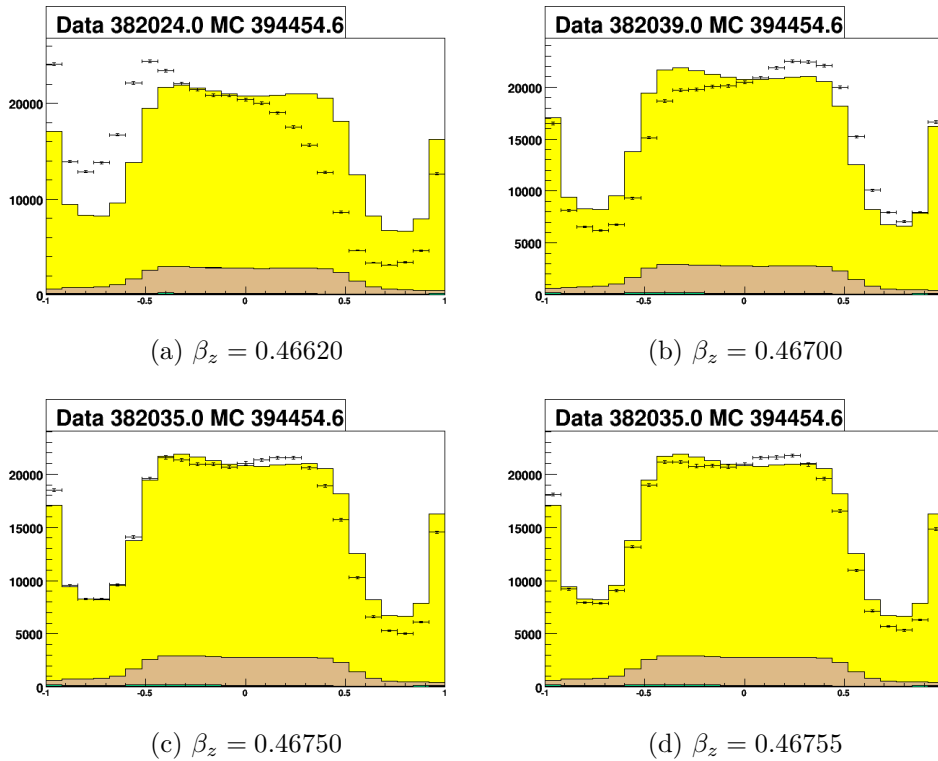
Figure 6.1: Missing cosine of the polar angle distributions for the fixed β_x (= -0.009565) and β_y (= -0.000603) and different β_z values indicated in each of the individual plots.

The quality factor defined as

$$\mathbf{QF}(\mathrm{D}, \mathrm{MC}) = \sum_i \frac{(\mathrm{D}_i - (\mathrm{MC})_i)^2}{\sigma_{\mathrm{D}_i}^2 + \sigma_{\mathrm{MC}_i}^2} \tag{6.23}$$

where D is a data histogram , MC is the total summed Monte Carlo histogram with identical binning as data, D_i and MC_i are the bin entries of the data and Monte Carlo histograms, and σ_i is the bin estimated resolution (calculated using the associated Poisson statistical error). The strong peaks in the $\cos(\not\phi)$ at -1 and 1 are due to initial state radiation. In the case of initial state radiation the emitted photon is preferentially emitted collinear with the direction of motion of either the electron or the positron which probably escapes detection down the beam pipe. In order to avoid trying to match these associated peaks (which are difficult to simulate properly and should also correspond to a lower centre-of-mass energy of produced dimuons), the minimization procedure is restricted to between -0.7 and 0.7.

(a) $\beta_z = 0.46770$ (b) $\beta_z = 0.46775$

(c) $\beta_z = 0.46780$ (d) $\beta_z = 0.46820$
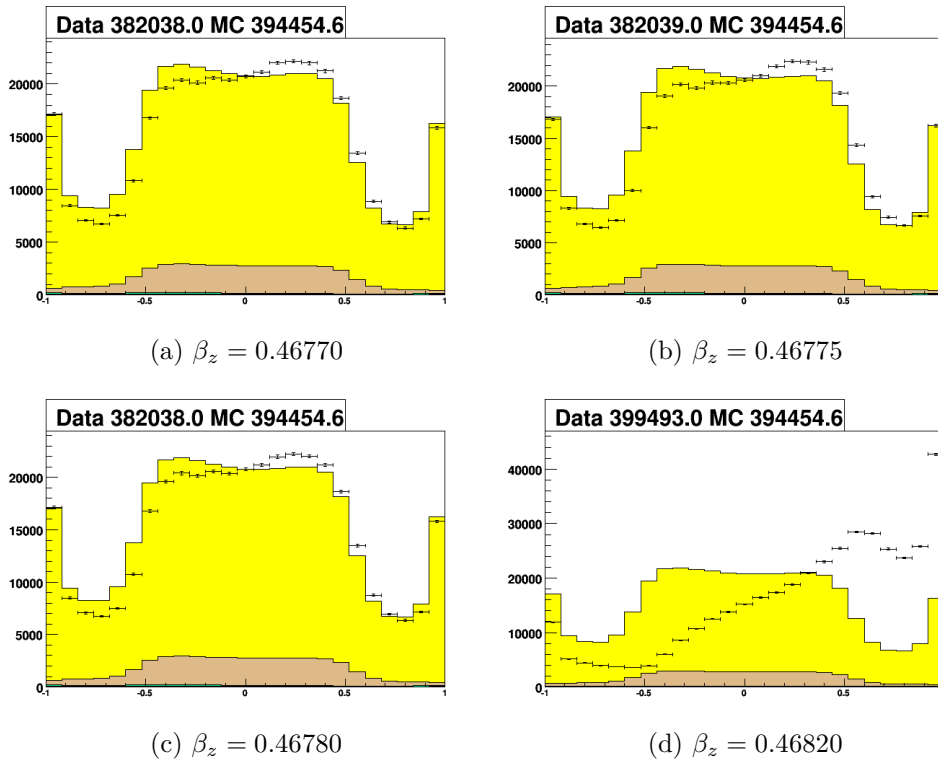
Figure 6.2: Missing cosine of the polar angle distributions for the fixed β_x (= -0.009565) and β_y (= -0.000603) and different β_z values indicated in each of the individual plots.

The objective is to arrive at the minimum β_z value for each set of QF, achieved using a quadratic fitting function (qff) relative to QF values in the minimum ranges of β_z(e.g. 0.4660 to 0.4680):

$$\mathbf{qff}(x) = ax^2 + bx + c \tag{6.24}$$

Figures 6.3, Figures 6.4 and Figures 6.5 shows the $\mathbf{qff}$(x) results for different sets of measurement, which are reported in the Table 6.14.

Measured Boost Vectors for $\Upsilon(3S)$

Boost vectors for $\Upsilon(3S)$ on-peak data are shown in the Table 6.15. Since β_z is the dominant term and corresponds to the beam direction, it can be corrected with respect to the default the accelerator values (also known as PepCond or PEP-II Conditions). Using measured boost vectors it is possible to estimate the energy of LER and HER beams. The LER beam

(a)

(b)
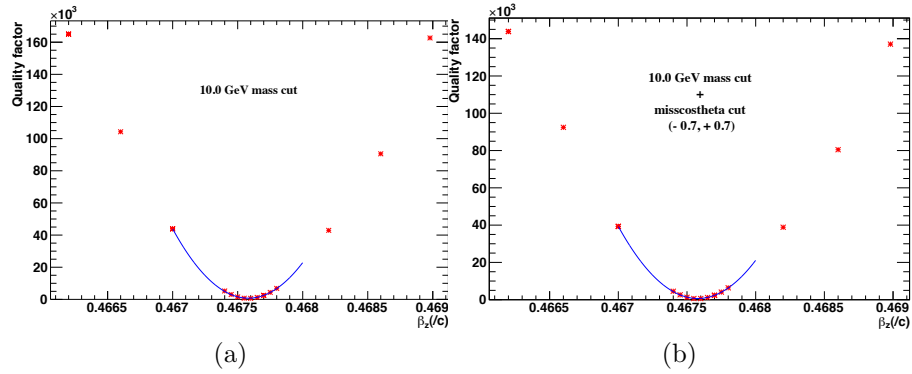
Figure 6.3: Quadratic fitting for the QF values in (a) 10.0 GeV/c^2 mass cut and (b) 10.0 GeV/c^2 plus $|\cos\theta|$ cuts.

(a)

(b)
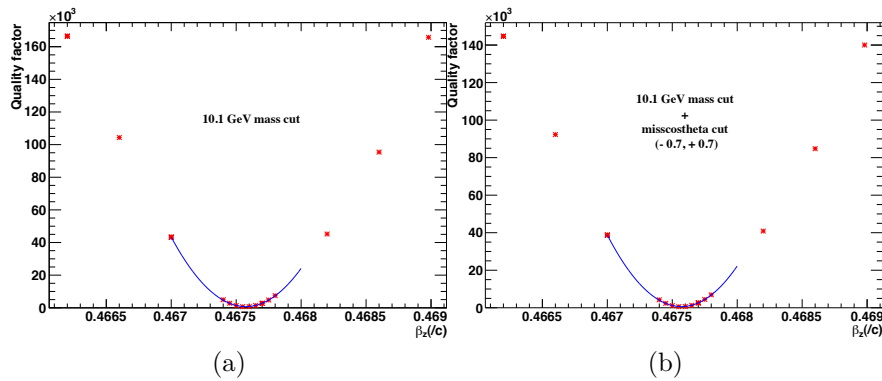
Figure 6.4: Quadratic fitting for the QF values in (a) 10.1 GeV/c^2 mass cut and (b) 10.1 GeV/c^2 with $|\cos\theta|$ cut.

(a)

(b)
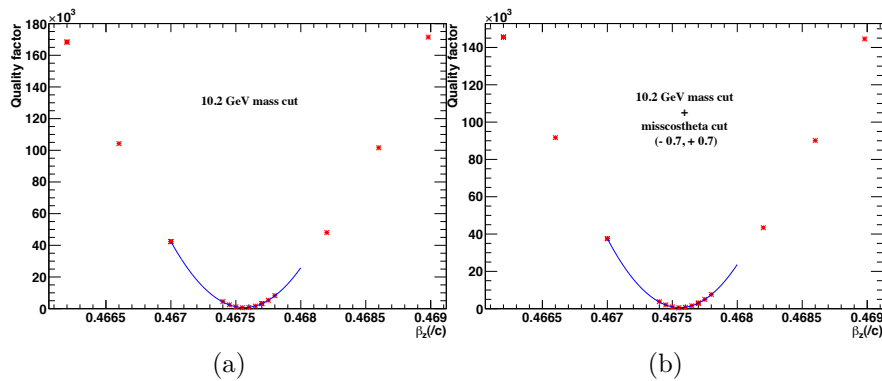
Figure 6.5: Quadratic fitting for the QF values in (a) 10.2 GeV/c^2 mass cut and (b) 10.2 GeV/c^2 with $|\cos\theta|$ cuts.

Table 6.14: Minimum β_z for different cuts from the quadratic fitting function.

Cuts	β_z
10.0 GeV/c^2	0.4675825
10.0 GeV/c^2 + $|\cos\theta|$	0.4675786
10.1 GeV/c^2	0.4675741
10.1 GeV/c^2 + $|\cos\theta|$	0.4675704
10.2 GeV/c^2	0.4675628
10.2 GeV/c^2 + $|\cos\theta|$	0.4675584

Boost Vector	$\Upsilon(3S)$
β_x	-0.009565
β_y	-0.000603
β_z	0.467570

Table 6.15: Final boost vector values for $\Upsilon(3S)$

energy is estimated at 7 MeV higher (than originally estimated) and the HER energy is at 18 MeV lower than the PepCond (machine condition) value for $\Upsilon(3S)$ resonance.

These measured values can be used to correct the data boost. The systematic error is determined by varying the boost away from the fitted minimum and calculating the systematic shift due to the small perturbation.

Measured Boost Vectors for $\Upsilon(4S)$

Using the same technique, but with the data sample divided into 1263 files (each file has roughly similar statistical significance). Each of the sub-samples is minimized independently (and the each minimum is calculated and plotted within the histogram, Figure 6.6). This technique was also used over the $\Upsilon(3S)$ data samples and the results are shown in Figure 6.7 (`low`), Figure 6.8 (`high`), and Figure 6.9 (`med`).

Using earlier equations (Equation 6.18 and Equation 6.19), combined with the mean $\beta_z = 0.484632$ and the initial estimate of the polar angle (θ) of the beam with respect to the

Mean	0.4846316
RMS (σ)	0.0000554
Error on Mean	0.0000016

Table 6.16: Distribution of β_z for $\Upsilon(4S)$ Relevant Parameters.

laboratory coordinate system, $\theta \approx 0.0200754$,[20] the energy of the electron beam is found to be $E_+ = 8.97783 \pm 0.0013$ GeV and $E_- = 3.11573 \pm 0.0005$ GeV. This is in contrast to the original beam energies of $E_+^{\text{default}} = 8.98872$ GeV and $E_-^{\text{default}} = 3.11195$ GeV (which have an estimated error on the total energy of 4 MeV). The beam energies shift by -10.9 MeV for the electron beam and 3.8 MeV for the positron beam.

The spread of the β_z distribution yields a measure of overall beam spread. Using the standard deviation (see Table 6.16) as a measure of overall beam spread, setting $\beta_z = 0.484632 \pm 0.000055$ and the electron beam has a spread of roughly 1.3 MeV and the positron beam has a spread of 0.5 MeV (note: using this methodology, the spread between the electron beam and the positron beam should be 100 % anti-correlated). The results for $\Upsilon(4S)$ and $\Upsilon(3S)$ using the sub-sample minimization are documented in Table 6.19, Table 6.20 and Table 6.21. The beam energies are *linear* with respect to initial mass (thus a shift of 4 MeV in initial mass corresponds almost with a shift of roughly 4 MeV. For example, the higher energy beam (using the parameters from $\Upsilon(3S)$ `med` in Table 6.20), the shift is 8.5867 to 8.590 (so slightly less than 4 MeV); similarly a downward shift corresponds to a shift from 8.5867 to 8.5834. The low energy beam seems a shift from 3.12197 to 3.12318 (upward shift roughly 1 MeV) and 3.12197 to 3.12077 (downward shift of about 1 MeV).

6.6 Theoretical Cross Section

Theoretical cross sections are obtained using Monte Carlo event generators. The generators are run in the `GeneatorsQA` framework. Beam parameters can be specified for the vari-

---

[20]The initial beam parameters are shown in Table 6.17 and Table 6.18.

Resonance	$\sqrt{s}$ (GeV)	$E_+ + E_-$ (GeV)	θ_{initial}	ϕ_{initial}	$\mathbf{p}$ (GeV/c)
$\Upsilon(4S)$	10.577799	12.100668	0.0200754	-3.095611	5.8767623
$\Upsilon(3S)$	10.355176	11.726650	0.0206862	-3.096473	5.5031499
$\Upsilon(2S)$	10.023260	11.183232	0.0208063	-3.082764	4.9597320
$\Upsilon(4S)$ - 0.030 GeV	10.538588	12.033790	0.0206146	-3.102576	5.8094968
$\Upsilon(3S)$ - 0.030 GeV	10.326467	11.678950	0.0204237	-3.089782	5.4554500
$\Upsilon(2S)$ - 0.030 GeV	9.993237	11.134949	0.0202538	-3.089381	4.9114499

Table 6.17: Initial parameters colliding beam parameters.

Resonance	$\sqrt{s}$ (GeV)	E_+ (GeV)	E_- (GeV)	β
$\Upsilon(4S)$	10.577799	8.98871515	3.11195285	0.48565602
$\Upsilon(3S)$	10.355176	8.61489995	3.11175005	0.46928576
$\Upsilon(2S)$	10.023260	8.071482	3.111734	0.44349719
$\Upsilon(4S)$ - 0.030 GeV	10.538588	8.9216434	3.1121466	0.48276546
$\Upsilon(3S)$ - 0.030 GeV	10.326467	8.5672	3.11175	0.46711819
$\Upsilon(2S)$ - 0.030 GeV	9.9932365	8.02319495	3.11174505	0.44108418

Table 6.18: Initial individual beam parameters.

Resonance	$\sqrt{s}$ (GeV)	$E_+ + E_-$ (GeV)
$\Upsilon(4S)$	10.577799	12.0936 ± 0.0009
$\Upsilon(3S)$ `low`	10.355176	11.7104 ± 0.0012
$\Upsilon(3S)$ `med`	10.355176	11.7093 ± 0.0016
$\Upsilon(3S)$ `high`	10.355176	11.7082 ± 0.0012

Table 6.19: Estimated beam parameters using minimization of small sub-samples ($E_+ + E_-$).

Resonance	$\sqrt{s}$ (GeV)	E_+ (GeV)	E_-	β
$\Upsilon(4S)$	10.577799	8.97668 ± 0.00088	3.11613 ± 0.00031	0.484632 ± 0.000055
$\Upsilon(3S)$ `low`	10.355176	8.5883 ± 0.0015	3.12208 ± 0.00056	0.46687 ± 0.00013
$\Upsilon(3S)$ `med`	10.355176	8.5867 ± 0.0023	3.12260 ± 0.00084	0.46672 ± 0.00020
$\Upsilon(3S)$ `high`	10.355176	8.5850 ± 0.0016	3.12321 ± 0.00057	0.46657 ± 0.00013

Table 6.20: Estimated beam parameters using minimization of small sub-samples (E_+, E_-, and β).
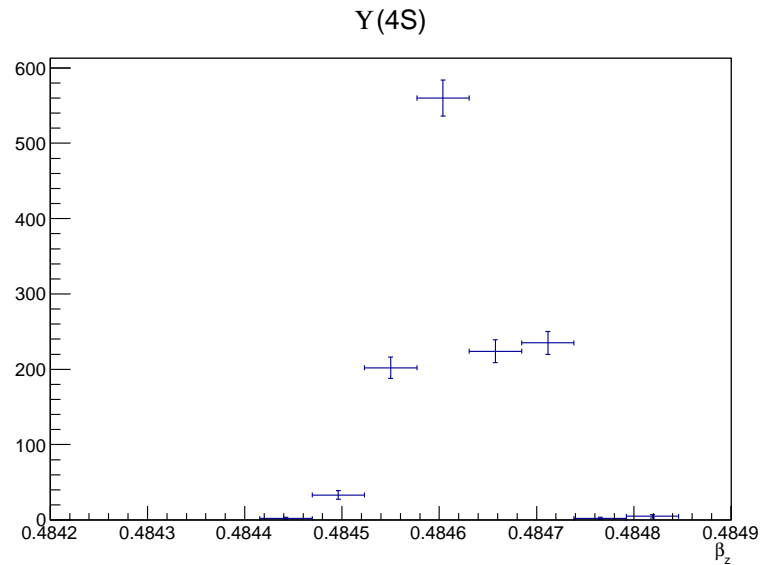
Figure 6.6: The χ^2 minimum as found through β_z minimizer for the entire $\Upsilon(4S)$ `Run 6` data set. The data set was divided into small sub-samples (1263) and each of the sub-samples were minimized independently.
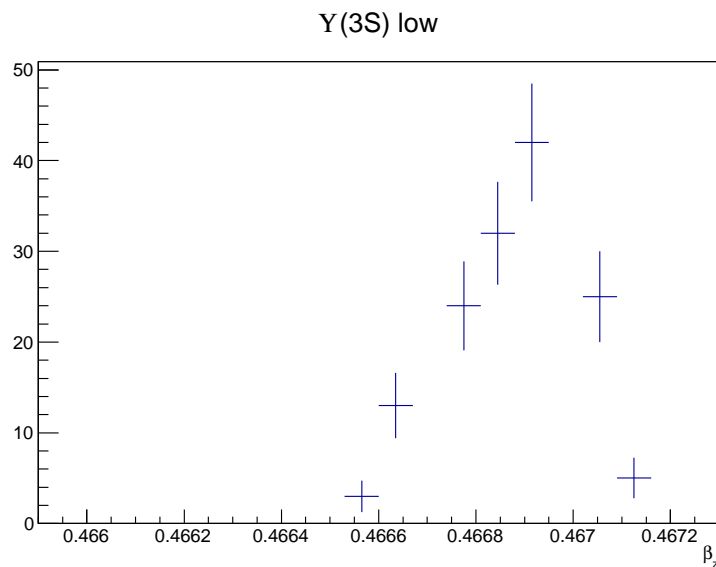
Figure 6.7: The χ^2 minimum as found through β_z minimizer for the entire $\Upsilon(3S)$ `Run 7 low` data set. The data set was divided into small sub-samples (144) and each of the sub-samples were minimized independently.
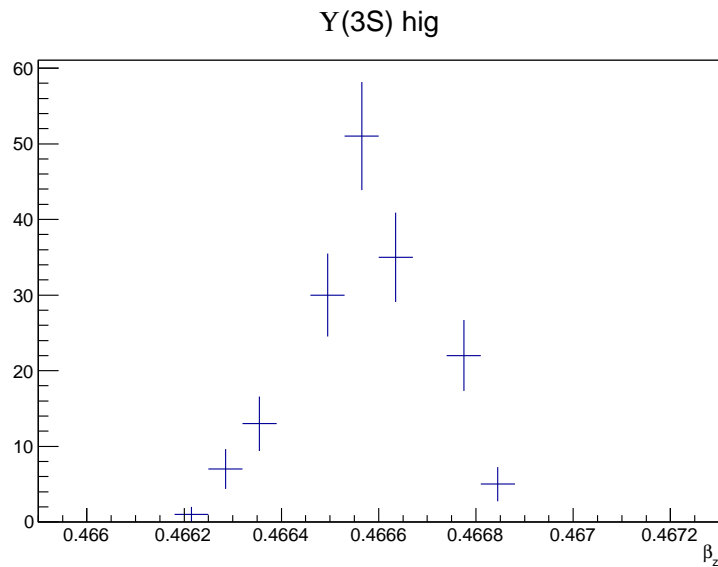
Figure 6.8: The χ^2 minimum as found through β_z minimizer for the entire $\Upsilon(3S)$ `Run 7 high` data set. The data set was divided into small sub-samples (163) and each of the sub-samples were minimized independently.
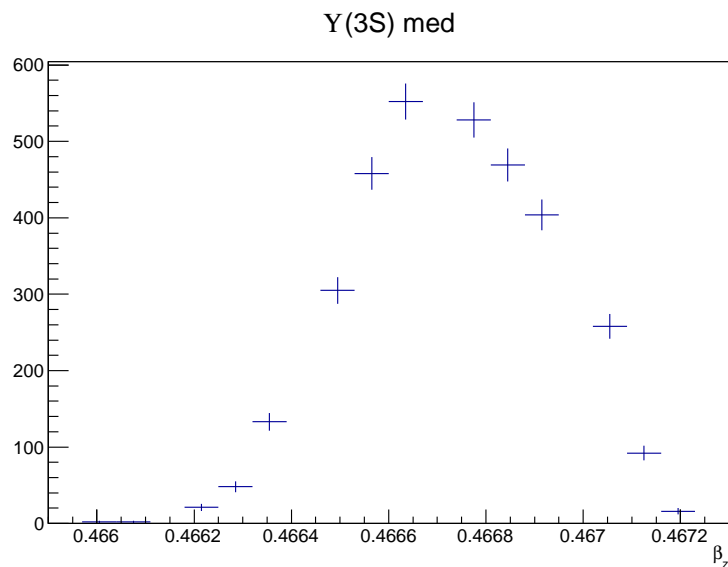
Figure 6.9: The minimum of as found through β_z minimizer for the entire $\Upsilon(3S)$ `Run 7 med` data set. The data set was divided into small sub-samples (3287) and each of the sub-samples were minimized independently.

Resonance	$\sqrt{s}$ (GeV)	$\delta(E_+ + E_-)$ (MeV)	$\delta(E_+)$ (MeV)	$\delta(E_-)$ (MeV)
$\Upsilon(4S)$	10.577799	7.1	12.0	-4.1
$\Upsilon(3S)$ `low`	10.355176	16.3	26.6	-10.3
$\Upsilon(3S)$ `med`	10.355176	17.4	28.2	-10.8
$\Upsilon(3S)$ `high`	10.355176	18.5	29.9	-11.4

Table 6.21: Estimated shifts using sub samples. Samples size: $\Upsilon(3S)$ `low` (144); $\Upsilon(3S)$ `high` (163); $\Upsilon(3S)$ `med` (3287); $\Upsilon(4S)$ (1263). The shift in the high energy beam is towards zero and in the opposite direction for the positron beam (an increase in energy).

ous resonances. The statistical contribution to uncertainty is negligible compared with the estimated systematic one.

The initial systematic uncertainty for each mode arises from the theoretical cross section[21] in the relevant region of phase space. In prior analyses [59–62][22] (in this case BAD 1850), the assigned uncertainties were 0.5 % for e^+e^-, 1.4 % for $\mu^+\mu^-$ and 2.0 % for $\gamma\gamma$. These values date back to 2001 [63]. The e^+e^- and $\mu^+\mu^-$ uncertainties were conservatively based comparisons between the generators in use then and alternative generators, while the $\gamma\gamma$ number was slightly inflated from a value `CLEO` used for the same generator.

A newer Bhabha generator, `BABAYAGA` [64, 65] was used by the *BABAR* collaboration. It implements a *new* next-to-leading order (NLO) Bhabha computation [66]. Using this generator Balossini and his collaborators claim an accuracy on the order of 0.1 %. Comparing the cross section reported by `BABAYAGA` to that reported by `BHWIDE`[23], the ratio of `BHWIDE` to `BABAYAGA` cross sections is 1.0016 ± 0.0011, where the error is the sum in quadrature of the reported theoretical errors. The deviation from unity is an additional systematic relative error (0.16 %). Adding this in quadrature to a 0.1 % relative error on `BABAYAGA` for a total relative error of 0.2 %. This term appears as a scaling factor for estimating the number Bhabha events which contaminate the final τ- and μ-pair event samples. The estimated

---

[21]This is equivalent to the size of the estimated error due to the Monte Carlo generator

[22]BAD 1312; BAD 1850; BAD 2126; BAD 2069;

[23]A slightly older Bhabha generator.

background due to Bhabha events has a dominant error associated with selection efficiency (see Table 6.22 and Table 6.24). The systematic error due to the Bhabha cross section can be ignored (and similarly the cross section due to other continuum background can be ignored because the selection efficiency for these background modes dominates the overall error).

Selection	Background Type	Estimated Background	Relative uncertainty
Dimuon ($\Upsilon(4S)$)	Bhabhas	1330 ± 180	1.4 %
Dimuon ($\Upsilon(3S)$)	Bhabhas	103.1 ± 4.2	4.1 %
τ ($\Upsilon(4S)$)	Bhabhas	52400 ± 1100	2.1 %
τ ($\Upsilon(3S)$)	Bhabhas	1452 ± 16	1.1 %

Table 6.22: The estimated contamination of Bhabha events in the dimuon and τ-pair selection, where the uncertainty is entirely due to the estimated selection efficiency.

6.7 τ- and μ-pair Cross Section Systematic

With respect to the production cross section ratio between the τ- and μ-pairs, Banerjee and collaborators [18] report an uncertainty of 0.44 %. In addition, Banerjee *et. al.* conclude that there is large correlation between individual theoretical errors. Within [18], the following errors are listed and their contribution on the final theoretical error estimated:

- Treatment of Vacuum Polarization - 0.22 %

- Initial and Final State Bremsstrahlung - 0.20 %

- Interference Effects - 0.04 %

- Pair-production and vertex correction uncertainty - 0.15 %

- Resonances - 0.28 %

The ratio between identical lepton pairs, for example $\sigma_{\tau\tau}(\sqrt{s_0})/\sigma_{\tau\tau}(\sqrt{s_1})$, should have a smaller theoretical error than the ratio between different lepton generations (a large number of the associated differences between the dimuon production cross sections and the τ-pair
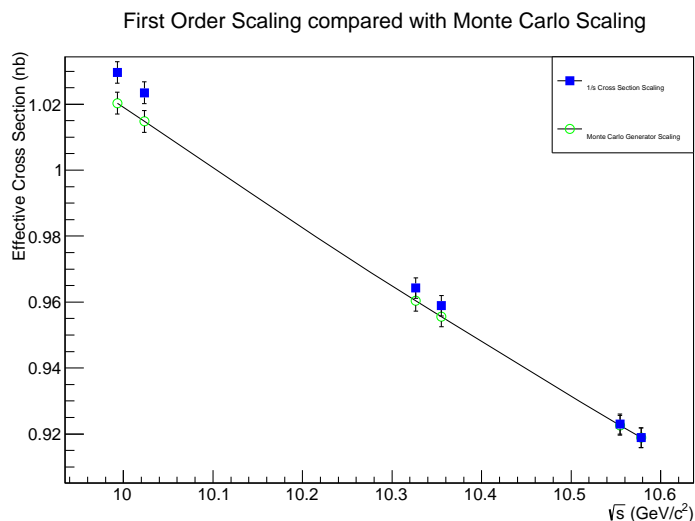
Figure 6.10: The $e^+e^- \to \tau\tau$ cross section scales roughly as $1/s$. The next order correction should be on the order $(m_\tau/\sqrt{s})^4$.

production cross sections are due to the mass of the τ lepton being considerably larger than the muon). Using the ultra-relativistic assumption (that the cross section scales as $1/s$), the τ cross section has one-σ discrepancy when compared to the Monte Carlo scaling[24]. In the case of dimuons, the cross section scaling has a 0.5σ discrepancy (from $1/s$).

Since the scaling of the individual lepton pair cross sections is reasonably described by $1/s$ (see Figure 6.10 and 6.11), an estimate of the overall systematic uncertainty due to the ratio of τ- or μ-lepton cross sections at different centre-of-mass energies can be estimated using variations of the beam energy scale. If the beam energies were scaled by 4 MeV up or down independently the following ratio:

$$\frac{\sqrt{s_0} + \delta s_0}{\sqrt{s_1} + \delta s_1} \tag{6.25}$$

---

[24]This can be seen,

$$0.9189 \pm 0.0021 \,\text{nb} \times (10.5782 \pm 0.0025 \,\text{GeV}/10.3552 \pm 0.0025 \,\text{GeV})^2 \quad = \quad (0.9189 \pm 0.0021 \,\text{nb}) \times (1.04354 \pm 0.00071)$$
$$= \quad (0.9589 \pm 0.0024 \,\text{nb})$$

and then
$$|0.9589 - 0.9556|/0.0024 = 1.038,$$

which is a 1σ discrepancy.
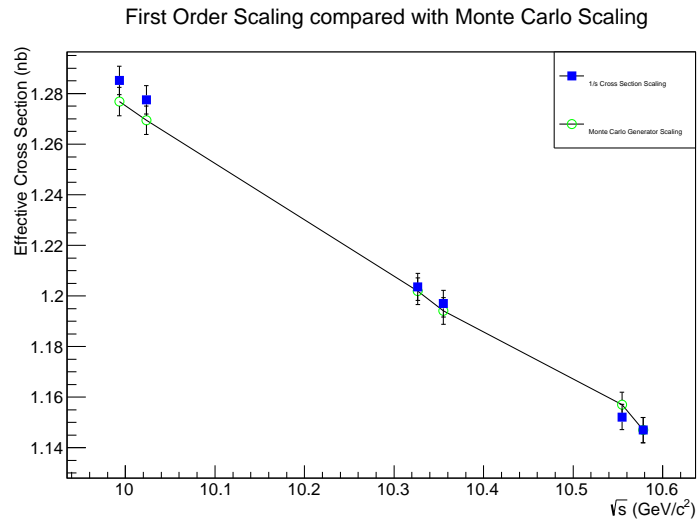
Figure 6.11: The $e^+e^- \to \mu\mu$ cross section scales roughly as $1/s$. The next order correction is on the order of $(m_\mu/\sqrt{s})^4$. There is better agreement between $1/s$ scaling when considering dimuon cross section when compared to τ pair cross section (see Figure 6.10).
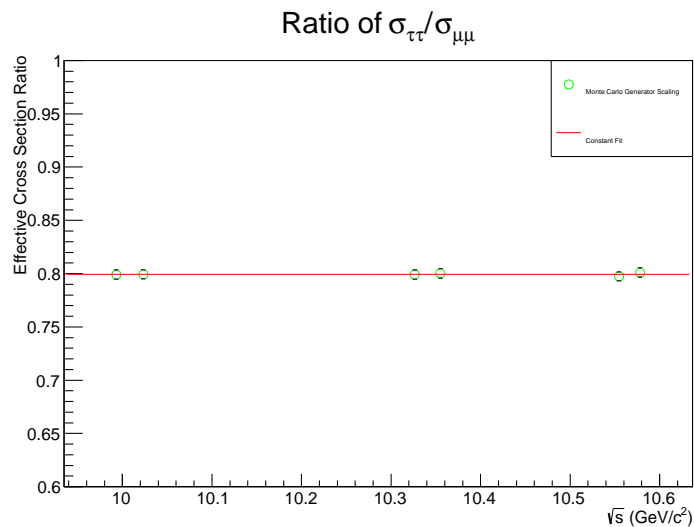
Figure 6.12: Assuming lepton universality (electromagnetic) and then the τ pair production cross section divided by dimuon production cross section should be flat[25] (the cross sections are found using KK2F Monte Carlo generator), fit is a constant (0.7994 ± 0.0018), with the associated error bar given by the quadratic sum of estimated cross section errors (all errors treated as independent), the simple fit has $\chi^2/\text{DOF} = 0.42055/5$; which is equivalent to a fit probability ($\mathbf{p} = 0.995$).

provides an estimate of the maximal variation of the cross section ratio. This would shift the overall cross section ratio by 0.04 %, and lead to a maximal shift of 0.2 % on $\mathcal{R}_{\tau/\mu}$ (the τ-and μ-lepton cross section ratio would have independent and uncorrelated errors)[26].

6.8 Projected Sensitivity

Using the early and late unblind periods, plus the $\Upsilon(3S)$ off-peak data will yield an estimate of the statistical sensitivity. The statistical component on the $\mathcal{R}_{\tau/\mu}$ of τ, μ on-peak and μ off-peak are shown in Table 6.23. Scaling the amount of on-peak data by a factor of $\mathcal{L}_{\text{unblind}}/\mathcal{L}_{\text{blind}}$, the statistical sensitivity should be scaled by $\sqrt{2.408/25.557} = 1/\sqrt{10.61}$. The number of dimuons selected is around 100 times larger than the τ pair sample. The number of τ events selected should be the dominant statistical error on the ratio. The statistical error due to τ pairs is roughly 3.3 % when considering the `low` and `high` data sets in the case of $[e\not{\phi}]$, hence the projected sensitivity should be about 1.0 % (the additional statistical component due to the τ-pair events at $\sqrt{s} = 10.58$ GeV used for subtraction). The dimuons statistical error of 0.88 % would be scaled by the same factor, and the estimated statistical contribution to the overall error would be 0.27 % (there is also an additional contribution of 0.15 % due to the μ-pair events at $\sqrt{s} = 10.58$ GeV used for subtraction).

Decreasing the size of the statistical error associated with the off-peak data set by using a large sample of $\Upsilon(4S)$ on or off-peak data should be possible. Currently the projected sensitivity is about 0.50-0.60 %. For example with `Run 6` (from the 2007 data collection period) $\Upsilon(4S)$ off-peak data sample (7.8 fb^{-1}) the statistical component would be on the order of 0.30-0.35 %. On the other hand using all `Run 6` $\Upsilon(4S)$ on-peak data (78 fb^{-1}) for the off-peak terms, the statistical component would be on the order of 0.09-0.11 %. The luminosity can be been assigned a flat 0.5 % error (uncorrelated). Combining all of the

---

[26]In addition, in Figure 6.12, the scaling between the dimuons and τ cross sections appears to be fit well by a constant. It also appears, that `KK2F` use a very similar distribution to generate the estimated cross section for both the τ- and μ-pairs.

	$\mathcal{R}_{\tau/\mu}$	$\mathcal{B}(\Upsilon(3S) \to \tau^+\tau^-)$	$\mathcal{B}(\Upsilon(3S) \to \mu^+\mu^-)$	$\sigma_{\tau^+\tau^-}/\sigma_{\mu^+\mu^-}$
Principal Value	1.04772	0.0276052	0.0263479	0.807734
τ Statistical ($\sqrt{s} = m_{\Upsilon(3S)}$)	0.033	0.00089	—	—
τ Statistical ($\sqrt{s} = m_{\Upsilon(4S)}$)	0.0057	0.00015	—	0.00060
μ Statistical ($\sqrt{s} = m_{\Upsilon(3S)}$)	0.0092	—	0.00023	—
μ Statistical ($\sqrt{s} = m_{\Upsilon(4S)}$)	0.0016	—	0.000040	0.00016
$\sigma_{\sigma_{\Upsilon(3S)}}$	0.00031	0.00028	0.00028	—
$\sigma_{\sigma_{\tau\tau}}(\sqrt{s} = m_{\Upsilon(4S)})$	0.019	0.00053	< 0.00001	0.0000074
$\sigma_{\sigma_{\tau\tau}}(\sqrt{s} = m_{\Upsilon(3S)})$	0.019	0.00053	< 0.00001	—
$\sigma_{\sigma_{\mu\mu}}(\sqrt{s} = m_{\Upsilon(4S)})$	0.019	< 0.00001	0.00051	0.000000061
$\sigma_{\sigma_{\mu\mu}}(\sqrt{s} = m_{\Upsilon(3S)})$	0.019	< 0.00001	0.00051	—
$\sigma_{\mathcal{L}_{\mathrm{on}}}$	0.00016	0.0013	0.0012	—
$\sigma_{\mathcal{L}_{\mathrm{off}}}$	0.00051	0.0011	0.0010	0.00010
$\sigma_{\varepsilon_{\tau\tau}}(\sqrt{s} = m_{\Upsilon(4S)})$	0.0040	0.00011	—	0.00042
$\sigma_{\varepsilon_{\tau\tau}(\mathrm{QED})}(\sqrt{s} = m_{\Upsilon(3S)})$	0.0060	0.00016	—	—
$\sigma_{\varepsilon_{\Upsilon(3S)\to\tau\tau}}$	0.0026	0.000067	—	—
$\sigma_{\varepsilon_{\mu\mu}}(\sqrt{s} = m_{\Upsilon(4S)})$	0.0013	—	0.000033	0.00013
$\sigma_{\varepsilon_{\mu\mu}(\mathrm{QED})}(\sqrt{s} = m_{\Upsilon(3S)})$	0.0013	—	0.000034	—
$\sigma_{\varepsilon_{\Upsilon(3S)\to\mu\mu}}$	0.00070	—	0.000018	—
Statistical Error	0.035	0.00090	0.00023	0.00062
Relative Uncertainty	3.3 %	3.3 %	0.89 %	0.077 %
MC Statistical Error	0.0079	0.00021	0.000051	0.00044
MC Relative Uncertainty	0.76 %	0.74 %	0.19 %	0.054 %

Table 6.23: Measured Value of the Branching Fractions and Ratio of Branching Fractions. This is using an updated cross section which is equivalent to the estimate the number of $\Upsilon(3S)$ produced for the combined `low` and `high` data samples ($4.355 \pm 0.032 \pm 0.026$ nb instead of (4.19 ± 0.19 nb)). [$e\not{e}$] (electron - not electron selection). These values are numerically simulated.

	$\mathcal{R}_{\tau/\mu}$	$\mathcal{B}(\Upsilon(3S)\to\tau^+\tau^-)$	$\mathcal{B}(\Upsilon(3S)\to\mu^+\mu^-)$	$\sigma_{\tau^+\tau^-}/\sigma_{\mu^+\mu^-}$
Principal Value	1.04772	0.0276052	0.0263479	0.807734
μ Background $(c\bar{c})$ $(\sqrt{s}=m_{\Upsilon(4S)})$	0.00000069	—	0.000000018	0.000000072
μ Background (uds) $(\sqrt{s}=m_{\Upsilon(4S)})$	0.000010	—	0.00000026	0.0000010
μ Background (τ) $(\sqrt{s}=m_{\Upsilon(4S)})$	0.000068	—	0.0000017	0.0000069
μ Background (e^+e^-) $(\sqrt{s}=m_{\Upsilon(4S)})$	0.000057	—	0.0000014	0.0000058
μ Background $(c\bar{c})$ $(\sqrt{s}=m_{\Upsilon(3S)})$	0.00000055	—	0.000000014	—
μ Background (uds) $(\sqrt{s}=m_{\Upsilon(3S)})$	0.000014	—	0.00000035	—
μ Background (τ) $(\sqrt{s}=m_{\Upsilon(3S)})$	0.00010	—	0.0000025	—
μ Background (e^+e^-) $(\sqrt{s}=m_{\Upsilon(3S)})$	0.000039	—	0.00000097	—
τ Background $(c\bar{c})$ $(\sqrt{s}=m_{\Upsilon(4S)})$	0.00011	0.0000028	—	0.000011
τ Background (uds) $(\sqrt{s}=m_{\Upsilon(4S)})$	0.000015	0.00000040	—	0.0000016
τ Background (μ) $(\sqrt{s}=m_{\Upsilon(4S)})$	0.000031	0.00000080	—	0.0000031
τ Background (e^+e^-) $(\sqrt{s}=m_{\Upsilon(4S)})$	0.0046	0.00012	—	0.000484607
τ Background $(c\bar{c})$ $(\sqrt{s}=m_{\Upsilon(3S)})$	0.00011	0.0000029	—	—
τ Background (uds) $(\sqrt{s}=m_{\Upsilon(3S)})$	0.000022	0.00000057	—	—
τ Background (μ) $(\sqrt{s}=m_{\Upsilon(3S)})$	0.000033	0.00000090	—	—
τ Background (e^+e^-) $(\sqrt{s}=m_{\Upsilon(3S)})$	0.0019	0.000051	—	—
τ Background $(\Upsilon(3S)$ Cascades$)$	0.00549834	0.000146632	—	—
μ Background $(\Upsilon(3S)$ Cascades$)$	0.00174166	—	0.000043	—
Background Total	0.0076	0.00020	0.000043	0.00048
Relative Uncertainty	0.73 %	0.71 %	0.16 %	0.6 %

Table 6.24: Measured Value of the Branching Fractions and Ratio of Branching Fractions (continued). This is using an updated $\Upsilon(3S)$ cross section which is equivalent to the estimate the number of $\Upsilon(3S)$ produced for the combined `low` and `high` data samples ($4.355\pm0.032\pm 0.026$ nb instead of $(4.19\pm0.19$ nb$)$). $[e\not{e}]$ (electron - not electron selection). All errors here are statistical estimates. These values are numerically simulated.

estimated systematic (see Table 6.30), the size of the total systematic error should be 1.3 %.

The τ-pair selection statistical error of 3.3 % on the $\mathcal{R}_{\tau/\mu}$ would imply a 1.1 % statistical error when considering the blind sample. Since the $\Upsilon(2S)$ has nearly the same QED cross section for τ-pair production, the τ statistical error can be estimated at 1.5 %.

6.9   Cross Check

Using the $\Upsilon(4S)$ data-set, the estimated cross section ratio provides a mechanism to check for a deviation between theory and experiment. Assuming lepton universality is valid with respect to QED interactions, the cross check provides another mechanism to estimate any missing systematic errors in $\mathcal{R}_{\tau/\mu}$ calculations.

The cross section ratio is estimated at 0.8012 ± 0.0044 (the *theoretical* estimate cross section ratio [18]). The cross section ratio is measured to $0.811385 \pm 0.00062 \pm 0.0078$ (or 0.8114 ± 0.0079) after correcting for effects of the τ lepton branching fraction. The significance of this deviance is 1.1σ (where all errors have been added in quadrature). In order to be conservative the relative size of the associated deviation will be taken as a global systematic on the $\mathcal{R}_{\tau/\mu}$. This leads to an additional systematic error (called the *CC-blind* systematic) which is assigned the value of 1.25 % (equal to the relative size of the deviation from the measured value).

6.9.1   Systematics Table

The estimated overall systematic of measurements are tabulated in Table 6.25, 6.26, 6.27, and 6.28. [27,28,29,30] Table 6.25 and Table 6.30 contain the estimates of all associated measurement uncertainties (and individual systematics).

---

[27]Using the results from [1].

[28]When there are 2 tracks per event and similar momentum the tracking efficiency systematic should cancel [67].

[29]Assumes that the cross section systematics are correlated between $\sigma_{\tau\tau}(\sqrt{s_0})/\sigma_{\tau\tau}(\sqrt{s_1})$.

[30]Luminosity systematic error should decrease as the data set is increased from unblind to the blind data sets.

Variable	Value (Shift $\delta\mathcal{R}$)
No Systematic	1.04772 (0)
Momentum Scale	1.04807 (+0.00035 or +0.033 %)
Momentum Angle	1.04773 (+0.00001 or +0.0001 %)
Momentum Resolution	1.04870 (+0.00098 or +0.094 %)
Energy Scale	1.04832 (+0.00060 or +0.057 %)
Energy Resolution	1.05092 (+0.00320 or +0.305 %)
Boost Shift (angle forward)	1.04834 (+0.00062 or +0.059 %)
Energy Resolution (CM shift)	1.04741 (-0.00031 or -0.030 %)
Beam Energy Scale	1.04765 (-0.00007 or -0.007 %)
Beam Energy Spread	1.04846 (+0.00074 or +0.070 %)
	Error
π^0 Veto Systematic	0.00057 (0.054 %)
PID Table (statistical)	0.00670 (0.64 %)
Total	1.0477 ± 0.0076 (0.726 %)

Table 6.25: Estimated size of systematic variation on $\mathcal{R}$.

Variable	Value (Shift $\delta\mathcal{B}(\Upsilon(3S) \to \tau\tau)$)
No Systematic	0.0276052 (0)
Momentum Scale	0.0276142 (+0.0000090 or +0.033 %)
Momentum Angle	0.0276068 (+0.0000016 or +0.006 %)
Momentum Resolution	0.0276313 (+0.0000261 or +0.095 %)
Energy Scale	0.0276391 (+0.0000339 or +0.123 %)
Energy Resolution	0.0276920 (+0.0000868 or +0.314 %)
Boost Shift (angle forward)	0.0275257 (-0.0000795 or -0.288 %)
Energy Resolution (CM shift)	0.0275972 (-0.0000080 or -0.029 %)
Beam Energy Scale	0.0276023 (-0.0000029 or -0.011 %)
Beam Energy Spread	0.0276235 (+0.0000183 or +0.066 %)
	Error
π^0 Veto Systematic	0.000014 (0.052 %)
PID Table (statistical)	0.000176 (0.64 %)
Total	0.02761 ± 0.00022 (0.79 %)

Table 6.26: Estimated size of systematic variation on $\mathcal{B}(\Upsilon(3S) \to \tau\tau)$

Variable	Value (Shift $\delta\mathcal{B}(\Upsilon(3S) \to \mu\mu)$)
No Systematic	0.0263479 (0)
Momentum Scale	0.0263477 (+0.0000002 or < 0.001 %)
Momentum Angle	0.0263493 (+0.0000014 or +0.005 %)
Momentum Resolution	0.0263482 (+0.0000004 or +0.001 %)
Energy Scale	0.0263652 (+0.0000173 or +0.066 %)
Energy Resolution	0.0263503 (+0.0000024 or +0.009 %)
Boost Shift (angle forward)	0.0262564 (-0.0000915 or -0.347 %)
Energy Resolution (CM shift)	0.0263480 (+0.0000001 or < 0.001 %)
Beam Energy Scale	0.0263470 (-0.0000009 or -0.003 %)
Beam Energy Spread	0.0263466 (-0.0000013 or -0.005 %)
	Error
π^0 Veto Systematic	0.0000040 (0.015 %)
PID Table (statistical)	—
Total	$0.026348 \pm 0.000093(0.354$ %)

Table 6.27: Estimated size of systematic variation on $\mathcal{B}(\Upsilon(3S) \to \mu\mu)$

Variable	Value (Shift $\delta(\sigma_{4S}^{\tau\tau}/\sigma_{4S}^{\tau\tau})$)
No Systematic	0.807734 (0)
Momentum Scale	0.807660 (-0.000074 or -0.009 %)
Momentum Angle	0.807758 (+0.000024 or +0.003 %)
Momentum Resolution	0.808597 (+0.000863 or +0.107 %)
Energy Scale	0.808160 (+0.000426 or +0.053 %)
Energy Resolution	0.808326 (+0.000592 or +0.073 %)
Boost Shift (angle forward)	0.808560 (+0.000826 or +0.102 %)
Energy Resolution (CM shift)	0.807757 (+0.000023 or +0.003 %)
Beam Energy Scale	0.808026 (+0.000292 or +0.036 %)
Beam Energy Spread	0.807726 (-0.000008 or < 0.001 %)
	Error
π^0 Veto Systematic	0.00044 (0.054 %)
PID Table (statistical)	0.000624 (0.077 %)
Total	$0.8077 \pm 0.0016(0.20$ %)

Table 6.28: Estimated size of systematic variation on Cross Section ratio ($\Upsilon(4S)$).

	$\mathcal{R}_{\tau/\mu}$	$\mathcal{B}(\Upsilon(3S) \to \tau^+\tau^-)$	$\mathcal{B}(\Upsilon(3S) \to \mu^+\mu^-)$	$\sigma_{\tau^+\tau^-}/\sigma_{\mu^+\mu^-}$
Principle Value	1.04772	0.0276052	0.0263479	0.807734
$\Upsilon(3S)$ Stat. Error	0.033	0.00089	0.00023	—
$\Upsilon(4S)$ Stat. Error	0.0059	0.00015	0.000040	0.00062
$\Upsilon(3S)$ MC Stat. Error	0.0067	0.00069	0.000038	0.00000
$\Upsilon(4S)$ MC Stat. Error	0.0042	0.00011	0.000033	0.00044
Cross Section Error	0.0029	0.000055	0.000053	—
Luminosity	0.00053	0.0017	0.0016	0.00010
PDG Branching Fraction	0.0035	0.000091	—	0.0022
Backgrounds	0.0076	0.00020	0.000043	0.00048
π^0 Veto Systematic	0.00057	0.000014	0.0000040	0.00044
Systematic Error	0.0076	0.000218	0.000093	0.0016
Total Statistical	0.034	0.00090	0.00023	0.00062
Relative Total Systematic	0.014	0.0018	0.0016	0.0078
CC-blind Systematic	1.25 %	—	—	—

Table 6.29: Total Statistical and Systematic Table. Currently calculated with completely uncorrelated errors. Does not include the scale correction for the PDG branching fraction error. The row, Systematic Error, is a reproduction of the values listed in Table 6.25, Table 6.26, Table 6.27 and 6.28.

	$\mathcal{R}_{\tau/\mu}$	$\mathcal{B}(\Upsilon(3S) \to \tau^+\tau^-)$	$\mathcal{B}(\Upsilon(3S) \to \mu^+\mu^-)$	$\sigma_{\tau^+\tau^-}/\sigma_{\mu^+\mu^-}$
Principle Value	1.03848	0.027362	0.0263479	0.811385
$\Upsilon(3S)$ Stat. Error	0.033	0.00089	0.00023	—
$\Upsilon(4S)$ Stat. Error	0.0059	0.00015	0.000040	0.00062
$\Upsilon(3S)$ MC Stat. Error	0.0067	0.00069	0.000038	—
$\Upsilon(4S)$ MC Stat. Error	0.0042	0.00011	0.000033	0.00044
Cross Section Error	0.0029	0.000055	0.000053	—
Luminosity	0.00053	0.0017	0.0016	0.00010
PDG Branching Fraction	0.0035	0.000091	—	0.0022
Backgrounds	0.0076	0.00020	0.000043	0.00048
π^0 Veto Systematic	0.00943	0.000248	0.000237	0.0073
Systematic Error	0.0079	0.000218	0.000093	0.0016
Total Statistical	0.034	0.00090	0.00023	0.00062
Total Systematic	0.014	0.0018	0.0016	0.0078
CC-blind Systematic	0.013 (1.25 %)	—	—	—

Table 6.30: Total Statistical and Systematic Table. Currently calculated with completely uncorrelated errors. Correction of Efficiency on $\Upsilon(3S) \to \tau\tau$ efficiency is 1.0089 ± 0.0033 and correction on τ QED efficiency is 0.9955 ± 0.0033 and has been applied; The CC-blind Systematic is listed independently of the Total Systematic.

6.10   Summary

The $\mathcal{R}_{\tau/\mu}$ is measured to be $1.0385 \pm 0.034(\text{stat}) \pm 0.014(\text{sysm}) \pm 0.013(\text{CC-blind})$ (the first error is error associated with data statistics, the second error is the systematic error and the third error is due to the $\Upsilon(4S)$ cross section ratio deviation). Averaging $\mathcal{R}_{\tau/\mu}$ $1.0385 \pm 0.034 \pm 0.014 \pm 0.013$ with the only previous measurement of $1.05 \pm 0.08 \pm 0.05$ [4,12], yields 1.044 ± 0.036 (where all errors are assumed to be uncorrelated).

The ratio of τ-pair to μ-pair production cross sections at $\sqrt{s} = m_{\Upsilon(4S)}$ is measured to be $0.8114 \pm 0.0006 \pm 0.0078$. The $\mathcal{B}(\Upsilon(3S) \to \mu^+\mu^-)$ is $0.02635 \pm 0.0002 \pm 0.0016$ and $\mathcal{B}(\Upsilon(3S) \to \tau^+\tau^-)$ is $0.0274 \pm 0.0009 \pm 0.0018$. The PDG gives a world average of 0.218 ± 0.0021. The most recent CLEO collaboration estimate of $\mathcal{B}(\Upsilon(3S) \to \mu^+\mu^-)$ is $0.0239 \pm 0.0007 \pm 0.0010$ [68] (this corresponds to a $1.7\,\sigma$ deviation from the world average and $1.2\,\sigma$ deviation from CLEO). In addition, assuming that lepton universality holds, the estimated total decay width of the $\Upsilon(3S)$ can be expressed as

$$\Gamma = \frac{\Gamma_{ee}\Gamma_{\text{hadrons}}/\Gamma}{\mathcal{B}_{\mu\mu}(1 - 3\mathcal{B}_{\mu\mu})}. \tag{6.26}$$

Combining the muonic branching fractions with the PDG estimated value of $\Gamma_{ee}\Gamma_{\text{hadrons}}/\Gamma$ $(0.414 \pm 0.007\,\text{keV}$ [12]$)$, gives a total decay width of the $\Upsilon(3S)$ resonance of $17.1 \pm 1.0\,\text{keV}$.

6.11   A Two Higgs Doublet Model Interpretation of Results

The Higgs boson has recently been observed by the ATLAS and CMS collaborations. There are extensions to the Standard Model (SM) with an extended Higgs sector (more than one Higgs boson). In extended Higgs models, there is still room for a light Higgs bosons [33]. The $\mathcal{R}_{\tau/\mu}$ provides an estimate of $\mathcal{B}(\Upsilon(3S) \to \gamma A^0)\mathcal{B}(A^0 \to \tau^+\tau^-)$. Starting with the measured $\mathcal{R}_{\tau/\mu} = 1.0385 \pm 0.034 \pm 0.014 \pm 0.013$, using the one-tailed Gaussian coverage, a 90 % confidence limit (upper limit) corresponds to $\mathcal{R}_{\tau/\mu} < 1.10$ and $\mathcal{B}(\Upsilon(3S) \to \gamma A^0)\mathcal{B}(A^0 \to$

$\tau^+\tau^-$) $< 2.6 \times 10^{-3}$ (at 90 % confidence). Further, assuming the Standard Model and the estimated reduction in statistical error due to the size of the blind sample, the 90 % upper confidence limit would be $\mathcal{B}(\Upsilon(3S) \to \gamma A^0)\mathcal{B}(A^0 \to \tau^+\tau^-) < 9.5 \times 10^{-4}$.

Using the upper bound, $\mathcal{R}^\star = \Gamma(\Upsilon((3S)) \to A^0\gamma)/\Gamma(\Upsilon(3S) \to \mu\mu) < 0.10$, this would yield an 90 % upper confidence limit of $\tan\beta < 16$ for the 50 MeV photon and $\tan\beta < 54$ for the 10 MeV photon.

There are a number of 2 Higgs Doublet Model (2HDM), including type I, type II, and type III (as well as specific lepton-specific models). The motivation for the measurement of the $\mathcal{R}_{\tau/\mu}$ is based on the 2HDM(type II) model with a low mass CP-odd Higgs boson. Starting with Equation 2.28 it follows that assuming the CP-odd Higgs decays 100 % to τ-pairs,

$$\mathcal{R}^\star = \mathcal{R}_{\tau/\mu} - 1 = 0.019318 \times \tan^2\beta \frac{\Delta(m)}{m_{\Upsilon(3S)}} \times \left[1 - \frac{\Delta(m)}{2m_{\Upsilon(3S)}}\right] \qquad (6.27)$$

where $\Delta(m) = m_{\Upsilon(3S)} - m_{A^0}$. Neglecting the term within the square brackets above, one gets the following limit on $\tan^2\beta$:

$$\tan^2\beta < (\mathcal{R}_{\tau/\mu} - 1) \times \frac{m_{\Upsilon(3S)}}{\Delta(m) \times 0.019318} \qquad (6.28)$$

or

$$\tan^2\beta < \frac{536.04 \text{ GeV}/c^2}{\Delta(m[\text{ GeV}/c^2])} \times (\mathcal{R}_{\tau/\mu} - 1) \qquad (6.29)$$

Thus, for smaller mass differences between the hypothetical CP-odd Higgs boson and $\Upsilon(3S)$, $\Delta(m[\text{ GeV}/c^2])$ (measured in GeV/c^2), there is a less stringent upper limit on $\tan\beta$. Starting with the measured $\mathcal{R}_{\tau/\mu}$ and hypothesizing a CP-odd Higgs boson with a mass 250 MeV/c^2 below the $\Upsilon(3S)$ mass, an upper limit on $\tan\beta < 14.6$ (at 90 % confidence). Assuming that the blind sample yields the Standard Model hypothesis of 0.9946 (which will be approximated by 1) and then using the error estimate for the blind sample ratio, one would expect a 90 % upper confidence limit of 1.0363 on the $\mathcal{R}_{\tau/\mu}$. Assuming there is no evidence of a signal and a 250 MeV/c^2 difference between the $\Upsilon(3S)$ and the CP-odd Higgs boson, an upper confidence

limit on $\tan\beta$ would be $\tan\beta \lesssim 8.82$ (at 90 % confidence).

Chapter 7

Conclusion

Using the `low` and `high` unblind data, the value of $\mathcal{R}_{\tau/\mu}$ is measured as $1.0385\pm0.034\pm0.014\pm$ 0.013, where the first error is the data statistical, the second error is the estimated systematic error of the analysis, and the final error is the CC-blind systematic (a conservative cross-check systematic based upon the τ-pair to μ-pair production cross section ratio at $\sqrt{s} = m_{\Upsilon(4S)}$). This measurement is three times more precise than the previous `CLEO` measures of this quantity and is consistent with the hypothesis of lepton universality. This estimate used only 2.4 fb^{-1} of data from the $\Upsilon(3S)$ running period. Assuming that the systematic errors will not scale with a larger data sample, the overall statistical error will drop to 0.011 and thus the total estimated error will be 2.2 %.

The ratio of τ-pair to μ-pair production cross sections is measured to be $0.811385 \pm$ 0.00062 ± 0.0078. In addition, individual branching fractions of the $\Upsilon(3S)$ to τ- and μ-pairs is measured to be $\mathcal{B}(\Upsilon(3S) \to \tau^+\tau^-) = 0.027362\pm0.00090\pm0.0018$ and $\mathcal{B}(\Upsilon(3S) \to \mu^+\mu^-) = 0.0263479 \pm 0.00023 \pm 0.0016$. Using the $\mathcal{B}(\Upsilon(3S) \to \mu^+\mu^-)$, the $\mathcal{B}(\Upsilon(3S) \to \gamma A^0)\mathcal{B}(A^0 \to \tau^+\tau^-) < 2.6 \times 10^{-3}$ at 90 % confidence (upper limit).

Bibliography

[1] J.P. Lees, V. Poireau, V. Tisserand, et al. Time-integrated luminosity recorded by the babar detector at the pep-ii collider. Nuclear Instruments and Methods in Physics Research Section A: Accelerators, Spectrometers, Detectors and Associated Equipment, 726(0):203 – 213, 2013.

[2] Swagato Banerjee. Search for a Light Higgs Boson at BaBar. ArXiv e-prints, 2009.

[3] Y. Kubota, J. K. Nelson, D. Perticone, et al. The CLEO II detector. Nuclear Instruments and Methods in Physics Research A, 320:66–113, August 1992.

[4] D. Besson and CLEO Collaboration. First Observation of upsilon(3s) $\rightarrow$ tau tau and tests of lepton universality in upsilon decays. Physical Review Letters, 98:052002, 2007.

[5] B. Aubert, A. Bazan, A. Boucham, et al. The babar detector. Nuclear Instruments and Methods in Physics Research Section A: Accelerators, Spectrometers, Detectors and Associated Equipment, 479(1):1 – 116, 2002. Detectors for Asymmetric B-factories.

[6] B. Aubert, R. Barate, D. Boutigny, et al. The babar detector: Upgrades, operation and performance. Nuclear Instruments and Methods in Physics Research Section A: Accelerators, Spectrometers, Detectors and Associated Equipment, 729(0):615 – 701, 2013.

[7] P. F. Harrison and H. R. Quinn, editors. The BaBar Physics Book: Physics at an asymmetric B factory. The BABAR Collaboration, 1998.

[8] R. Aaij, C. Abellan Beteta, A. Adametz, et al. Measurement of the $B^0 - \overline{B}^0$ oscillation frequency Δm_d with the decays $B^0 \to D^- \pi^+$ and $B^0 \to J/\psi K^{*0}$. Physics Letters B, 719(45):318 – 325, 2013.

[9] D. Griffiths. Introduction to Elementary Particles. John Wiley & Sons, New York, 1987.

[10] F. Halzen and A.D. Martin. Quarks and Leptons: An Introductory Course in Modern Particle Physics. John Wiley & Sons, New York, 1st edition, 1984.

[11] I.J.R. Aitchison and A.J.G. Hey. Gauge Theories in Particle Physics, Volume 1: From Relativistic Quantum Mechanics to QED. Taylor & Francis, New York, 3rd, revised edition, 2002.

[12] J. Beringer et al. Review of Particle Physics (RPP). Phys.Rev., D86:010001, 2012.

[13] Ta Pei Cheng and Ling Fong Li. Gauge theory of elementary particle physics. Oxford University Press, Toronto, 1st edition, 1984.

[14] C.P. Burgess and G.D. Moore. The standard model: A primer. Cambridge University Press, 2007.

[15] M. L. Perl et. al. Evidence for anomalous lepton production in $e^+ - e^-$ annihilation. Phys. Rev. Lett., 35(22):1489–1492, Dec 1975.

[16] P. Renton. Electroweak Interactions: An Introduction to the Physics of Quarks and Leptons. Cambridge University Press, 1990.

[17] A. Stahl. Physics with Tau Leptons. Springer, New York, 1st edition, 2000.

[18] Swagato Banerjee, Bolek Pietrzyk, J. Michael Roney, and Zbigniew Was. Tau and muon pair production cross sections in electron-positron annihilations at $\sqrt{s} = 10.58$ GeV.

Phys. Rev. D, 77:054012, Mar 2008.

[19] G. Aad, T. Abajyan, B. Abbott, et al. Observation of a new particle in the search for the standard model higgs boson with the {ATLAS} detector at the {LHC}. Physics Letters B, 716(1):1 – 29, 2012.

[20] S. Chatrchyan, V. Khachatryan, A. M. Sirunyan, et al. Observation of a new boson at a mass of 125 GeV with the CMS experiment at the LHC. Physics Letters B, 716:30–61, September 2012.

[21] Achim Stahl. Physics with Tau Leptons (Springer Tracts in Modern Physics). Springer, 2000.

[22] J. Swain and L. Taylor. Constraints on the τ neutrino mass and mixing from precise measurements of τ decay rates. Phys. Rev. D, 55:R1–R4, Jan 1997.

[23] Achim Stahl. The michel parameter in decays. Physics Letters B, 324(1):121 – 124, 1994.

[24] Yao, W.-M. et. al. Review of particle physics. Journal of Physics G, 33:1+, 2006.

[25] R. Hagedorn. Relativistic Kinematics. W. A. Benjamin, Inc., New York, 1st edition, 1963.

[26] E. Byckling and K. Kajantie. Particle Kinematics. John Wiley & Sons, Toronto, 1st edition, 1973.

[27] W. Greiner, S. Schramm, and E. Stein. Quantum Chromodynamics. Springer-Verlag, Berlin, 2nd edition, 2002.

[28] R. J. Barlow. Statistics: A Guide to the Use of Statistical Methods in the Physical Sciences (Manchester Physics Series). Wiley, 11 1993.

[29] Miguel Angel Sanchis-Lozano. Searching for new physics in leptonic decays of bottomonium. Mod.Phys.Lett., A17:2265–2276, 2002.

[30] Miguel Angel Sanchis-Lozano. Hints of new physics in bottomonium decays and spectroscopy. Nuclear Physics B - Proceedings Supplements, 142:163 – 166, 2005. Hyperons, Charm and Beauty Hadrons - Proceedings of the 6th International Conference Hyperons, Charm and Beauty Hadrons.

[31] B. Aubert, Y. Karyotakis, J. Lees, et al. Search for a low-mass higgs boson in $\upsilon(3s) \to \gamma A^0$, $A^0 \to \tau^+\tau^-$ at $BABAR$. Phys. Rev. Lett., 103:181801, Oct 2009.

[32] J. Lees, V. Poireau, V. Tisserand, et al. Search for a low-mass scalar higgs boson decaying to a tau pair in single-photon decays of $\upsilon(1s)$. Phys. Rev. D, 88:071102, Oct 2013.

[33] Esteban Fullana and Miguel-Angel Sanchis-Lozano. Hunting a light cp-odd non-standard higgs boson through its tauonic decay at a (super) B factory. Physics Letters B, 653:67, 2007.

[34] Esteban Fullana and Miguel-Angel Sanchis-Lozano. Hunting a light cp-odd non-standard higgs boson through its tauonic decay at a (super) b factory. Physics Letters B, 653(1):67 – 74, 2007.

[35] M. A. Sanchis-Lozano. Searching for new physics in leptonic decays of bottomonium. MOD.PHYS.LETT.A, 17:2265, 2002.

[36] J. Brodzicka, T. Browder, P. Chang, et al. Physics achievements from the Belle experiment. Progress of Theoretical and Experimental Physics, 2012(4):040000, December 2012.

[37] Stanford University. SLAC Virtual Visitor Center - Accelerator Form and Function.

http://www2.slac.stanford.edu/vvc/accelerator.html, 2006.

[38] K. Kleinknecht. Detectors for Particle Radiation. Cambridge University Press, New York, 2nd edition, 2003.

[39] Richard Clinton Fernow. Introduction to Experimental Particle Physics. Cambridge University Press, 1989.

[40] Dan Green. The Physics of Particle Detectors (Cambridge Monographs on Particle Physics, Nuclear Physics and Cosmology). Cambridge University Press, 2005.

[41] The BABAR Collaboration. The BABAR Detector: Upgrades, Operation and Performance. ArXiv e-prints, May 2013.

[42] The BABAR Collaboration. The BABAR Detector. Nuclear Instrument and Methods In Physics Research, A479:1, 2002.

[43] Joshua R Klein and Aaron Roodman. Blind analysis in nuclear and particle physics. Annual Review of Nuclear and Particle Science, 55(1):141–163, 2005.

[44] F. Wilson. Babar analysis: Think before you leap. BaBar Analysis School 2011 Lecture, 2011.

[45] S. Jadach, B. F. L. Ward, and Z. Wacs. Coherent exclusive exponentiation for precision monte carlo calculations. Phys. Rev. D, 63:113009, May 2001.

[46] Z. Was. {TAUOLA} the library for lepton decay, and kkmc/koralb/koralz/ status report. Nuclear Physics B - Proceedings Supplements, 98(13):96 – 102, 2001.

[47] Stanisaw Jadach, Johann H. Khn, and Zbigniew Was. {TAUOLA} - a library of monte carlo programs to simulate decays of polarized leptons. Computer Physics Communications, 64(2):275 – 299, 1991.

[48] S. Jadach, B.F.L. Ward, and Z. Was. The precision monte carlo event generator {KK} for two-fermion final states in e+e collisions. Computer Physics Communications, 130(3):260 – 325, 2000.

[49] Torbjrn Sjstrand and Mats Bengtsson. The lund monte carlo for jet fragmentation and e+ e- physics - jetset version 6.3 - an update. Computer Physics Communications, 43(3):367 – 379, 1987.

[50] David J. Lange. The evtgen particle decay simulation package. Nuclear Instruments and Methods in Physics Research Section A: Accelerators, Spectrometers, Detectors and Associated Equipment, 462(12):152 – 155, 2001. BEAUTY2000, Proceedings of the 7th Int. Conf. on B-Physics at Hadron Machines.

[51] A. Ryd, D. Lange, N. Kuznetsova, et al. Evtgen: A monte carlo generator for b-physics.

[52] Elisabetta Barberio, Bob van Eijk, and Zbigniew Was. Photos a universal monte carlo for {QED} radiative corrections in decays. Computer Physics Communications, 66(1):115 – 128, 1991.

[53] S. Agostinelli, J. Allison, K. Amako, et al. Geant4a simulation toolkit. Nuclear Instruments and Methods in Physics Research Section A: Accelerators, Spectrometers, Detectors and Associated Equipment, 506(3):250 – 303, 2003.

[54] Edward Farhi. Quantum chromodynamics test for jets. Phys. Rev. Lett., 39:1587–1588, Dec 1977.

[55] Byron P. Roe. Probability and Statistics in Experimental Physics (Undergraduate Texts in Contemporary Physics). Springer, 2nd edition, 7 2001.

[56] O. Behnke, K. Kröninger, G. Schott, and T. Schörner-Sadenius. Data Analysis in High Energy Physics: A Practical Guide to Statistical Methods. Wiley, 2013.

[57] I. Nugent et. al. Measurements of $B(\tau^- \to K^-\nu)/B(\tau^- \to e^-\nu\nu)$, $B(\tau^- \to \pi^-\nu)/B(\tau^- \to e^-\nu\nu)$, $B(\tau^- \to \mu^-\nu\nu)/B(\tau^- \to e^-\nu\nu)$. BAD #1905, Version 22 (*BABAR* internal analysis document), 2009.

[58] Y. Amhis et al. Averages of B-Hadron, C-Hadron, and tau-lepton properties as of early 2012. arXiv/hep-ex, 2012.

[59] G. Raymond and T. Christos. Luminosity measurement for the runs 1,2 and 3 data sample using release 12 and sp5 simulation. BAD #1312, Version 1 (*BABAR* internal analysis document), 2005.

[60] G. Raymond. Luminosity measurement for the run 4 and run 5 data samples using release 18d and sp8 simulation. BAD #1850, Version 1 (*BABAR* internal analysis document), 2007.

[61] C. Hearty and G. McGregor. Summary of upsilon(2s) counting. BAD #2126, Version 1 (*BABAR* internal analysis document), 2008.

[62] C. Hearty and G. McGregor. Hadronic and gamma-pair event selection for upsilon(3s) counting. BAD #2069, Version 6 (*BABAR* internal analysis document), 2008.

[63] T. Christos and P. Wang. Luminosity measurement for the run 1 data. BAD #229, Version 1 (*BABAR* internal analysis document), 2001.

[64] C.M. Carloni Calame, G. Montagna, O. Nicrosini, and F. Piccinini. The {BABAYAGA} event generator. Nuclear Physics B - Proceedings Supplements, 131(0):48 – 55, 2004. SIGHADO3 Proceedings of the Workshop on Hadronic Cross Section at Low Energy.

[65] A. Hafner. Test and implementation of babayaga@nlo into the *BABAR* simulation environment. BaBar Analysis Presentation, 2007.

[66] Giovanni Balossini, Carlo M. Carloni Calame, Guido Montagna, Oreste Nicrosini, and Fulvio Piccinini. Matching perturbative and parton shower corrections to bhabha process at flavour factories. Nuclear Physics B, 758(12):227 – 253, 2006.

[67] H. Choi. personal correspondence.

[68] G. Adams, M. Chasse, M. Cravey, et al. Measurement of the muonic branching fractions of the narrow upsilon resonances. Phys. Rev. Lett., 94:012001, Jan 2005.

[69] B. Thorsten. Likelihood-based electron identification. BAD #396, Version 1 (BABAR internal analysis document), 2002.

[70] Homer A. Neal Jr. Data preservation and long term accessibility in high energy physics at the 2nd international conference on frontiers in diagnostic technologies in frascati, italy. Nuclear Instruments and Methods in Physics Research Section A: Accelerators, Spectrometers, Detectors and Associated Equipment, 720(0):62 – 66, 2013. Selected papers from the 2nd International Conference Frontiers in Diagnostic Technologies (ICFDT2).

Appendix A

Electron Selector

A.1 Electron Likelihood Tight Selector

Three sub-detectors, the electromagnetic calorimeter (EMC), the drift chamber (DCH), and the Cherenkov detector (DIRC) in the BABAR experiment are used to separate electrons from muons and charged hadrons. These detectors are described in [5, 6].

Using high purity data samples of electrons, muons, pions, kaons, and protons (selection is documented in [69]) the discriminating variables involved in electron identification are discussed.

This is done in the following steps: first a set of loose pre-selection cuts is developed, second, probability density functions are constructed for each discriminating variable. Under the assumption of independent measurements from the individual sub-detectors these are combined to compute the likelihood $\mathcal{L}(\phi)$ for each particle hypothesis.

Weighting the individual likelihoods with *a priori* probability, the likelihood fraction is computed as follows:

$$f_\mathcal{L} = \frac{p_e \mathcal{L}_e}{p_e \mathcal{L}_e + p_\pi \mathcal{L}_\pi + p_K \mathcal{L}_K + p_p \mathcal{L}_p}. \tag{A.1}$$

A track is selected as an electron if it passes the pre-selection cuts and a given cut on the likelihood fraction. Electron identification efficiency and hadronic *fake* rates are measured on control data samples.

Electrons entering the electromagnetic calorimeter will produce an electromagnetic shower.

Since the CsI crystals cover at least 16.1 radiation lengths ($\mathbf{X}_0$) the entire kinetic energy of an electron or photon is be deposited within the calorimeter. Electron candidates are identified by the ratio of 'bump' energy in the electromagnetic calorimeter to track momentum, E_{EMC}/p. In a perfect calorimeter this would be centred around 1.

In the *BABAR* experimental set-up, the distribution is centred slightly lower at 0.95 and shows a non-Gaussian tail at lower values of $E_{EMC}/|p|$ due to,

(1) material in front of the calorimeter and between the individual crystals;

(2) leakage through the sides caused by staggered crystal arrangement; and

(3) reconstruction inefficiencies.

In addition, the track must have a measured mean ($\mathrm{d}E/\mathrm{d}x$) in the DCH consistent with the electron hypothesis. The lateral[1] and azimuthal shape of the EMC shower and the observed Cherenkov angle in the DIRC must also be consistent with an electron. The azimuthal 'shape' is measured using the difference between the polar angles where the track intersects the electromagnetic calorimeter and the shower centre. Due to the curvature of the track in the $x - y$ plane, this angle carries information about longitudinal energy distribution. Electromagnetic showers reach their maximum earlier in the crystal than hadronic showers and their centre is closer to the impact point of the track on the electromagnetic calorimeter.[2]

A detailed review of the electron particle identification using a likelihood formulation is provided by BAD 396 [69].

---

[1]The lateral moment of the cluster associated with this track, is given by the ratio of (1) to (2):

(1) Sum of energies of all but the 2 most energetic crystals, weighted by the square of distance to the cluster centre.

(2) Sum of (1) and the energies of the 2 most energetic crystals, which are weighted by $(5 \text{ cm})^2$ (5 cm is approximately the average distance between two crystals).

The lateral moment is a measure of the 'radial' (the crystals are not circular, however if the electromagnetic shower can spread to surrounding crystals) energy profile of the cluster, and is used to suppress clusters from electronic noise (low lateral moment) or hadronic interactions (high lateral moment).

[2]Other selectors use $|A_{4,2}|$, is absolute value of $(4, 2)-$Zernike Moment of the associated EMC cluster. The $(4, 2)$-Zernike Moment measures the azimuthal asymmetry of the cluster about its peak, can be used to distinguish between electromagnetic from hadronic showers.

Appendix B

TAUOLA and EvtGen Details

B.1   TAUOLA Branching Fraction

The *BABAR* version of TAUOLA is located on the LTDA in the direction `/BFROOT/dist/packages/tauola/V00-01`
The code is stored with a CVS repository and shows a last change date of 2004. The values
are reported here are probably from the PDG from the early 2000.

Branching Fraction	Channel	Routine Type	TAUOLA Decay Code
0.17865206	$e^-\overline{\nu}_e\nu_\tau$	DADMEL	1
0.17355202	$\mu^-\overline{\nu}_e\nu_\tau$	DADMMU	2
0.11084165	$\pi^-\nu_\tau$	DADMPI	3
0.25375548	$\pi^-\pi^0\nu_\tau$	DADMRO	4
0.09178355	$\pi^-\pi^+\pi^-\nu_\tau$	DADMAA	5
0.00694604	$K^-\nu_\tau$	DADMKK	6
0.01364108	K^{*-}	DADMKS	7
0.04365426	$\pi^-\pi^+\pi^-\pi^0\nu_\tau$	DPH4PI	8
0.01261907	$\pi^-\pi^0\pi^0\pi^0\nu_\tau$	DPH4PI	9
0.005011030	$\pi^-\pi^+\pi^-\pi^0\pi^0\nu_\tau$	DPH5PI	50
0.000789005	$\pi^-\pi^+\pi^-\pi^+\pi^-\nu_\tau$	DPHNPI	71
0.000183001	$\pi^-\pi^+\pi^-\pi^+\pi^-\pi^0\nu_\tau$	DPHNPI	72
0.000251001	$\pi^-\pi^+\pi^-\pi^0\pi^0\pi^0\nu_\tau$	DPHNPI	73
0.00159001	$K^-\pi^-K^+\nu_\tau$	DPHSPK	84
0.00167201	$K^0\pi^-\overline{K}^0\nu_\tau$	DPHSPK	85
0.00153601	$K^-\pi^0K^0\nu_\tau$	DPHSPK	86
0.00068000	$K^-\pi^0\pi^0\nu_\tau$	DPHSPK	87
0.00300902	$\pi^-\pi^+K^-\nu_\tau$	DPHSPK	88
0.00376702	$\pi^-\overline{K}^0\pi^0\nu_\tau$	DPHSPK	89
0.00183001	$\eta\pi^-\pi^0\nu_\tau$	DPHSPK	90
0.00080200	$\pi^-\pi^0\gamma\nu_\tau$	DPHSPK	91
0.09178355	$\pi^-\pi^0\pi^0\nu_\tau$	DPHSPK	92
0.00165101	$K^-K^0\nu_\tau$	DPHSPK	103

Table B.1: TAUOLA τ^- Decay Table.

B.2 EvtGen Branching Fraction

In addition to KK2F (which uses TAUOLA) to decay τ, BABAR use another MC generator to handle $\Upsilon(\mathbf{n}S)$ decays (and also the sub-decays of τ leptons). The generator used for decays of $\Upsilon(3S)$, $\Upsilon(2S)$ and $\Upsilon(1S)$ is EvtGen. Within the context of this analysis, the code is located on the LTDA at /BFROOT/dist/packages/EvtGen/V00-17-01/DECAY.DEC.

EvtGen generates decays of any particle through a series of decay tables. If the initial event that is produced is an $\Upsilon(3S)$ (which is given specific properties from a simulated e^+ e^- interaction), it will decay into one of the defined daughter particles as defined within the Table B.3 (see B.2.2). Each table entry defines an estimated branching fraction for the

associated mode as well as an simulation engine used to decay into the next state daughter particles. Subsequent, daughter particles are then decayed in turn (until particles with no defined decay channels are reached)[1].

B.2.1 EvtGen τ Decay Table

Branching Fraction	Channel	PHOTOS	Simulation Type
0.1778	$e^-\overline{\nu}_e\nu_\tau$	Yes	TAULNUNU
0.1731	$\mu^-\overline{\nu}_\mu\nu_\tau$	Yes	TAULNUNU
0.1095	$\pi^-\nu_\tau$	No(*)	TAUSCALARNU
0.2531	$\pi^-\pi^0\nu_\tau$	No(*)	TAUHADNU^a
0.09234	$\pi^-\pi^-\pi^+\nu_\tau$	No(*)	TAUHADNU^b
0.0910	$\pi^0\pi^0\pi^-\nu_\tau$	No(*)	TAUHADNU^c
0.00686	$K^-\nu_\tau$	No(*)	TAUSCALARNU
0.0134	$K^{*-}\nu_\tau$	No(*)	TAUVECTORNU
0.0450	$\pi^-\pi^+\pi^-\pi^0\nu_\tau$	No(*)	JETSET^d
0.0100	$\pi^-\pi^0\pi^0\pi^0\nu_\tau$	No(*)	JETSET^e
0.0015	$K^-\pi^-K^+\nu_\tau$	No(*)	JETSET^f
0.0015	$K^0\pi^-\overline{K}^0\nu_\tau$	No(*)	JETSET^g
0.0015	$K^-\pi^0K^0\nu_\tau$	No(*)	JETSET^h
0.0005	$K^-\pi^0\pi^0\nu_\tau$	No(*)	JETSET^i
0.0050	$K^-\pi^+\pi^-\nu_\tau$	No(*)	JETSET^j
0.0055	$\pi^-\overline{K}^0\pi^0\nu_\tau$	No(*)	JETSET^k
0.0017	$\eta\pi^-\pi^0\nu_\tau$	No(*)	JETSET^l
0.0013	$\pi^-\pi^0\gamma\nu_\tau$	No(*)	JETSET^m

Table B.2: EvtGen τ^- Decay Table.

^{a}Associated parameters: -0.108 0.775 0.149 1.364 0.400.
^{b}Associated parameters: -0.108 0.775 0.149 1.364 0.400.
^{c}Associated parameters: -0.108 0.775 0.149 1.364 0.400.
^{d}Associated parameter: 41.
^{e}Associated parameter: 41.
^{f}Associated parameter: 41.
^{g}Associated parameter: 41.
^{h}Associated parameter: 41.
^{i}Associated parameter: 41.
^{j}Associated parameter: 41.
^{k}Associated parameter: 41.
^{l}Associated parameter: 41.
^{m}Associated parameter: 41.

[1]An example decay chain is, starting with, $\Upsilon(3S) \to \tau^+\tau^-$; after that, each of the τ's are decayed, one case that would occur is, $\tau^- \to \pi^-\nu_\tau$ and $\tau^+ \to \mu^+\overline{\nu}_\tau\nu_\mu$ and the decay chain ends here because π^-, μ^-, ν_τ, ν_μ, $\overline{\nu}_\tau$ are considered to be detector level particles.

B.2.2 EvtGen $\Upsilon(3S)$ Decay Table

Branching Fraction	Channel	PHOTOS	Simulation Type
0.022	e^+e^-	Yes	VLL
0.022	$\mu^+\mu^-$	Yes	VLL
0.022	$\tau^+\tau^-$	Yes	VLL
0.0442	$\Upsilon(1S)\pi^+\pi^-$	No(*)	YMSTOYNSPIPICLEO[a]
0.0226	$\Upsilon(1S)\pi^0\pi^0$	No(*)	YMSTOYNSPIPICLEO[b]
0.0290	$\Upsilon(2S)\pi^+\pi^-$	No(*)	YMSTOYNSPIPICLEO[c]
0.0200	$\Upsilon(2S)\pi^0\pi^0$	No(*)	YMSTOYNSPIPICLEO[d]
0.00067	$\Upsilon(1S)\eta$	No(*)	PARTWAVE[e]
0.001	$h_b\pi^0$	No(*)	PHSP
0.001	$h_b\pi^+\pi^-$	No(*)	PHSP
0.0006	$h_b\pi^0\pi^0$	No(*)	PHSP
0.000005	$\eta_b\gamma$	No(*)	PHSP
0.000040	$\eta_b(2S)\gamma$	No(*)	PHSP
0.000050	$\eta_b(3S)\gamma$	No(*)	PHSP
0.0590	$\gamma\chi_{b_0}(2P)$	No(*)	HELAMP[f]
0.1260	$\gamma\chi_{b_1}(2P)$	No(*)	HELAMP[g]
0.1310	$\gamma\chi_{b_2}(2P)$	No(*)	HELAMP[h]
0.0030	$\gamma\chi_{b_0}$	No(*)	HELAMP[i]
0.0073	$\gamma\chi_{b_1}$	No(*)	HELAMP[j]
0.0108	$\gamma\chi_{b_2}$	No(*)	HELAMP[k]
0.00700	$d\bar{d}$	No(*)	JETSET[l]
0.02800	$u\bar{u}$	No(*)	JETSET[m]
0.00700	$s\bar{s}$	No(*)	JETSET[n]
0.02800	$c\bar{c}$	No(*)	JETSET[o]
0.39274	$\gamma\gamma\gamma$	No(*)	JETSET[p]
0.01500	$\gamma\gamma\gamma$	No(*)	JETSET[q]

Table B.3: EvtGen $\Upsilon(3S)$ Decay Table.

[a]Additional Parameters: -2.523 1.189

[b]Additional Parameters: -2.523 1.189

[c]Additional Parameters: -0.395 0.001

[d]Additional Parameters: -0.395 0.001

[e]Additional Parameters: 0.0 0.0 1.0 0.0 0.0 0.0

[f]Additional Parameters: 1. 0. 1. 0.;

[g]Additional Parameters: 1. 0. 1. 0. -1. 0. -1. 0.;

[h]Additional Parameters: 2.4494897 0. 1.7320508 0. 1. 0. 1. 0. 1.7320508 0. 2.4494897 0.;

[i]Additional Parameters: 1. 0. 1. 0.;

[j]Additional Parameters: 1. 0. 1. 0. -1. 0. -1. 0.;

[k]Additional Parameters: 2.4494897 0. 1.7320508 0. 1. 0. 1. 0. 1.7320508 0. 2.4494897 0.;

[l]Additional Parameters: 32;

[m]Additional Parameters: 32;

[n]Additional Parameters: 32;

[o]Additional Parameters: 32;

[p]Additional Parameters: 4;

[q]Additional Parameters: 4;

B.2.3 $\Upsilon(1S)$ and $\Upsilon(2S)$ Decay Tables

Branching Fraction	Channel	PHOTOS	Simulation Type
0.0194	e^+e^-	Yes	VLL
0.0194	$\mu^+\mu^-$	Yes	VLL
0.0194	$\tau^+\tau^-$	No(*)	VLL
0.1870	$\Upsilon(1S)\pi^+\pi^-$	No(*)	YMSTOYNSPIPICLEO[a]
0.0935	$\Upsilon(1S)\pi^0\pi^0$	No(*)	YMSTOYNSPIPICLEO[b]
0.0008	$\Upsilon(1S)\eta$	No(*)	PARTWAVE[c]
0.000005	$\eta_b\gamma$	No(*)	PHSP
0.000063	$\eta_b(2S)\gamma$	No(*)	PHSP
0.0380	$\gamma\chi_{b_0}$	No(*)	HELAMP[d]
0.0690	$\gamma\chi_{b_1}$	No(*)	HELAMP[e]
0.0660	$\gamma\chi_{b_2}$	No(*)	HELAMP[f]
0.00700	$d\bar{d}$	No(*)	JETSET[g]
0.02800	$u\bar{u}$	No(*)	JETSET[h]
0.00700	$s\bar{s}$	No(*)	JETSET[i]
0.02800	$c\bar{c}$	No(*)	JETSET[j]
0.39274	$\gamma\gamma\gamma$	No(*)	JETSET[k]
0.01500	$\gamma\gamma\gamma$	No(*)	JETSET[l]

Table B.4: EvtGen $\Upsilon(2S)$ Decay Table.

[a]Additional Parameters: -0.753 0.000;

[b]Additional Parameters: -0.753 0.000;

[c]Additional Parameters: 0.0 0.0 1.0 0.0 0.0 0.0;

[d]Additional Parameters: 1. 0. +1. 0.;

[e]Additional Parameters: 1. 0. 1. 0. -1. 0. -1. 0.;

[f]Additional Parameters: 2.4494897 0. 1.7320508 0. 1. 0. 1. 0. 1.7320508 0. 2.4494897 0.;

[g]Additional Parameters: 32;

[h]Additional Parameters: 32;

[i]Additional Parameters: 32;

[j]Additional Parameters: 32;

[k]Additional Parameters: 4;

[l]Additional Parameters: 4;

Branching Fraction	Channel	PHOTOS	Simulation Type
0.0249	e^+e^-	Yes	VLL
0.0249	$\mu^+\mu^-$	Yes	VLL
0.0249	$\tau^+\tau^-$	No(*)	VLL
0.00036	$\eta_b\gamma$	No(*)	PHSP
0.01500	$d\bar{d}$	No(*)	JETSET^a
0.04500	$u\bar{u}$	No(*)	JETSET^b
0.01500	$s\bar{s}$	No(*)	JETSET^c
0.04500	$c\bar{c}$	No(*)	JETSET^d
0.77594	$\gamma\gamma\gamma$	No(*)	JETSET^e
0.02900	$\gamma\gamma\gamma$	No(*)	JETSET^f

Table B.5: EvtGen $\Upsilon(1S)$ Decay Table.

^{a}Additional Parameters: 32;
^{b}Additional Parameters: 32;
^{c}Additional Parameters: 32;
^{d}Additional Parameters: 32;
^{e}Additional Parameters: 4;
^{f}Additional Parameters: 4;

Appendix C

Numerical Simulation Using KK2F

C.1 Numerical Simulation of $\tau\tau$ cross section

Using `GeneratorQA` as the interface to the KK2F event generator. There is an additional step needed prior to running the generator, `TAUOLA` source code needs to have a simple patch (default configuration for τ pair generation causes a crash). This configuration runs within a Scientific Linux 5 (SL5) virtual machine on the long term data access cluster (LTDA) [70]. These commands on the head node (bbrltda01, bbrltda02, bbrltda03):

Listing C.1: Setting up GeneratorsQA in a new release

cd /awg/tauqed/gking
newrel −t current **test**
cd test
srtpath **<return> <return>**
addpkg GeneratorsQA
addpkg PepCond
addpkg tauola
addpkg workdir

This can be checked with showtag.


```
[gking@bbr-ltda-vm1754 test]$ showtag
GeneratorsQA V00-03-29
PepCond V01-02-02
tauola V00-01-25
workdir V00-04-21
```

Small patch for tauola/formf.F (Fortran code), issue is due to calling FORMAT function with a 'tab' or '\t' character.

```
[gking@bbrltda01 tauola]$ cvs diff
cvs diff: Diffing .
Index: formf.F
===================================================================
RCS file: /afs/slac.stanford.edu/g/babar/repo/tauola/formf.F,v
retrieving revision 1.12
diff -r1.12 formf.F
819c819
<      . /,   '   R. DECKER, M. FINKEMEIER, P. HEILIGER AND H.H. JONSSON',\t
---
>      . /,   '   R. DECKER, M. FINKEMEIER, P. HEILIGER AND H.H. JONSSON',
```

Log into a SL5 virtual machine (interactive node, with virtual machine operating system configured to SL5). The packages have to be compiled and linked (this is done through the command `gmake installdirs` and `gmake all`)[1]. The command `cond24boot11` configures access to the conditions database.

Listing C.2: Compiling Commands

```
ssh sl5
cd /awg/tauqed/gking/test
srtpath <return> <return>
gmake installdirs
gmake workdir.setup
gmake all
cond24boot11
```

Shifting to the workdir (the directory used to run the executables).

Listing C.3: Setting up workdir

```
cd workdir
cp ../GeneratorsQA/Kk2f.tcl .
ln -s ../PepCond/pepEnergiesUpsilon3S.raw
ln -s ../PepCond/pepEnergiesUpsilon3SOff.raw
ln -s ../PepCond/pepEnergies.raw
ln -s ../PepCond/pepEnergiesCorr.raw
ln -s ../PepCond/pepBoostCalUpsilon3S.raw
ln -s ../PepCond/pepBoostCal.raw
ln -s ../PepCond/pepBeamSpotCal.raw
```

The symbolic links (generated by the command `ln -s`) to files in the PepCond directory allow one to quickly change the configuration of the beam parameters and allow for the program running in `workdir` to access them directly. This allows for modification of the centre-of-mass energy (and boost).

Listing C.4: GeneratorsQA/Kk2f.tcl

---

[1]`gmake installdirs` creates the output location for the libraries and binaries. `gmake all` compiles and links all checked out packages

```
# FILE: Kk2f.tcl
# PURPOSE: run GeneratorsQA using the Kk2f generator
# $Id: Kk2f.tcl,v 1.3 2004/11/02 21:11:02 abi Exp $
#

#—————————————————————————————————————————#

# common stuff:

sourceFoundFile GeneratorsQA/common.tcl

#—————————————————————————————————————————#

# GfiKk2f specifics:

disableGenerators 0
module enable GfiKk2f

module talk GfiKk2f
  generate set "tau+ tau−"
  scaleEnergy set true
  transformEvent set true
exit

# A module to test KK2f:
path append genQA GqaTauHisto

   GeneratorsQA/common.tcl
```

Listing C.5: GeneratorsQA/common.tcl

```
# FILE: initial.tcl
# PURPOSE: This script creates the genQA path and does stuff needed to run all
# generators
# $Id: common.tcl,v 1.14 2010/12/22 22:32:28 abi Exp $
#

#turn on actions
action enable all

path create genQA

#—————————————————————————————————————————#
## the input module:

module input RacTestInput

#—————————————————————————————————————————#
```

control of random numbers:

path **append** genQA RandomControl

#——#
 # The generators and all they need:

sourceFoundFile GenFwkInt/GfiSequence.tcl
path **append** genQA GfiSequence

#——#
 # QA modules:
#——#

 # a module to test GenFwkInt:

#path append genQA GqaGfiTest
#module talk GqaGfiTest
 #   testCollisionGenerator set true
#exit

#——#

 # Load generated data onto the event (needed for GfiMCAnalysis):

path **append** genQA BtaLoadMcCandidates

mod talk BtaLoadMcCandidates
  requireGTrackList **set** false
exit

#——#

 # Histogram quantities from the event:
path **append** genQA GqaMCAnalysis
#——#

 # module to test GfiFlightLenScaler. Didsable bhy default
path **append** genQA GfiTestFlightLenScaler
module disable GfiTestFlightLenScaler
#——#

 # Event store stuff:

catch {
  if {$env(GQA_DATABASE) == "yes"} {

```
    sourceFoundFile  BdbSequences/BdbSequence.tcl
    sourceFoundFile  BdbSequences/BdbOutputSequence.tcl
    sourceFoundFile  BdbSequences/BdbWriteSim.tcl
    sourceFoundFile  BdbSequences/BdbWriteRaw.tcl

    path append genQA BdbSequence

    module talk BdbEventOutput
      output set GeneratorsQA
    exit
  }
}
```

```
#———————————————————————————————————————————————————#
# set the name of the histogram file:

module talk HbkTupleEnv
  histFileName set "GfiMCTruth.hbook"
exit
```

```
#———————————————————————————————————————————————————#
# By default, disable dump to a file:

mod disable StdHepAsciiDump
```

To set-up the custom configuration of beam parameters, the following is done:

Listing C.6: Change Beam Parameter Example and Run

```
mod talk PepBuildEnv
pepEnergiesFile set pepEnergiesUpsilon3S.raw
pepBoostCalFile set pepBoostCalUpsilon3S.raw
pepBeamSpotCalFile set pepBeamSpotCal.raw
exit

mod talk RandomControl
maxEventsPerRun set 4100000
exit

mod disable HbkTupleEnv
module talk RooTupleEnv
histFileName set "GfiMCTruth−Y3SON.root"
exit

ev beg −nev 1000000
```

Custom particle generation and kinematic filtering can be enabled (for example, but not used in this case):

Listing C.7: GefSelectFilter Filtering Example

```
module enable GefSelectFilter
mod talk GefSelectFilter
echo "Setting up a Filter  ..."

BooNew acceptance = GefKinematic
BooObjects acceptance lump tracks = e+ e- mu+ mu- pi+ pi- K+ K-
BooObjects acceptance define angle = tracks -100 100 -100 100 0.383972435 2.70526034
afterFilter      set   acceptance
exit
```

It is also possible to change simulation parameters of the `KK2F` MC generator. *BABAR* `GeneratorQA` enables modification of the `TAUOLA` running parameters through the `TCL` module control environment:

Listing C.8: GfiKk2f xpar set example

```
module talk GfiKk2f
xpar set "901 : 4"
exit
```

`TAUOLA` and the *BABAR* `GeneratorQA` framework outputs a large amount of details of the

simulation process. There are a number of point of interest, including:

1. center-of-mass energy ($\sqrt{s}$);

2. estimated cross section of the process being simulated;[2]

3. estimate partial width of τ sub-decays (partial widths are measured in units of $G_F^2 m_e^5/(192\pi^3)$);

4. decay chain of few simulated decays;

5. estimated photon multiplicity.

The estimate value of the cross section for the $\Upsilon(4S)$ for both the τ pair cross section and

dimuon cross section is dicussed in detail, by Swagato et. al [18].

---

[2]The inclusion of the Higgs, and is estimated to be 100 GeV/c^2. The top mass is set to 175 GeV/c^2. These two parameters should have a small (to negligible) affect on the cross section estimate.

Events	Estimated Cross Section (nb)
1,000	0.9138 ± 0.0066
100,000	0.91892 ± 0.00065
1,000,000	0.91889 ± 0.00021

Table C.1: Cross section Estimate depends on the number of events used in simulation by `KK2F`.

Changing the number generated by a factor of 100 reduces the error by exactly 1/10. The simulation has an improved sampling of generating distribution and therefore the error on the mean should go down by roughly $1/\sqrt{N_{\text{gen}}}$. To get the estimate error as determined in the paper one would have to generate roughly $100,000 \times (0.67/0.21)^2 \approx 1,000,000$. If you want the statistical error to be 100 times smaller than the estimated systematic of 0.3 %, one would need to simulate, $100,000 \times (0.67/0.003)^2 \approx 4.99 \times 10^9$ (or 5 billion events)[3]. The ability to simulate five billion events is fairly challenging due to the limitations of the pseudo-random number generators, the computational precision necessary to accurately measure the mean and standard deviation, and the distinct possibility of bias sampling of the set of associated floating point numbers.

C.1.1 $\Upsilon(3S)$ Response

The relevant information for the $\Upsilon(3S)$ cross section as reported by `KK2F` is clipped from the output after finalizing simulation job.

```
**************************************************************************
*                  KK2f_Finalize   printouts                          *
*     10.35517560                cms energy total       cmsene    a0 *
*         100002                 total no of events     nevgen    a1 *
*           ** principal info on x-section **                         *
*     1.18033236  +- 0.00083267  xs_tot MC R-units      xsmc      a1 *
*   956.05300171                 xs_tot    picob.       xSecPb    a3 *
*     0.67444791                 error     picob.       xErrPb    a4 *
*     0.00070545                 relative error         erel      a5 *
*     0.81514237                 WTsup, largest WT       WTsup    a10 *
*                    ** some auxiliary info **                        *
```

---

[3]Similarly if you wanted the error to just be a factor of ten times smaller one would have to simulate 5×10^7, roughly 50 million events

```
*     809.91580016                    xs_born   picobarns      xborn    a11 *
*       1.12484750                    Raw phot. multipl.                === *
*       8.00000000                    Highest phot. mult.               === *
*                           End of KK2f  Finalize                           *
****************************************************************************
```

C.1.2 $\Upsilon(4S)$ Response

```
****************************************************************************
*                      KK2f_Finalize  printouts                          *
*     10.57821022                    cms energy total       cmsene    a0 *
*         100001                     total no of events     nevgen    a1 *
*            ** principal info on x-section **                           *
*      1.18388529  +- 0.00083966  xs_tot MC R-units         xsmc      a1 *
*    918.92025986                    xs_tot    picob.        xSecPb    a3 *
*      0.65173553                    error     picob.        xErrPb    a4 *
*      0.00070924                    relative error         erel      a5 *
*      0.81641169                    WTsup, largest WT       WTsup    a10 *
*                      ** some auxiliary info **                         *
*    776.12059436                    xs_born   picobarns     xborn    a11 *
*      1.13299867                    Raw phot. multipl.               === *
*      8.00000000                    Highest phot. mult.              === *
*                          End of KK2f  Finalize                         *
****************************************************************************
```

C.1.3 $\Upsilon(4S)$ Response with 350000 events

The estimated error drops by roughly 1/2; mean oscillates to 0.91805 ± 0.00035 nb

```
****************************************************************************
*                      KK2f_Finalize  printouts                          *
*     10.57821022                    cms energy total       cmsene    a0 *
*         350003                     total no of events     nevgen    a1 *
*            ** principal info on x-section **                           *
*      1.18276717  +- 0.00044785  xs_tot MC R-units         xsmc      a1 *
*    918.05238597                    xs_tot    picob.        xSecPb    a3 *
*      0.34761527                    error     picob.        xErrPb    a4 *
*      0.00037864                    relative error         erel      a5 *
*      1.06661924                    WTsup, largest WT       WTsup    a10 *
*                      ** some auxiliary info **                         *
*    776.12059436                    xs_born   picobarns     xborn    a11 *
*      1.13122745                    Raw phot. multipl.               === *
*      9.00000000                    Highest phot. mult.              === *
*                          End of KK2f  Finalize                         *
```

```
    **************************************************************************
```

C.1.4 $\Upsilon(4S)$ Response with 1000000 event

The estimated error is estimated to be 0.91889 ± 0.00021 nb.

```
    **************************************************************************
    *                       KK2f_Finalize   printouts                       *
    *       10.57821022               cms energy total      cmsene    a0 *
    *           1000026               total no of events     nevgen    a1 *
    *            ** principal info on x-section **                          *
    *        1.18385088  +- 0.00026535  xs_tot MC R-units    xsmc      a1 *
    *      918.89355647               xs_tot    picob.       xSecPb    a3 *
    *        0.20596484               error     picob.       xErrPb    a4 *
    *        0.00022414               relative error         erel      a5 *
    *        1.38870398               WTsup, largest WT       WTsup    a10 *
    *                  ** some auxiliary info **                            *
    *      776.12059436               xs_born   picobarns     xborn    a11 *
    *        1.13572747               Raw phot. multipl.               === *
    *        9.00000000               Highest phot. mult.              === *
    *                  End of KK2f  Finalize                                *
    **************************************************************************
```

C.2 τ-pair cross section summary

The following are the estimated τ-pair cross-section[4]:

Center of Mass Energy	Estimated Cross Section	Number of Simulated Events (Millions)
$\Upsilon(4S)$ on-peak	0.9189 ± 0.0021 nb	1.00
$\Upsilon(4S)$ off-peak	0.9226 ± 0.0021 nb	1.00
$\Upsilon(3S)$ on-peak	0.9556 ± 0.0021 nb	1.00
$\Upsilon(3S)$ off-peak	0.9604 ± 0.0025 nb	0.75
$\Upsilon(2S)$ on-peak	1.0148 ± 0.0022 nb	1.00
$\Upsilon(2S)$ off-peak	1.0203 ± 0.0022 nb	1.00

Table C.2: Cross section as calculated by KK2F at various centre-of-mass energies.

---

[4]750K events were used in the $\Upsilon(3S)$ off-peak simulation due to a problem with KK2F failing to complete the simulation for one million events.

C.3 Bhabha Simulation (generic)

Listing C.9: ProdDecayFiles/Bhabha_generic_lumi_C.tcl

```
#
# This tcl configures the Bhwide to generate a natural
# mixture of nonradiatve and radiative bhabhas.
# Both e+ and e- are limited in the 15--165deg angular
# region in the CMS.
# This corresponds to 17.93224 to 131.06434 deg in the LAB
# The cross section is 25.52 picobarn by ALIBABA
# File to be used for Luminosity measurement
#
# modified by Christos Touramanis on January 17 2001
# email : christos@slac.stanford.edu

disableGenerators 0
module enable GfiBhwide

module talk GfiBhwide
  minThetaPositron set 17.93224
  maxThetaPositron set 131.06434
  minThetaElectron set 17.93224
  maxThetaElectron set 131.06434
  minEnergyPositron set 0.1
  minEnergyElectron set 0.1
  maxCMSAcollinearity set 180.0
  minThetaPhoton set 0.0
  maxThetaPhoton set 180.0
  minEnergyPhoton set 0.0
  minNumEnergeticPhotons set 0
  maxNumPhotonsProduced set 10
  minPhotonTrackSeparation set 0.0
exit
```